

**Measurement of the Top Quark Mass by Dynamical
Likelihood Method using the Lepton + Jets Events
with the Collider Detector at Fermilab**

Taichi KUBO

February 2008

Measurement of the Top Quark Mass by Dynamical
Likelihood Method using the Lepton + Jets Events
with the Collider Detector at Fermilab

Taichi KUBO
(Doctoral Program in Physics)

Submitted to the Graduate School of Pure and
Applied Sciences in Partial Fulfillment of the
Requirements for the Degree of Doctor of
Philosophy in Science

at the
University of Tsukuba

Abstract

We have measured the top quark mass with the dynamical likelihood method. The data corresponding to an integrated luminosity of 1.7fb^{-1} was collected in proton antiproton collisions at a center of mass energy of 1.96 TeV with the CDF detector at Fermilab Tevatron during the period March 2002 - March 2007. We select $t\bar{t}$ pair production candidates by requiring one high energy lepton and four jets, in which at least one of jets must be tagged as a b-jet. In order to reconstruct the top quark mass, we use the dynamical likelihood method based on maximum likelihood method where a likelihood is defined as the differential cross section multiplied by the transfer function from observed quantities to parton quantities, as a function of the top quark mass and the jet energy scale(JES). With this method, we measure the top quark mass to be 171.6 ± 2.0 (stat.+ JES) ± 1.3 (syst.) = 171.6 ± 2.4 GeV/ c^2 .

Acknowledgments

I would like to thank my supervisor Prof. Shinhong Kim. He gave me a chance to go to study at Fermilab and also gave me a constructive advice when I was in difficulties on my studies.

I would also like to thank Prof. Kunitaka Kondo, who is the original proposer of the dynamical likelihood method, and has been taking care of my analysis and daily life during my stays at Fermilab. He made my analysis mature. He also sometimes invited me to his home party and I had a lot of fruitful conversations.

Conveners of CDF Top Group and Top Mass Group gave me a lot of helps. The Top conveners Prof. Robin D. Erbacher and Prof. Kirsten Tollefson encourage me and lead to finish my analysis. The Top Mass Conveners Prof. Daniel Whiteson, Prof. Gueorgui Vesselinov Velez and Prof Nick van Remortel made a lot of effort to justify my analysis. I appreciate their kindness and supports.

Prof. Jeremy Lys, Prof Alexander Sukhanov, Prof. Erik Brubaker and Mr. Jahred Adelman, inspected my analysis precisely. The discussions with them brought a deep comprehension of my analysis to me. Kohei Yorita, who is my predecessor of this analysis, also brought a lot of hints to me to understand the dynamical likelihood method.

Prof. Takasumi Maruyama gave me a lot of points of view on not only analysis but also my life at Fermilab. He also taught me a lot of things of SVT, which is one of the trigger system, with great patience.

Dr. Tomonobu Tomura much helped me on my life on Fermilab. I could work and live every day without troubles due to him. And lot of my colleagues supported me on not only studies but also daily life. I would like to thank to Dr. Nobu Oshima, Dr. Koji Sato, Dr. Masato Aoki, Dr. Ryo Tsuchiya, Dr. Yoshiaki Kusakabe, Mr. Junji Naganoma, Mr. Tatsuya Masubuchi, Mr. Naoki Kimura, Miss. Ai Nagano, Mr. Koji Nakamura and Mr. Takayuki Wakisaka. We often went to dinner and drink to everywhere, and also sometimes traveled. I had a good time with doing something with them.

Mr. Stefano Torre, Mr. Alberto Annovi and Mr. Benedetto Di Ruzza, the members of the SVT group, gave me a lot of suggestions and opinions for me to progress jobs on SVT. Especially, Stefano had been waiting for me to finish the jobs on Ghost Buster patiently. He also made my daily life cheerfully at Fermilab.

I would also like to appreciate to the stuffs of my university, Prof. Fumihiko Ukegawa, Prof. Kazuhiko Hara, Prof. Yuji Takeuchi, Dr. Hideki Miyake, Dr. Masakazu Kurata and Dr. Takashi Akimoto. They gave me a lot of suggestions to my analysis.

I would like to say thank you to Mrs. Kyoko Kunori and Mrs. Kazuko Kumashiro. They taking care of administrative issues through their secretary works.

Finally, I would like to grateful to my family. Especially, I deeply appreciate my parents for your support. Thank you very much.

Contents

1	Introduction	1
1.1	The Standard Model	2
1.1.1	The Fundamental Particles	2
1.1.2	Higgs Mechanism	6
1.1.3	Top Quark Physics	9
1.1.4	The Top Quark Mass	14
2	Experimental Apparatus	21
2.1	The Accelerator Complex	21
2.1.1	Proton Production and Boosting	23
2.1.2	Main Injector	23
2.1.3	Antiproton Production	24
2.1.4	Recycler Ring	24
2.1.5	Tevatron	25
2.1.6	Beam Monitors	25
2.2	The CDF Detector	26
2.3	Tracking System	26
2.3.1	Silicon Vertex Detector	28
2.3.2	Central Outer Tracker	28
2.3.3	Time of Flight	28
2.3.4	Magnet	29
2.4	Calorimetry	29
2.4.1	Overview	29
2.4.2	Central Calorimeter	30
2.4.3	Plug Calorimeter Upgrade	31
2.5	Muon Chambers	33
2.5.1	Central Muon Detectors	35
2.5.2	Intermediate Muon Detectors	36
2.6	Data Acquisition and Trigger	36
2.6.1	Level 1 Trigger	36
2.6.2	Level 2 Trigger	38
2.6.3	Level 3 Trigger	38
2.6.4	On-line Monitoring	39

3	Reconstruction and Event Selection	41
3.1	Electron Identification	41
3.2	Muon Identification	43
3.3	Jet Reconstruction	44
3.4	Missing Transverse Energy	49
3.5	Event Selection and Collected Data	50
3.6	Background Composition	51
3.7	Monte Carlo Simulations	54
4	Top Quark Mass Measurement	55
4.1	Dynamical Likelihood Method	55
4.2	Application of DLM for <i>lepton + jets</i> Channel	60
4.2.1	Reconstruction Procedure in <i>lepton+jets</i> Channel	60
4.2.2	Transfer Function	62
4.2.3	TF and Jet Energy Scale	67
4.2.4	Performance of Transfer Function	68
4.2.5	Likelihood Function in <i>l+jets</i> Channel	70
4.2.6	Example of the Likelihood	72
4.2.7	The Likelihood Fit	72
4.3	Performance of the Method	75
4.3.1	Test with Signal Only	75
4.3.2	Pseudo-experiments with Background	76
4.3.3	Top Mass Extraction	76
4.3.4	Sanity Check	80
4.3.5	Pull Width	80
4.3.6	Blind Test	85
5	The Systematic Uncertainty	89
5.1	Residual Jet Energy Scale	89
5.2	Parton Distribution Function	90
5.3	Generator	91
5.4	Initial and Final State QCD Radiation	91
5.5	Background Composition	92
5.6	Background Shape	92
5.7	b-jet Energy Scale	92
5.8	Multiple Interaction	94
5.9	Lepton p_T	94
5.10	NLO	95
5.11	b-tagging Efficiency	95
5.12	Calibration	96
5.13	Background Fraction	96
5.14	Summary of systematic uncertainties	96

6	Results and Discussion	99
6.1	Candidates Events and Results of the Fit	99
6.2	Validation of Statistical Uncertainty	99
6.3	Discussion	102
7	Conclusions	105

List of Figures

1.1	$t\bar{t}$ production processes at Tevatron.	10
1.2	$t\bar{t}$ production cross section measured at CDF in Run I ($\sqrt{s} = 1.8 \text{ TeV}$) and Run II ($\sqrt{s} = 1.96 \text{ TeV}$).	11
1.3	The preliminary Run II CDF result of top mass dependence for top cross section. The mean of the top quark mass is set at $172.0 \pm 2.7 \text{ GeV}/c^2$.	12
1.4	The preliminary production cross section measurement at CDF Run II	13
1.5	A diagram for $t\bar{t}$ production by $q\bar{q}$ annihilation and its decay into lepton + jets channel.	14
1.6	Virtual top quark loops contributing to W and Z masses.	16
1.7	Virtual Higgs boson loops contributing to W and Z masses.	16
1.8	The dashed ellipse represents direct measurements of the W mass from LEP2 and the Tevatron, and the top mass. Diagonal lines of constant Higgs mass are indicated. The lower limit is the $114.4 \text{ GeV}/c^2$ 95% confidence level value from direct searches at LEP2 while theory arguments suggest that the Higgs could not be more massive than 1000 GeV or so.	18
1.9	$\Delta\chi^2 = \chi^2 - \chi_{min}^2$ vs Higgs boson mass M_H . The line shows the best fit. The blue band represents an estimate of the theoretical error due to missing higher order correction. The vertical band shows the 95% confidence level exclusion limit on M_H from the direct search. The dashed curve is the result obtained using the evaluation of $\Delta\alpha_{had}^{(5)}(M_Z^2)$ from [8].	19
1.10	Standard Model(SM) and Minimal Supersymmetric extension to the Standard Model (MSSM) parameter space in terms of current best measurements of top quark and W boson mass	20
2.1	Elevation view of one half of the CDF II detector	27
2.2	Cross section of half CDF II plug calorimeter	32
2.3	η and ϕ coverage of the Run II muon systems	35
2.4	Block diagram of the CDF II Trigger	37
2.5	Design of the CDF on-line consumer framework	40
3.1	Example of dijet balancing in relative jet energy corrections as a function of jet detector η	46

3.2	Relative contributions to uncertainty on jet energy scale corrections.	48
3.3	The plots show the tagging efficiency with top quark Monte Carlo samples	49
3.4	The plots show the false b-tag rate with inclusive jet data.	50
4.1	Summary of analysis procedure.	63
4.2	A concept of event reconstruction. For a given jet, there are a lot of possibilities that the jet originates from a parton. One of these possibilities are called a path. transfer functions give a weight of a path from a jet to a parton. Actually we take 10000 paths in an event. For each path, we calculate a path likelihood, and the path likelihoods are summed up to obtain an event likelihood. Finally a joint likelihood is obtained by multiplying the event likelihoods each other.	64
4.3	E_T dependence of transfer function. Transfer function is divided by 10 bins of E_T . Top and bottom plots is used for light jets and b-jets respectively.	65
4.4	η dependence of transfer function. Transfer function is divided by 3 bins of η . The top and bottom plots are used for light jets and b-jets respectively.	66
4.5	JES dependences of transfer function. JES is calibrated by using this dependence of transfer function. We generated 61 transfer function for each ΔJES ($-3 \leq \Delta JES \leq 3$). This plots shows only 7 transfer functions for each ΔJES . Top and bottom plots is used for light jets and b-jets respectively.	67
4.6	Reconstruction procedure for each ΔJES with transfer function. In this analysis, there are 61 parton quantities which reconstructed by transfer functions for each ΔJES in a path. The 'y' is input jet energy whose ΔJES is fixed, on the other hand, ΔJES for transfer function is changed to obtain 'x', which is parton energy.	68
4.7	The comparisons of W 2-jets and Top 3-jets invariant masses, before and after transfer function is applied. Obviously transfer function improves invariant masses of jet systems compared with those obtained by by Level 5 correction.	69
4.8	Invariant mass for each ΔJES for transfer function, while input jet energy is fixed at $\Delta JES = 0.0$. The x-axis represents ΔJES for transfer function. The y-axis of the left plot shows the invariant mass of hadronic decay W boson and of the right plot show the invariant mass of hadronic decay top quark.	70
4.9	Two examples of the signal event likelihoods as a function of M_{top} and ΔJES with right jet assignment with Monte Carlo simulation. Input top quark mass is $175 \text{ GeV}/c^2$ and input ΔJES is 0.0σ	73

4.10	Two typical signal event likelihoods as a function of M_{top} and ΔJES including wrong jet assignments with Monte Carlo simulation. Input top quark mass is $175 \text{ GeV}/c^2$ and input ΔJES is 0.0σ	73
4.11	Two typical background event likelihoods as a function of M_{top} and ΔJES with Monte Carlo simulation. The left plot is calculated with $Wb\bar{b}$ background and the right plot is calculated with QCD background.	74
4.12	An example of the negative log joint likelihood as a function of M_{top} and ΔJES by a realistic pseudo-experiment with Monte Carlo simulation.	74
4.13	Example of 2D fitting. We take a minimum point of negative log likelihood as top mass and ΔJES . The most inner ellipse represents 1σ	75
4.14	Linearities (left three plots) and Residuals (right three plots) of reconstructed mass for different mass samples with 165, 170, 175, 180 and $185 \text{ GeV}/c^2$, which are obtained by 1D likelihood. Residual is defined by $M_{top}^{reconstructed} - M_{top}^{input}$. The top two plots obtained by using correct jets assignments with matched events with parton, middle two plots obtained by using all possible jets assignments with matched events with parton, and the down two plots obtained by using all possible jets assignments including unmatched events with parton.	77
4.15	Linearities of reconstructed mass for each mass sample with 165, 170, 175, 180 and $185 \text{ GeV}/c^2$, which are reconstructed with 2D likelihood. The top two plots obtained by using correct jets assignments with matched events with parton, the center of two plots obtained by using all possible jets assignments with matched events with parton and the down two plots obtained by using all possible jets assignments including unmatched events with parton.	78
4.16	The top plot shows the reconstructed M_{top} as a function of input M_{top} and the down plot shows the residual reconstructed M_{top} as a function of input M_{top} . Since the bias can be seen due to wrong jet assignments and background contaminations, the bias should be corrected by a mapping function which is discussed in the next section.	79
4.17	2D mapping function. Since wrong jet assignments and background contaminations make the biases of reconstructions, we have to correct these biases with 2D mapping functions.	81
4.18	The residual reconstructed M_{top} as a function of input M_{top} and ΔJES after correction with 2D mapping function.	82
4.19	Sanity check from many pseudo-experiments including the backgrounds after applying 2D mapping function. The plot shows the relation between the input M_{top} and the reconstructed M_{top} for five input ΔJES 's. The slope of the linear fit is consistent with 1.0.	83

4.20	Sanity check from many pseudo experiments including background after applying 2D mapping function. The plot shows the residuals between the input M_{top} and the reconstructed M_{top} for five input M_{top} and five input ΔJES ($5 \times 5 = 25$ in total), fitted to $y = \text{constant}$. The constant from the fit corresponds to 0 within the uncertainty.	84
4.21	The pull width before correction for five mass samples and five input ΔJES . The pull width is 1.37, which means that the statistical uncertainty is underestimated. We have to correct statistical uncertainty by multiplying 1.37.	85
4.22	The pull width after correction by multiplying 1.37.	86
4.23	The left plot shows residuals for each PE including 7 blind samples, second plot shows statistical uncertainties and right plot shows pull distribution	86
4.24	The residuals and pulls for 7 blind samples. All results are found to be consistent with input top masses within their uncertainties and pull widths are almost 1.	87
6.1	The fit result of joint likelihood with 343 events of CDF data before applying correction of 2D mapping function and pull width. The cross mark corresponds to minimum point and blue curve represents one σ	100
6.2	The measured statistical uncertainty with 2D fit which include JES uncertainty is consistent with expected statistical uncertainty with 6k pseudo-experiments. 68.3% of total number of pseudo-experiments are smaller than the observed statistical uncertainty.	101
6.3	Results of top quark mass measurements using different analysis methods at CDF Run II. This figure was updated on March 2007, so this result is not listed in this figure.	103
7.1	The prediction of mass area of Higgs boson with results of DLM using 1.73 fb^{-1} . The black curve represents the results in this analysis. Higgs boson mass is expected to approached to the SM region.	106

List of Tables

1.1	Introduction and the history of six quarks. The number of each mass are in Particle Data Group [6].	3
1.2	Introduction and the history of six leptons. The number of each mass are in Particle Data Group [6].	4
1.3	Introduction and the history of four forces. The number of each mass are in Particle Data Group [6].	5
1.4	The relative magnitudes of the four types of interaction.	6
1.5	A typical mean lifetime τ	6
1.6	Branching ratio for $t\bar{t}$ decay modes in the Standard Model coupling. q stands for a u , d , c or s quark. Decay modes are categorized into four channels: All-jets, Lepton+jets, Di-lepton and τ channels.	15
2.1	Evolution of Tevatron parameters.	22
2.2	Evolution of Tevatron parameters.	23
2.3	Calorimeter segmentation. “had” means Hadron Calorimeter.	30
2.4	Characteristic of CDF II calorimeter. X_0 means one radiation length.	30
2.5	Parameters of muon detection at CDF. Pion interaction length and the limit on resolution due to multiple scattering are computed at $\theta = 90^\circ$ in the central detectors CMU, CMP and CSP; at $\theta = 55^\circ$ in CMX and CSX; and on the entire θ coverage for the IMU.	34
3.1	The jet energy correction levels.	45
3.2	The summary of event selection criteria.	51
3.3	The number of expected events for individual background source.	53
5.1	Residual jet energy scale uncertainties.	90
5.2	The table of pdf systematic uncertainty in GeV/c^2 . We take three kind of PDF systematics summed in quadrature.	91
5.3	The systematic uncertainty for the top quark mass dependence on input generator. We compare Pythia with Herwig.	91
5.4	The systematic uncertainty for ISR and FSR.	92
5.5	The systematic uncertainty from the number of background for 2-D analysis.	93

5.6	The systematic uncertainty from the background shape uncertainty which is obtained using two different Q^2 samples.	93
5.7	The systematic uncertainty for b-jet energy scale.	94
5.8	The systematic uncertainty from effect of lepton p_T	95
5.9	The systematic uncertainty from NLO effect.	95
5.10	The systematic uncertainty from the b-tagging efficiency.	96
5.11	The systematic uncertainty from background fraction.	96
5.12	The total systematic uncertainty.	97

Chapter 1

Introduction

What is the indivisible elements which compose this universe? This is the one of the most attractive questions for human beings from ancient times. Thales considered the world organized from water and Aristoteles considered that the matter is made from the five elements, fire, earth, air, water and aether. In the meantime, Leucippus and Democritus believe that all matter is made up of various imperishable, indivisible elements which they called atom. At the 18th century, Dalton developed the idea of the atomizm and proposed that elements are made of tiny particles called atoms and periodic table of elements had been completed by Mendeleev and others.

Beginning before the turn of the 20th century and, continuing beyond the turn of the 20th century, one of the most important pursuits of physicists has been to understand the elementary nature of matter. In 1897 J.J.Thomson confirmed the corpuscular nature of cathode rays by measuring their charge to mass ratio and identified them as universal constituents of matter. The charge to mass ratio was the same regardless of the source of the cathode rays. So, Thomson had made the first concrete identification what we now consider a fundamental particle, the electron.

Ever since, a lot of particles had been discovered by a lot of efforts of experimenters, and a lot of theorist developed the theory to explain the behavior of these new particles. In the 1970s, a framework to explain particles and their interactions was completed at last, called Standard Model [1, 2, 3].

However, Standard Model has not been fully tested experimentally yet because Higgs boson, which is last one of the composition of Standard Model, has not been observed. So one of the most important mission for experimenters is to observe the Higgs boson. At Fermilab, many experimenters are searching for the Higgs boson directly or indirectly. One of the methods to predict the possible range the Higgs boson mass, is to measure the top quark mass precisely. Top quark is the heaviest quark of six quarks in Standard Model, discovered at 1995 [4, 5], and its mass is important not only for prediction of Standard Model Higgs mass but also for one of the parameters of new theories beyond the Standard Model.

In this thesis, we present the precise measurement of the top quark mass with dynamical likelihood method.

1.1 The Standard Model

1.1.1 The Fundamental Particles

Practically, all experimental results from high energy experiments can be explained by the so-called Standard Model of particle physics, formulated in the 1970s. High precision experiments have repeatedly verified subtle effects predicted by the Standard Model. This theory, which is based on an $SU(3)_C \times SU(2)_L \times U(1)_Y$ gauge group, has proved to be extraordinarily robust. The first gauge group $SU(3)_C$ corresponds to the strong force described by Quantum Chromodynamics(QCD), and the second and third gauge groups, $SU(2)_L \times U(1)_Y$, correspond to the symmetry of the electroweak interactions. $SU(2)_L$ corresponds to the left-handed weak doublets and $U(1)_Y$ is a diagonal phase symmetry. $SU(2)_L \times U(1)_Y$ symmetry breaks into the usual V-A weak interaction and the electromagnetic interactions of Quantum Electrodynamics(QED). There is another known force in the nature, graviton, but its interaction is too weak to be detected in the subatomic experiments. Therefore gravitation is not understood in terms of particle physics, and has not been included in the Standard Model.

The fundamental particles are categorized into three categories - leptons, quarks and gauge bosons as summarized in Tables 1.1-1.3. The leptons carry integral electric charge. The electron e with unit negative charge is familiar to every one, and the other charged leptons are the muon μ and the tau τ . These are heavy versions of the electron. The neutral leptons are called neutrinos denoted by the generic symbol ν . A different flavor of neutrino is paired with each flavor of charged lepton, as indicated by the subscript. Neutrinos were postulated by Pauli in 1930 in order to account for the energy and momentum missing in the process of nuclear β -decay. The actual existence of neutrinos as independent particles, detected by their interactions, was first demonstrated in 1956.

The quarks carry fractional charge, of $+2/3|e|$ or $-1/3|e|$. The quark type or flavor is denoted by a symbol: u for 'up', d for 'down', c for 'charm', s for 'strange', t for 'top' and b for 'bottom'. While leptons exist as free particles, quarks do not. It is a peculiarity of the strong forces between the quarks that they can be found only in combinations such as uud , not singly. This phenomenon of quark confinement is even today, not properly understood.

Protons and neutrons consist of the lightest u and d quarks, three at a time: a proton consists of uud , a neutron consists of ddu . The common material of the present universe is the stable particles, i.e. the electrons e and the u and d quarks. The heavier quarks s, c, b, t also combine to form particles akin to, but much heavier than the proton and neutron, these are unstable and decay rapidly (in typically 10^{13} s) to lighter quarks u or d just as the heavy leptons decay to electrons.

At the present, the Standard Model characterizes the interaction between the leptons and quarks as mediated by another category of particles. These mediator particles are bosons with internal spin 1, obey Bose-Einstein statistics and are called gauge bosons. The four types of bosons are sufficient to explain all phenomena in physics.

Quark	charge	Mass(MeV/c^2)	discovery(year)	short description
1st generation				
up(u)	+2/3	1.5-3	1968	Physicists at the Stanford linear Accelerator Center(SLAC) observe the first evidence for quarks inside the proton. Friedman, Kendall and Taylor receive the 1990 Nobel Prize.
down(d)	-1/3	3-7		
2nd generation				
strange(s)	-1/3	95 ± 25	1951	First observation of kaons in cosmic-ray experiments. Nishijima of Osaka City University and Gell-Mann of Caltech explains the relative longevity of kaons with the concept of strangeness and Gell-Mann receives Nobel Prize in 1969 for the invention of the quark model. At Brookhaven National Laboratory(BNL) Cronin and Fitch find that kaons violate the matter-antimatter (CP) symmetry. They receive the 1980 Nobel Prize.
			1956	
			1964	
charm(c)	+2/3	$1.25 \pm 0.09 \times 10^3$	1974	Physicists at SLAC and BNL discover independently a new particle that contains a new kind of quark, called the charm quark. Richter (SLAC) and Ting (BNL) receive the 1976 Nobel Prize.
3rd generation				
bottom(b)	-1/3	$4.20 \pm 0.07 \times 10^3$	1977	Led by Lederman, a group of scientists at Fermilab discover the upsilon, a particle containing a bottom quark and an anti-bottom quark.
top(t)	+2/3	$1.725 \pm 0.027 \times 10^5$	1995	The CDF and DZero collaborations at Fermilab announce the discovery of the top quark, an elementary particles as heavy as a gold atom.

Table 1.1: Introduction and the history of six quarks. The number of each mass are in Particle Data Group [6].

Lepton	charge	Mass(MeV/c^2)	discovery(year)	short description
1st generation electron(e)	-1	0.51	1897	Using cathode tube, Thomson discovers the electron at the Cavendish laboratory in England. He receives the Nobel Prize in 1906.
electron neutrino (ν_e)	0	$< 2 \times 10^{-6}$	1956	Experimenters led by Cowan and Reines at the Savannah River plant detect the first neutrino. Reines shares the 1995 Nobel Prize.
2nd generation muon(μ)	-1	105.66	1937	Neddermeyer and Anderson discover the muon in a cosmic-ray experiment.
muon neutrino (ν_μ)	0	< 0.19	1962	Scientists at BNL discover the muon neutrino. Lederman, Schwartz and Steinberger receive the 1988 Nobel Prize.
3rd generation tau(τ)	-1	1776.90 ± 0.20	1976	Experiments at SLAC discover the tau lepton, the first observation of a third generation particle. Perl shares the 1995 Nobel Prize.
tau neutrino	0	< 18.2	2000	Fermilab announces first direct evidence for the interaction of a tau neutrino in a detector. Indirect indications for the existence of this particle existed since more than two decades.

Table 1.2: Introduction and the history of six leptons. The number of each mass are in Particle Data Group [6].

Force	charge	Mass(MeV/c^2)	discovery(year)	short description
photon(γ)	0	$< 6 \times 10^{-17}$	1905	Based on Plank's introduction of quanta of energy, Einstein describes the photoelectric effect using light particles called photons. They are carriers of the electromagnetic force. Planck receives the 1918 Nobel Prize, and Einstein is honored in 1921.
gluon(g)	0	0	1979	At the Deutsches Elektronen-Synchrotron (DESY) in Germany, scientists report evidence for the gluon, the carrier of the strong force.
electroweak				
(W)	± 1	$80.403 \pm 0.029 \times 10^3$	1983	Physicists at the European research CERN observe the W and Z bosons, the only force carriers with mass. Rubbia and van der Meer receive the 1984 Nobel Prize.
(Z)	0	$91.1876 \pm 0.0021 \times 10^3$		

Table 1.3: Introduction and the history of four forces. The number of each mass are in Particle Data Group [6].

- **The strong force** is responsible for quarks “sticking” together to form protons, neutrons and related particles. The gluon mediates the strong force; it glues quarks together.
- **The electromagnetic force** binds electrons to atomic nuclei (clusters of protons and neutrons) to form atoms. The photon carries the electromagnetic force; it is a quantized particle of light wave.
- **The weak force** facilitates the decay of heavy particles into smaller siblings. The W and Z bosons mediate the weak force; they introduce different types of decays.
- **The gravitational force** acts between massive objects. Although it plays no role at the microscopic level, it is the dominant force in our everyday life and throughout the universe. It has been expected that the gravitational force may also be associated with a boson particle named as the graviton.

To indicate the relative magnitudes of the four types of interaction, relative strengths of the force between two protons when just in contact are very roughly shown in Table 1.4.

strong	electromagnetic	weak	gravity
1	10^{-2}	10^{-7}	10^{-39}

Table 1.4: The relative magnitudes of the four types of interaction.

The timescale for the decay of unstable particles via one or other of the fundamental interactions are also very different. As listed in Table 1.5, a typical mean lifetime τ for decay through a weak interaction is $10^{-10}s$, which is easily measurable, while that for a strong interaction will be about $10^{-23}s$, which cannot be measured directly. An unstable particle has the Breit-Wigner type mass, distribution with a decay width $\Gamma = \hbar/\tau$. So, when τ is very short, its value can be inferred from the measured width Γ .

	strong	electromagnetic	weak	gravity
Typical lifetime(seconds)	10^{-23}	10^{-20}	10^{-10}	-

Table 1.5: A typical mean lifetime τ .

1.1.2 Higgs Mechanism

From the very beginning of the Standard Model history, scientists tried to find mechanisms, that would break the $SU(2)_L \times U(1)_Y$ symmetry, allowing the mass terms of

quarks, leptons and gauge bosons to be present in the Lagrangian. We introduce a field ϕ called the Higgs field [7],

$$\phi = \begin{pmatrix} \phi^+ \\ \phi^0 \end{pmatrix} \quad (1.1)$$

which behaves as a complex scalar under Lorentz transformations and as a doublet under $SU(2)_L$ isospin transformation with isospin $T_\phi = \frac{1}{2}$ and hyper-charge $Y_\phi = \frac{1}{2}$. Its kinematic, mass and interaction terms are described by the standard normalizable Lagrangian of scalar particles:

$$\mathcal{L}_{scalar} = (\mathcal{D}_\mu \phi)^\dagger \mathcal{D}^\mu \phi - V(\phi) \quad (1.2)$$

where the covariant derivative \mathcal{D}_μ and the potential $V(\phi)$ are:

$$\mathcal{D}_\mu = \partial_\mu + ig' B_\mu \frac{Y}{2} + \frac{ig}{2} \vec{\tau} \cdot \vec{b}_\mu \quad (1.3)$$

$$V(\phi) = \mu^2 \phi^\dagger \phi + \lambda (\phi^\dagger \phi)^2 \quad (1.4)$$

Notice that μ^2 is the parameter with dimension 2. The dimensionless λ parameter is chosen to be positive in order to have the scalar potential. The Lagrangian of Eq. 1.2 is invariant under $SU(2)_L \times U(1)_Y$ symmetry, therefore we can add it to the electroweak Lagrangian

$$\mathcal{L}_{EWK} = \mathcal{L}_{gauge} + \mathcal{L}_{lepton} + \mathcal{L}_{quark} \quad (1.5)$$

where

$$\mathcal{L}_{lepton} = \sum_{l=e,\mu,\tau} \bar{R}_l i A^\mu (\partial_\mu + ig' B_\mu Y) R_l + \sum_{l=e,\mu,\tau} \bar{L}_l i A^\mu (\partial_\mu + ig' B_\mu Y + \frac{ig}{2} \vec{\tau} \cdot \vec{W}_\mu) L_l \quad (1.6)$$

where

$$R_l = e_R, \mu_R, \tau_R \quad (1.7)$$

$$L_l = \begin{pmatrix} \nu_e \\ e^- \end{pmatrix}, \begin{pmatrix} \nu_\mu \\ \mu^- \end{pmatrix}, \begin{pmatrix} \nu_\tau \\ \tau^- \end{pmatrix} \quad (1.8)$$

$$\mathcal{L}_{quark} = \sum_{q=u,d,c,s,t,b} \bar{R}_q i A^\mu (\partial_\mu + ig' B_\mu Y) R_q + \sum_{q=1,2,3} \bar{L}_q i A^\mu (\partial_\mu + ig' B_\mu Y + \frac{ig}{2} \vec{\tau} \cdot \vec{W}_\mu) L_q \quad (1.9)$$

where

$$R_q = u_R, d_R, c_R, s_R, t_R, b_R \quad (1.10)$$

$$L_q = \begin{pmatrix} u_L \\ d_L \end{pmatrix}, \begin{pmatrix} c_L \\ s_L \end{pmatrix}, \begin{pmatrix} t_L \\ b_L \end{pmatrix} \quad (1.11)$$

$$\mathcal{L}_{gauge} = -\frac{1}{4} W_{\mu\nu}^a W_a^{\mu\nu} - \frac{1}{4} B_{\mu\nu} B^{\mu\nu} \quad (1.12)$$

with

$$B_{\mu\nu} = \partial_\nu B_\mu - \partial_\mu B_\nu, \quad W_{\mu\nu}^a = \partial_\nu W_\mu^a - \partial_\mu W_\nu^a + g\epsilon_{jk}^a W_\mu^j W_\nu^k \quad (1.13)$$

If $\mu^2 > 0$, then the Lagrangian L_{scalar} describes a QED theory with a massless photon B_μ and two real scalar particles ϕ and ϕ^* with the same mass $\sqrt{\mu^2}$. If we consider the other case, namely $\mu^2 < 0$, then the scalar potential $V(\phi)$ has a non-vanishing minimum and the Higgs field gets a non-zero vacuum expectation value $\langle \phi^\dagger \phi \rangle = -\frac{1}{2}\mu^2/\lambda$. By choosing the vacuum expectation value (VEV) of the Higgs to be

$$\langle \phi \rangle = \begin{pmatrix} 0 \\ v/\sqrt{2} \end{pmatrix} \quad (1.14)$$

where $v/\sqrt{2} \equiv \sqrt{(-\frac{1}{2}\mu^2)/\lambda}$, we can redefine the field ϕ of Eq.1.1 by introducing four new real scalar fields $\vec{\xi}(x)$, $H(x)$ by the expression:

$$\phi(x) \equiv \exp\left(\frac{i\vec{\xi}(x) \cdot \vec{\tau}}{2v}\right) \begin{pmatrix} 0 \\ (v + H(x))/\sqrt{2} \end{pmatrix} \quad (1.15)$$

by choosing $\vec{\beta} = \frac{\vec{\xi}}{gv}$ in the $SU(2)$ gauge transformations, we can eliminate the ξ field to obtain the Higgs field in the following form:

$$\phi(x) \rightarrow \phi'(x) = \frac{1}{\sqrt{2}} \begin{pmatrix} 0 \\ (v + H(x)) \end{pmatrix} \quad (1.16)$$

Substituting Eq.(1.16) into \mathcal{L}_{scalar} of Eq.(1.2) we obtain

$$\mathcal{L}_{scalar} = \frac{1}{2}(\partial_\mu H(x))^2 + \frac{1}{4}g^2 W_\mu^+ W^{-\mu}(v + H(x))^2 \quad (1.17)$$

$$+ \frac{1}{8} \frac{e^2}{\sin^2 \theta_W \cos^2 \theta_W} Z_\mu^0 Z^{0\mu} (v + H(x))^2 \quad (1.18)$$

$$+ (\mu^2 (\frac{1}{2}(v + H(x))^2)) + \lambda (\frac{1}{4}(v + H(x))^4) \dots \quad (1.19)$$

where $A_\mu = B_\mu \cos \theta_W + W_\mu^3 \sin \theta_W$, $Z_\mu^0 = -B_\mu \sin \theta_W + W_\mu^3 \cos \theta_W$, $W_\mu^\pm = \frac{W_\mu^1 \mp i W_\mu^2}{\sqrt{2}}$ are the physical states of the photon γ , Z_μ^0 and W^\pm vector bosons. Note that the neutral Higgs field does not couple to the photon. After regrouping Eq.(1.19) we can read out the Higgs and gauge bosons masses.

$$m_H^2 = -2\mu^2 = 2\lambda v^2 \quad (1.20)$$

$$m_W = g \frac{v}{2} \quad (1.21)$$

$$m_Z = \frac{m_W}{\cos^2 \theta_W} \quad (1.22)$$

$$m_\gamma = 0 \quad (1.23)$$

By introducing the Higgs field, so far we were able to give masses to the vector bosons, but the scalar field is still decoupled from the fermionic sector and the fermions are still massless. The solution to this problem is hidden in the following Yukawa coupling terms, which for the first family:

$$\mathcal{L}_{Yukawa} = -(\lambda_u \bar{R}_u \bar{\phi}^\dagger \cdot L_u + \lambda_d \bar{R}_d \bar{\phi}^\dagger \cdot L_d + \lambda_e \bar{R}_e \bar{\phi}^\dagger \cdot L_e + h.c.) \quad (1.24)$$

where λ_u , λ_d and λ_e are the Yukawa coupling constants. This Lagrangian is also invariant under electroweak symmetry and can be added to Eq.(1.5). We demonstrate how fermions acquire their masses using the first family leptons only. By plugging the Higgs field from Eq.(1.16) into \mathcal{L}_{Yukawa} we obtain the electron mass term as well as a term describing the coupling of the Higgs to electrons,

$$\mathcal{L}_{Yukawa}^{electron} = -\lambda_e \frac{v + H(x)}{\sqrt{2}} (\bar{e}_R e_L + \bar{e}_L e_R) = -m_e \psi_{\bar{e}} \psi_e - \frac{\lambda_e}{\sqrt{2}} H \psi_{\bar{e}} \psi_e \quad (1.25)$$

where the electron mass is

$$m_e = \frac{v \lambda_e}{\sqrt{2}} \quad (1.26)$$

Similar procedure is applied to the charged leptons in other generations and to the quarks. The Standard Model has successfully explained many phenomena observed in particles physics experiments over several decades, and no clear sign of its contradiction with nature has been reported yet. On the other hand, it is fundamental to feed the correct input parameters in order for this theory to work. The mass of the top quark is one of such input parameters which the Standard Model is incapable of predicting. Especially, the mass of the top quark is the heaviest among the elementary particles discovered so far. At the same time, it is an exciting coincidence that the mass of the top quark is very close to the vacuum expectation value of the Standard Model. The precision measurement of the top quark mass will play an important role in revealing the mechanism of the Electroweak Symmetry Breaking closely related the properties of the Higgs particle.

1.1.3 Top Quark Physics

The discovery of the top quark in 1995 provided dramatic confirmation of the essential validity of the Standard Model, since the top quark is the last of the known or needed constituents of matter. Fermilab scientists have researched the top quark physics for past 10 years since its discovery using Fermilab Tevatron. Several properties of the top quark have already been examined at the CDF Run II experiment, one of the Fermilab Tevatron experiments. These include studies on the top quark production cross sections [9, 10, 11, 12, 13, 14, 15, 16, 17], the measurements of the top quark mass [18, 19, 20, 21, 22, 23, 24, 25], the search for single top quark production [26], the search for anomalous kinematics [27], the measurement of $B(t \rightarrow Wb)/B(t \rightarrow Wq)$ [28],

the search for $t \rightarrow \tau \nu q$ [29], the search for charged Higgs bosons [30], the measurement of the helicity of W Bosons [31], the search for V+A current [32] and the search for anomalous semi leptonic decay of heavy flavor hadrons [33].

The top quark is, according to the Standard Model, a spin 1/2 and charge 2/3 fermion, transforming as a color triplet under the group $SU(3)_C$ of the strong interactions and as the weak-isospin partner of the bottom quark. None of these quantum numbers has been directly measured so far, although a large amount of indirect evidence supports these assignments.

The top quark is produced predominately in top antitop pairs at the Tevatron via the strong interaction. At a center of mass energy \sqrt{s} of 1.96 TeV, the processes $q\bar{q} \rightarrow t\bar{t}$ and $gg \rightarrow t\bar{t}$ occur approximately 85% and 15% of the time, respectively. The leading order diagrams for the two processes are shown in Figure 1.1. The total cross section for the pair production of top quark is theoretically calculated to be $6.7^{+0.7}_{-0.9}$ pb [34]. Figure 1.2 summarizes the total cross section measured at CDF experiment in Run I and Run II compared to the prediction of the Standard Model. And also, the latest CDF Run II results are presented as shown in Figures 1.3 and 1.4.

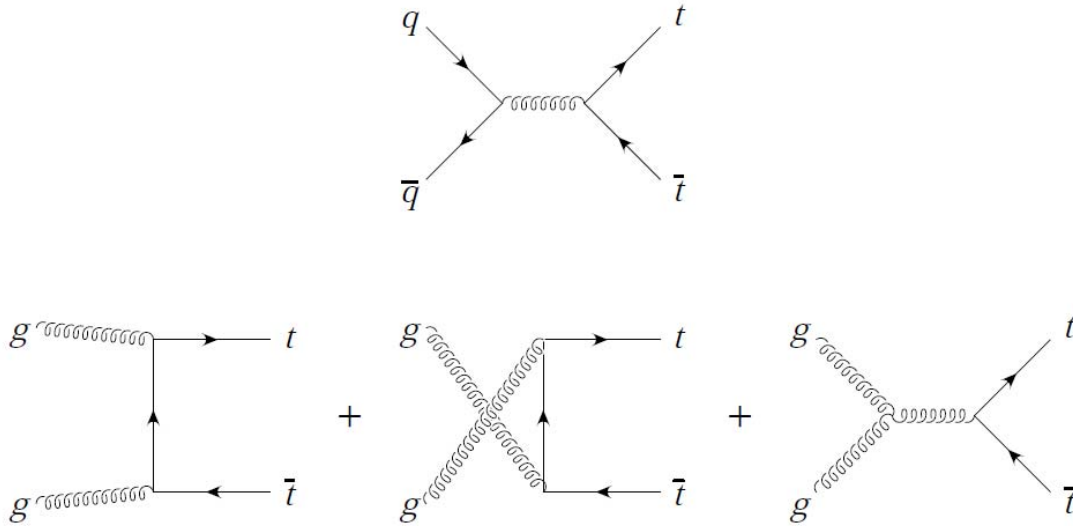


Figure 1.1: $t\bar{t}$ production processes at Tevatron.

The top quark decay occurs by the electroweak interaction. Flavor changing neutral currents are forbidden in the Standard Model due to the GIM mechanism [35]. According to the Standard Model, top quark decays 100% of the time into a W boson and a b quark. The decays are rapid without forming hadrons, and occur almost exclusively through the single mode $t \rightarrow Wb$. The final signatures of the $t\bar{t}$ production are categorized into four categories, di-lepton, lepton+jets, all-hadronic and τ channels, due to the decay modes of the two W bosons produced in the decays of top and anti-top

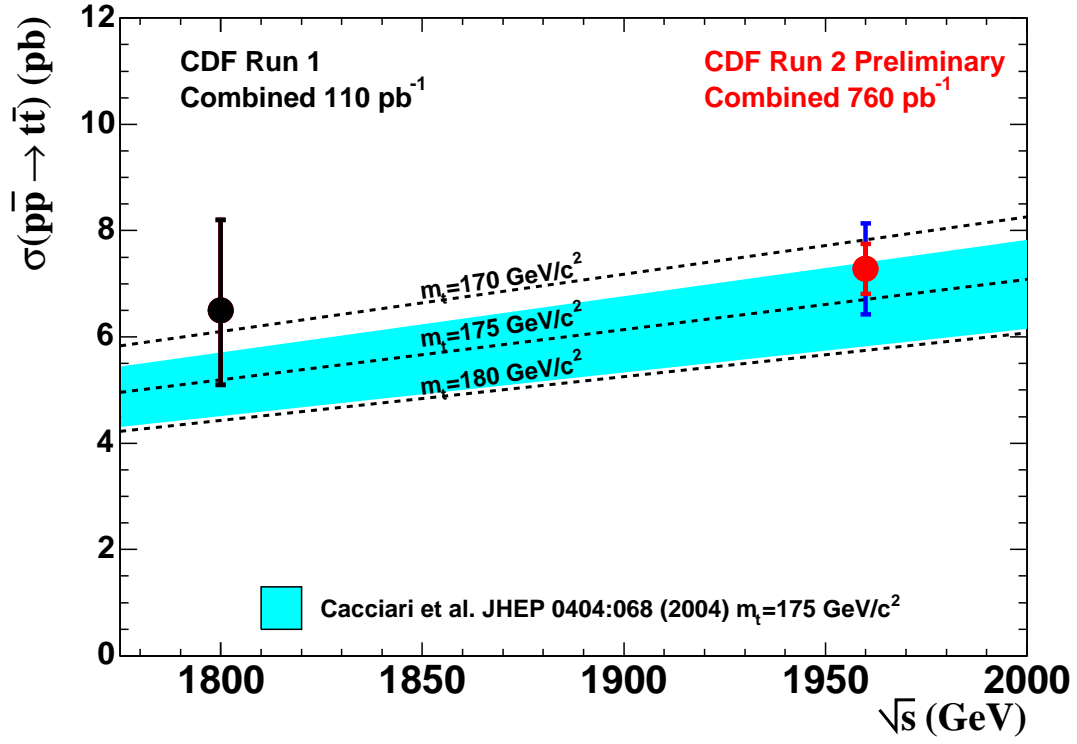


Figure 1.2: $t\bar{t}$ production cross section measured at CDF in Run I ($\sqrt{s} = 1.8$ TeV) and Run II ($\sqrt{s} = 1.96$ TeV).

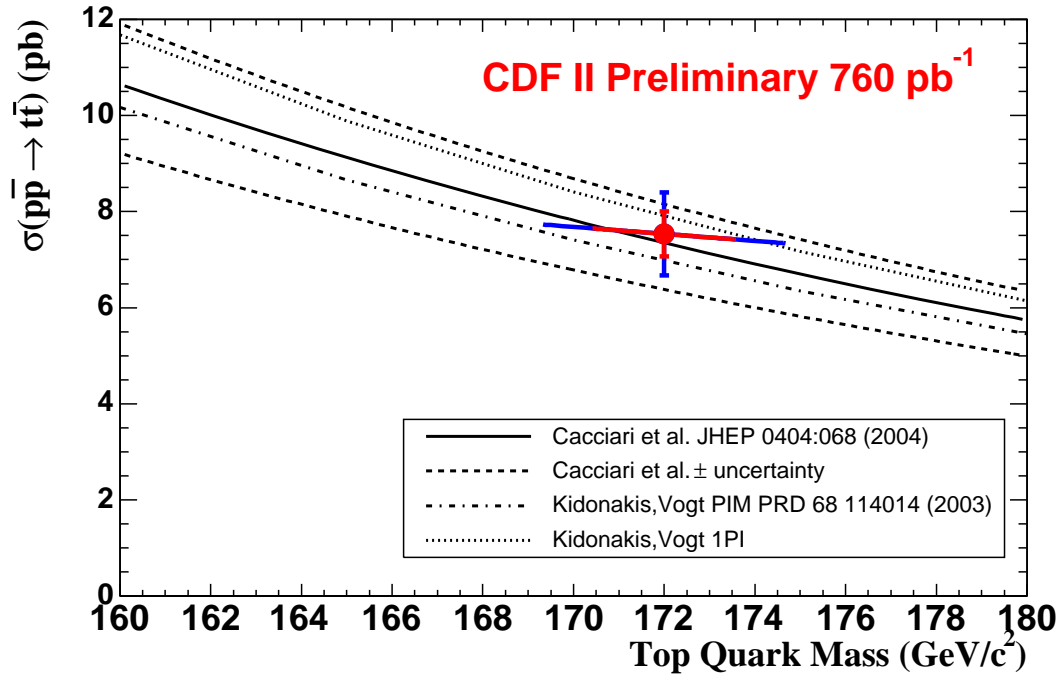


Figure 1.3: The preliminary Run II CDF result of top mass dependence for top cross section. The mean of the top quark mass is set at $172.0 \pm 2.7 \text{ GeV}/c^2$

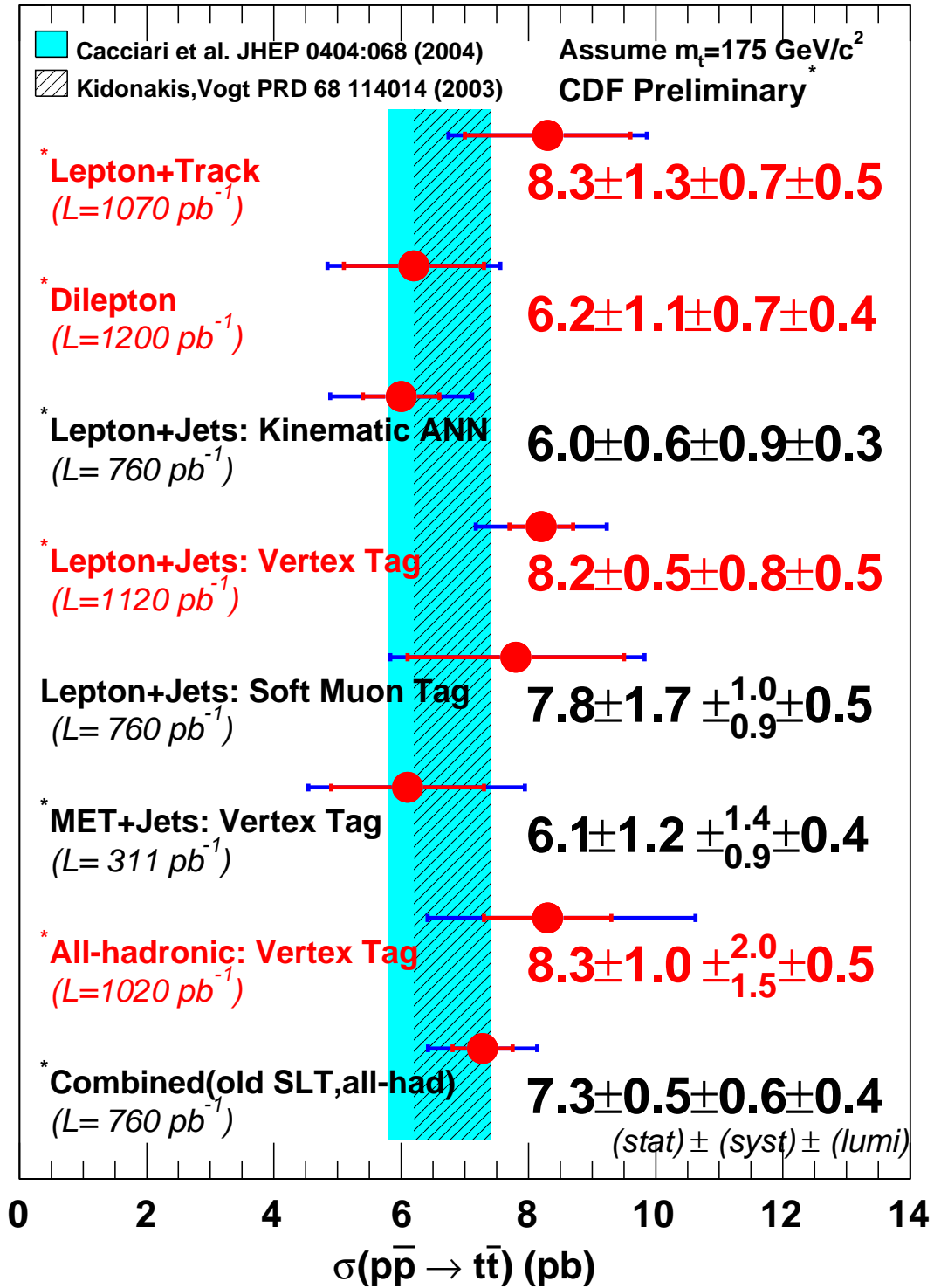


Figure 1.4: The preliminary production cross section measurement at CDF Run II

quarks. Although the τ particle is a lepton, its identification requires a complicated analysis technique due to its short lifetime. So the decay modes involving τ particle are categorized into an independent channel.

Figure 1.5 is a diagram showing the lepton + jets decay of $t\bar{t}$ pair. Table 1.6 summarizes the categorization of the decay modes, with the branching ratio at the tree-level.

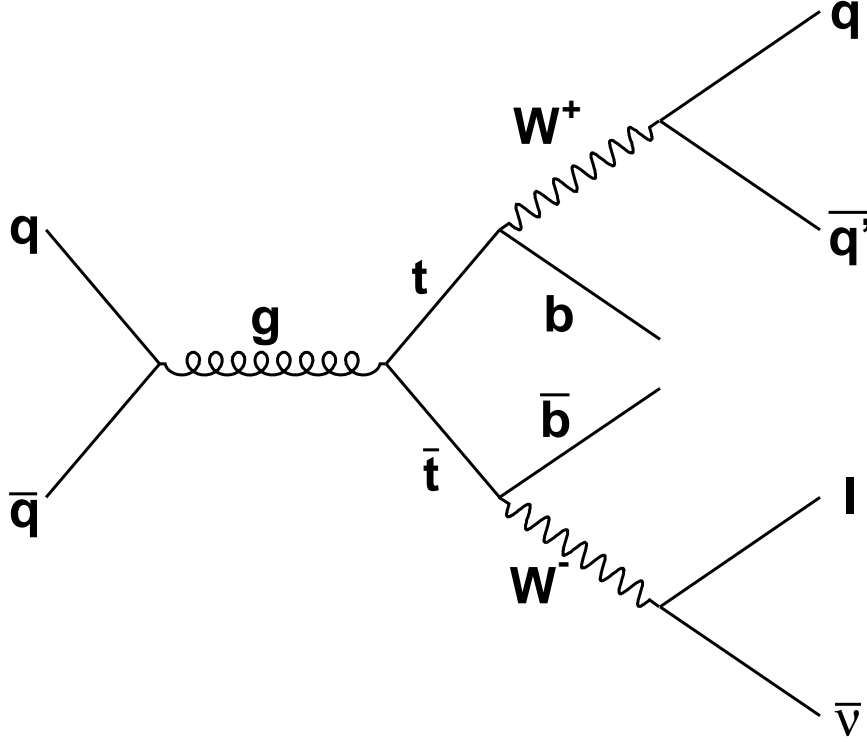


Figure 1.5: A diagram for $t\bar{t}$ production by $q\bar{q}$ annihilation and its decay into lepton + jets channel.

1.1.4 The Top Quark Mass

The top quark mass is one of most fundamental properties of the top quark. Therefore, CDF Run II Top group also has taken a lot of effort to determine its mass precisely. Thereby, the main purpose of this thesis is to measure this top quark mass as well.

After discovering the top quark, meanwhile, the Higgs boson was the last particle which is not discovered in the Standard Model. A lot of experimenters at Fermilab have made much effort to search for the Higgs boson for many years, nevertheless they are still not recompensed for their efforts yet. However we can predict the mass of Higgs boson indirectly by precise measurements of the masses of W boson and top quark. In the Standard Model, tree-level, leading-order Feynman diagrams like that of $t\bar{t}$ production and decay in Figure 1.5 do not describe the physical process completely.

Decay mode	Branching Ratio	Channel Category
$t\bar{t} \rightarrow (qq'b)(q\bar{q}'\bar{b})$	36/81	All-hadronic
$t\bar{t} \rightarrow (qq'b)(e\nu\bar{b})$	12/81	Lepton + jets
$t\bar{t} \rightarrow (qq'b)(\mu\nu\bar{b})$	12/81	Lepton + jets
$t\bar{t} \rightarrow (qq'b)(\tau\nu\bar{b})$	12/81	τ channel
$t\bar{t} \rightarrow (e\nu\bar{q}'b)(\mu\nu\bar{b})$	2/81	Di-lepton
$t\bar{t} \rightarrow (e\nu\bar{q}'b)(\tau\nu\bar{b})$	2/81	τ channel
$t\bar{t} \rightarrow (\mu\nu\bar{q}'b)(\tau\nu\bar{b})$	2/81	τ channel
$t\bar{t} \rightarrow (e\nu\bar{q}'b)(e\nu\bar{b})$	1/81	Di-lepton
$t\bar{t} \rightarrow (\mu\nu\bar{q}'b)(\mu\nu\bar{b})$	1/81	Di-lepton
$t\bar{t} \rightarrow (\tau\nu\bar{q}'b)(\tau\nu\bar{b})$	1/81	τ channel

Table 1.6: Branching ratio for $t\bar{t}$ decay modes in the Standard Model coupling. q stands for a u , d , c or s quark. Decay modes are categorized into four channels: All-jets, Lepton+jets, Di-lepton and τ channels.

We must, in general, include all such Feynman diagrams that have the same incoming and outgoing particle content such as next-leading-order diagrams which include the one loop diagrams. The next-leading-order electroweak calculations involving W or Z bosons are much affected by properties of top quark because of enormous mass of top quark.

Furthermore, as illustrated below, the precise measurement of the top quark mass, along with the W boson mass, provides a constraint on the Higgs boson mass. Such a constraint can bring us a hint in the search for the Higgs boson. At the tree level calculation of the Standard Model, there is an equation,

$$M_W^2 = \frac{\frac{\pi\alpha}{\sqrt{2}G_F}}{\sin^2\theta_W} \quad (1.27)$$

where M_W , α , G_F and θ_W are the W boson mass, the fine structure constant, the Fermi coupling constant and the electroweak mixing angle, respectively. At one loop calculation, tree-level expression is modified as:

$$M_W^2 = \frac{\frac{\pi\alpha}{\sqrt{2}G_F}}{\sin^2\theta_W(1 + \Delta r)} \quad (1.28)$$

where Δr contains the one-loop corrections. The top quark makes a contribution to Δr via the one loop diagrams shown in Figure 1.6, which contribute to the W and Z masses:

$$(\Delta r)_{top} \approx -\frac{3G_F m_t^2}{8\sqrt{2}\pi^2} \frac{1}{\tan^2\theta_W} \quad (1.29)$$

The Higgs boson also contributes to Δr via diagrams shown in Figure 1.7 :

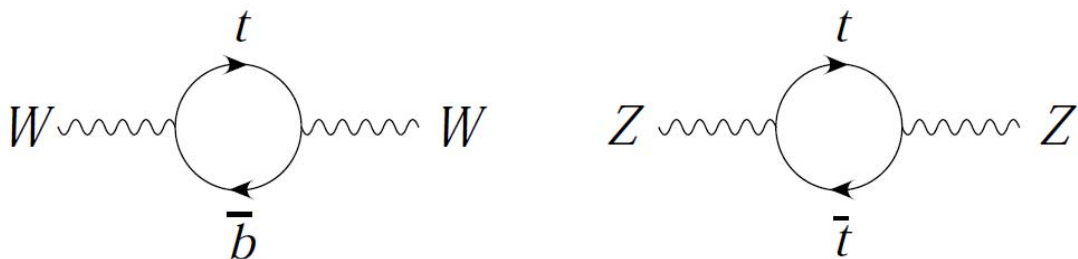


Figure 1.6: Virtual top quark loops contributing to W and Z masses.

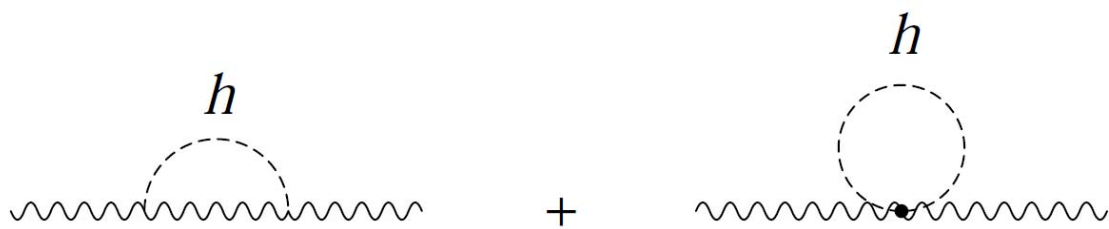


Figure 1.7: Virtual Higgs boson loops contributing to W and Z masses.

$$(\Delta r)_{Higgs} \approx \frac{11G_F M_Z^2 \cos^2 \theta_W}{24\sqrt{2}\pi^2} \ln \frac{m_h^2}{M_Z^2} \quad (1.30)$$

Thus measuring the masses of the W boson and the top quark allows us to predict the mass of the Higgs boson, in the context of the Standard Model, as shown in Figure 1.8. The dashed ellipse represents direct measurements of the W mass from LEP2 and the Tevatron, and the top mass. Diagonal lines of constant Higgs mass are indicated. The lower limit of the Higgs boson mass is $114.4 \text{ GeV}/c^2$ of 95% confidence level from direct searches at LEP2 while theory arguments suggest that the Higgs could not be more massive than $1000 \text{ GeV}/c^2$ or so. Unfortunately, since the dependence of M_W on m_h is only logarithmic these two measurements alone do not put a tight constraint on m_h . Figure 1.9 further shows the χ^2 as a function of the Higgs mass obtained in a fit of the Standard Model to the electroweak measurements of LEP, SLD and Tevatron.

These figures show that the Higgs boson in the Standard Model exists in lower m_H region if it exists, on the other hand, also indicate that there is a possibility of existence of the beyond the Standard Model. If the Higgs in the Standard Model does not exist, we may probably expect that the Higgs exists in the minimal Supersymmetric extension to the Standard Model (MSSM). Figure 1.10 shows regions of the top quark and W boson mass parameter space consistent with the Standard Model and MSSM. The current best measurements and corresponding uncertainty are described by the blue ellipse, which lies predominantly in the MSSM region. There also may exist the other beyond the Standard Model such as Technicolor model [36, 37, 38] and Top-color model [39, 40] which explain that the scalar Higgs field is replaced by a composite field composed of the top quark and anti-top quark, which is supported by the fact that only the top quark is much heavier than other quarks.

In this thesis, we describe the precise measurement of the top quark mass with dynamical likelihood method. Chapter 1 describes the overview of the Standard Model and the top quark physics, Chapter 2 describes the experimental apparatus at Tevatron accelerator and CDF detector, Chapter 3 describes how we select events that we require for top quark measurement, Chapter 4 explains dynamical likelihood method and the application of this method for the top quark mass measurement, Chapter 5 describes an estimation of systematic uncertainties in our measurement, and Chapter 7 concludes this analysis.

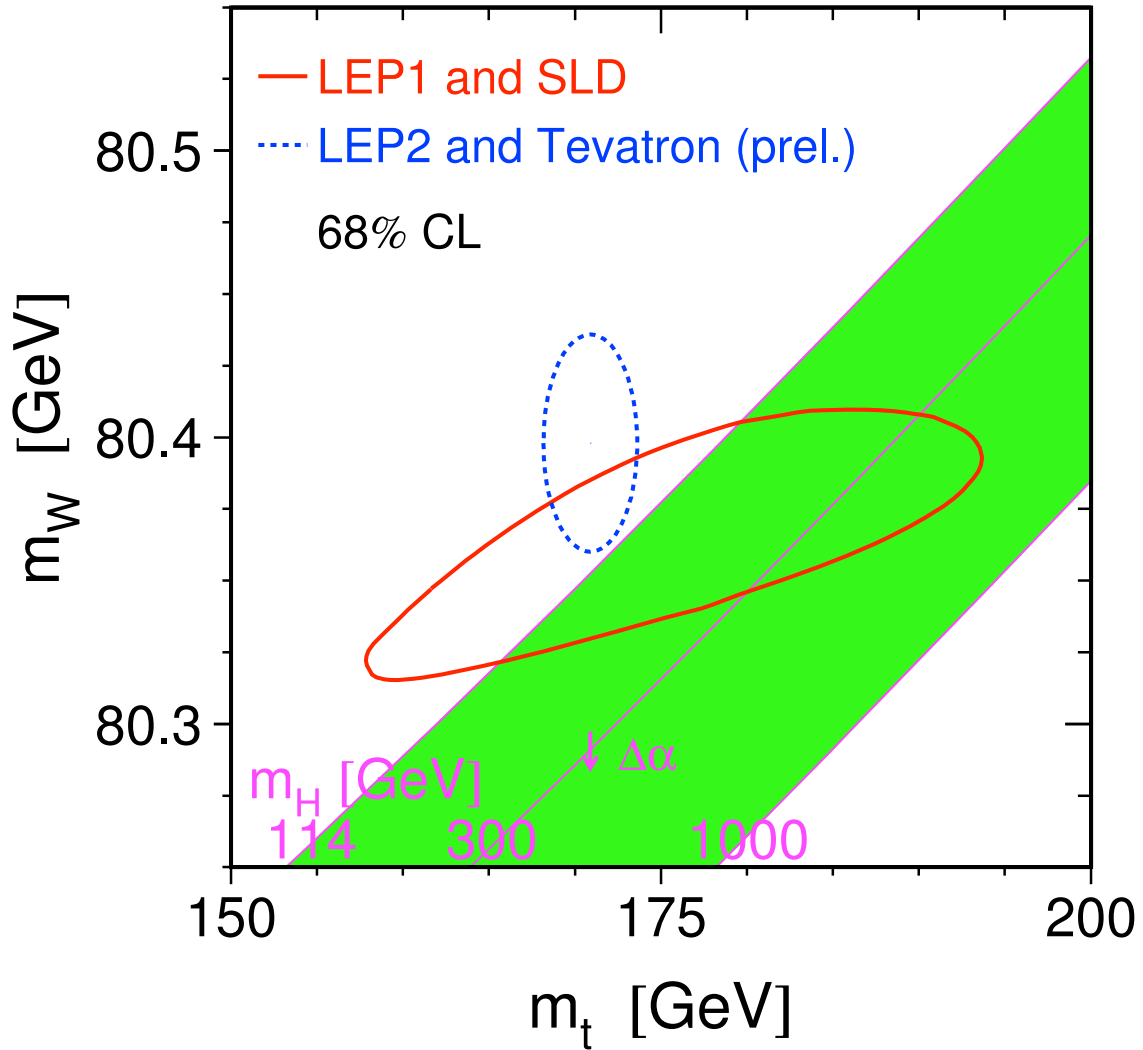


Figure 1.8: The dashed ellipse represents direct measurements of the W mass from LEP2 and the Tevatron, and the top mass. Diagonal lines of constant Higgs mass are indicated. The lower limit is the $114.4 \text{ GeV}/c^2$ 95% confidence level value from direct searches at LEP2 while theory arguments suggest that the Higgs could not be more massive than 1000 GeV or so.

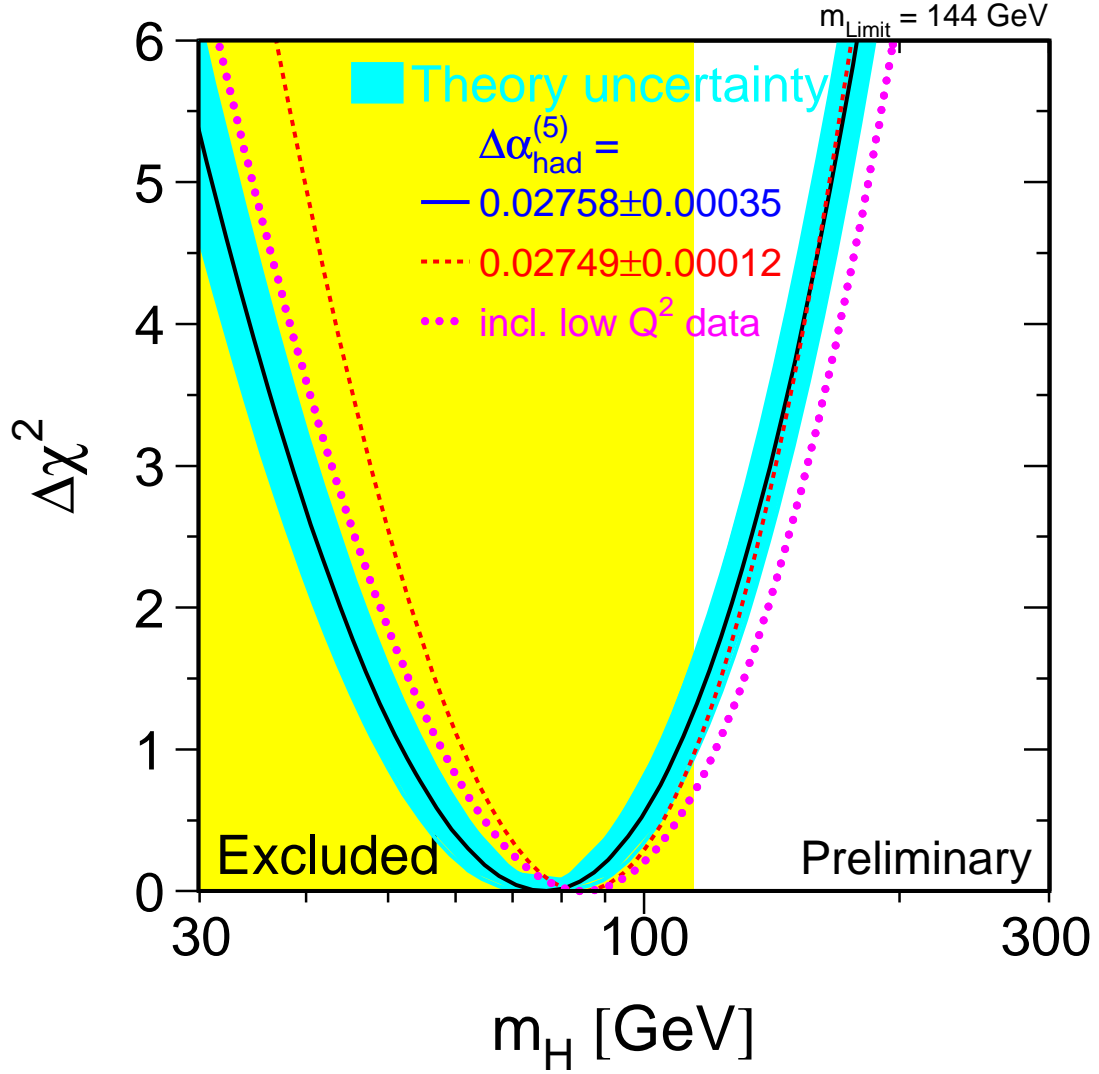


Figure 1.9: $\Delta\chi^2 = \chi^2 - \chi_{min}^2$ vs Higgs boson mass M_H . The line show the best fit. The blue band represents an estimate of the theoretical error due to missing higher order correction. The vertical band shows the 95% confidence level exclusion limit on M_H from the direct search. The dashed curve is the result obtained using the evaluation of $\Delta\alpha_{had}^{(5)}(M_Z^2)$ from [8].

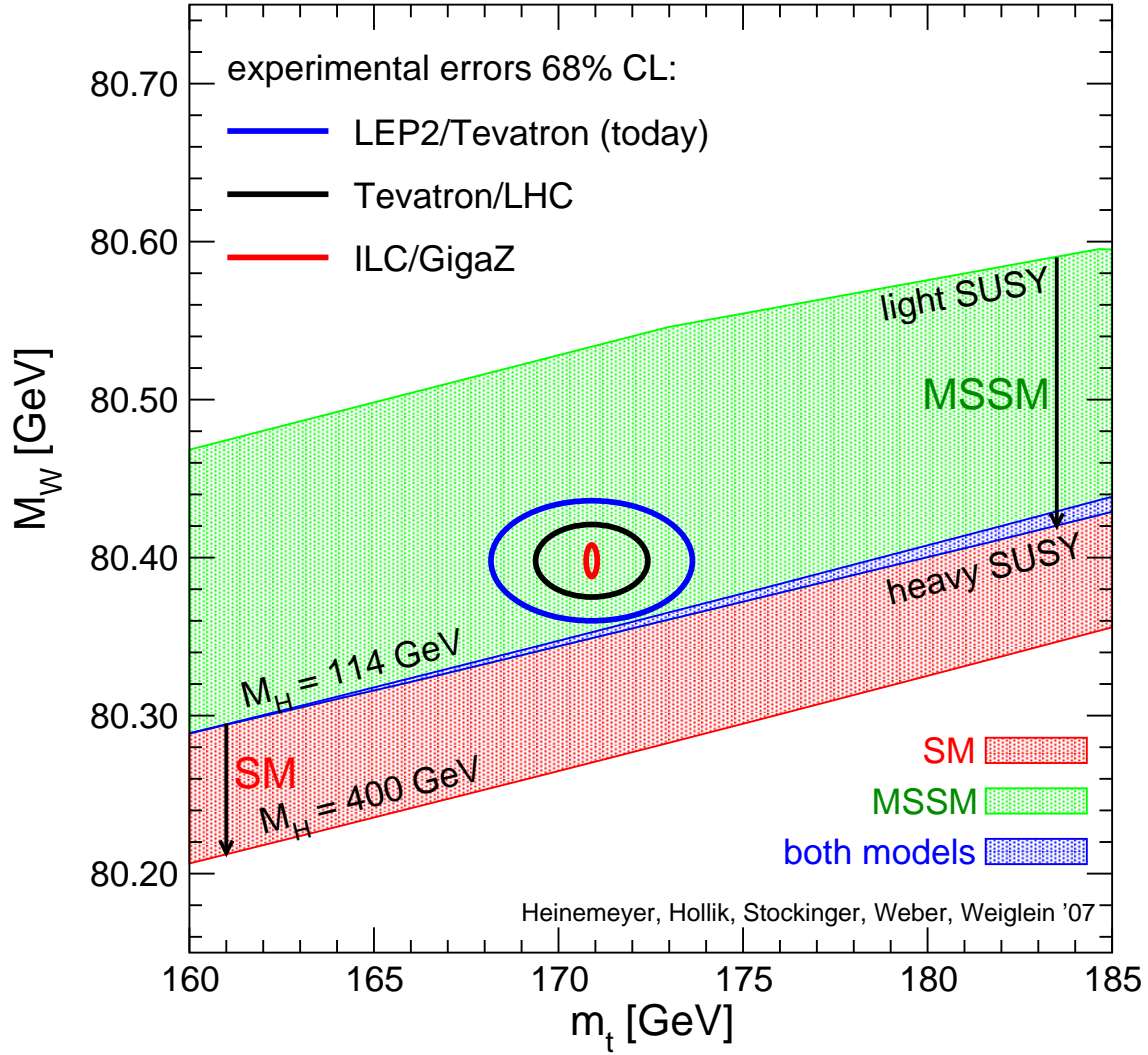


Figure 1.10: Standard Model(SM) and Minimal Supersymmetric extension to the Standard Model (MSSM) parameter space in terms of current best measurements of top quark and W boson mass

Chapter 2

Experimental Apparatus

Particle accelerators are mainly known as research tools in nuclear and high energy particle physics. The Fermilab Tevatron Collider is currently the world highest energy accelerator, where antiprotons collide with protons at a center of mass energy of 1.96 TeV. The Collider Detector at Fermilab (CDF) was constructed by an international collaboration of about 500 Physicists from about 30 American universities and National laboratories plus about 30 groups from universities and national laboratories in Italy, Japan, UK, Canada, Germany, Spain, Russia, Finland, France, Taiwan, Korea and Switzerland. The CDF Detector is 100t weight and about 40' high by 40' x 40' base. The CDF Detector is a complex detector which measures the energy and momenta of particles produced in $p\bar{p}$ collisions. The beams bunches (about 10^{14} to 10^{15} particles per each bunch) of protons and antiprotons collide head-on in the middle of the CDF detector, and a few collisions occur at each bunch collision at every 132 nsec.

2.1 The Accelerator Complex

In the past decade, we have performed physics analyses of several rare physical processes whose cross section is several orders of magnitude smaller than the inelastic $p\bar{p}$ cross section at CDF. In order to obtain sufficiently large samples, several steps have been taken:

- Increase the center-of-mass energy
- Increase the luminosity
- Increase the detector acceptance

The first two steps, and partial reconstruction of the Tevatron, are the topic of the section.

As was stated above, the Run II proton-antiproton center of mass energy has increased to 1.96 TeV from the Run I value of 1.8 TeV. This change provides a major increase in

the reconstructed sample size; for example, the cross section for associated $t\bar{t}$ production grows by 40% with respect to Run I.

Another way to obtain a larger sample is to increase the accelerator's luminosity. In the ideal case, where the proton and antiproton beams collide head-on without a crossing angle and with optimal alignment, the Tevatron's luminosity is given by the formula

$$\mathcal{L} = \frac{fBN_pN_{\bar{p}}}{2\pi(\sigma_p^2 + \sigma_{\bar{p}}^2)} F\left(\frac{\sigma_l}{\beta^*}\right) \quad (2.1)$$

where f is the revolution frequency, B the number of bunches in each beam, N_p and $N_{\bar{p}}$ the number of protons and antiprotons per bunch, σ_p and $\sigma_{\bar{p}}$ the transverse beam sizes (RMS) at the interaction point, and F a form factor that depends on the ratio between the bunch longitudinal RMS size, σ_l , and the beta function at the interaction point, β^* .

Run	1989	IA(1992-93)	IB(1993-95)
p /bunch	1.00E+10	1.20E+11	2.32E+11
\bar{p} /bunch	2.90E+10	3.10E+10	5.50E+10
p emittance (mm mrad)	25	20	23
\bar{p} emittance (mm mrad)	18	12	13
Beta @@ IP (m)	0.55	0.35	0.35
Energy (GeV/particle)	900	900	900
Bunches	6	6	6
Bunch length (rms, m)	0.65	0.55	0.6
Form Factor	0.71	0.62	0.59
Typical \mathcal{L} ($cm^{-2}s^{-1}$)	1.60E+30	5.42E+30	1.58E+31
Best \mathcal{L} ($cm^{-2}s^{-1}$)	2.05E+30	9.22E+30	2.50E+31
$\int \mathcal{L} dt$ (pb^{-1} /week)	0.32	1.09	3.18
Bunch Spacing (nsec)	3500	3500	3500
Interactions/crossing	0.25	0.85	2.48
What's New?		Separators \bar{p} improvements	Linac Upgrade

Table 2.1: Evolution of Tevatron parameters.

As shown in Table 2.1 and 2.2, the most significant improvements in luminosity are obtained by increasing the number of bunches per beam from 6 to 36, while keeping the number of particles per bunch similar to or higher than the Run I figure.

A limiting factor in the choice of accelerator parameters is the superposition of multiple elementary proton-antiproton interactions within the same bunch crossing. At high luminosities, this superposition increases the complexity of the event, making its reconstruction more difficult. Production and acceleration of proton and antiprotons at Fermilab require a chain of accelerators, each boosting particles to higher energies. Each step will be described in the following.

Run	II (2001-)
p /bunch	3.30E+11
\bar{p} /bunch	3.60E+10
p emittance (mm mrad)	30
\bar{p} emittance (mm mrad)	20
Beta @@ IP (m)	0.35
Energy (GeV/particle)	980
Bunches	36
Bunch length (rms, m)	0.43
Form Factor	0.70
Typical \mathcal{L} ($cm^{-2}s^{-1}$)	4-10E+31
$\int \mathcal{L} dt$ (pb^{-1} /week)	8
Bunch Spacing (nsec)	396
Interactions/crossing	2.17
What's New?	Main Injector \bar{p} improvements

Table 2.2: Evolution of Tevatron parameters.

2.1.1 Proton Production and Boosting

The process begins with a **Cockcroft-Walton** accelerator, which feeds negative hydrogen ions to a 150 m linear accelerator. The Linac itself was upgraded in 1993, increasing its energy from 200 MeV to 400 MeV; this made it possible, during Run Ib, to double the number of protons per bunch, and to increase by about 50% the production rate of antiprotons.

After being stripped of electrons, the protons enter the Booster, a synchrotron whose diameter is about 150 m, where they reach a kinetic energy of 8 GeV. Together, Linac and Booster are able to provide pulses of 5×10^{12} protons for antiproton production every 1.5 s, or 6×10^{10} protons per bunch in series of 5 to 7 bunches, repeated 36 times every four seconds.

After leaving the Booster, protons are transferred to the Main Injector, a newly built circular accelerator that replaced the older Main Ring.

2.1.2 Main Injector

The Main Ring was originally built to provide 400 GeV protons to Fermilab's fixed target experiments; later on, it was converted to act as an injector to the Tevatron. The new operational requirements for the Main Ring did not match its original design; therefore, during Run I, the Main Ring was a performance bottleneck. To quote an example, the Main Ring was never able to make full use of the Booster's capabilities: the Main Ring's aperture (12π mm mrad) is only 60% of the Booster's aperture (20π

mm mrad). The situation would be even worse in Run II, with the Booster's aperture at injection increasing to 30π mm-mrad.

The **Main Injector** was designed to solve this problem, while providing further benefits. It is a 3-km circular accelerator, which brings protons and antiprotons from a kinetic energy of 8 GeV to a total energy of up to 150 GeV. Its transverse admittance is larger than 40π mm mrad, more than enough to accommodate particle bunches from the Booster; its emittance is about 12π mm mrad. The maximum beam size is 3×10^{13} particles, divided into up to 504 bunches of 6×10^{10} (anti)protons.

Being more flexible than the Main Ring, the Main Injector can be used in several operation modes:

- Antiproton production;
- Proton and antiproton boosting, before injection into the Tevatron in collider mode;
- Antiproton deceleration, in order to recover unused antiprotons after a Tevatron collision run;
- Proton and antiproton acceleration for fixed target experiments, either directly or as a booster for the Tevatron.

2.1.3 Antiproton Production

In order to produce antiproton, a pulse of 5×10^{12} protons at 120 GeV is extracted from the Main Injector and focused on a nickel target. A lithium lens collects the antiprotons produced by the collision, with a wide acceptance around the forward direction, at energies close to 8 GeV. The antiproton bunches are then moved to Debuncher Ring, where they are transformed into a continuous beam and stochastically cooled, and then to the Accumulator, where they are further cooled. The antiproton stacking rate during Run I was about $7 \times 10^{10} \bar{p}/hour$; Run II upgrades, ranging from antiproton cooling to improving the lithium lens, increases the rate by a factor of three to four. When a sufficient number of antiprotons (up to 10^{12}) is available, stacking is suspended; the antiprotons are further cooled, and then transferred, with an aperture of 10π mm mrad and a $\Delta p/p < 10^{-3}$, to the antiproton Recycler Ring.

2.1.4 Recycler Ring

The Recycler Ring lies in the same enclosure as the Main Injector; contrarily to the other rings at Fermilab, it is built with permanent magnets. During Run I, the antiproton accumulation ring was found to suffer some kind of failure approximately once a week; this led to the loss of the entire store. Permanent magnets, not being prone to the most common causes of failure (such as power loss and lightning) provide a very stable repository for up to 3×10^{12} antiprotons at time.

During Run II, bunches of $2 \cdot 10^{11}$ recently produced antiprotons are transferred from the accumulator to the Recycler Ring every about half an hour, thus keeping the total beam current in the Accumulator small (below 10 mA, compared to the 200 mA antiproton current in Run I).

Antiproton production is one of the limiting factors in the efficiency of Fermilab's colliders. At the end of a store, 75% of the antiprotons are expected to be still circulating in the Tevatron; by recycling 2/3 of these antiprotons, the average luminosity can be increased by a factor of two.

2.1.5 Tevatron

The Tevatron is about 6-km circular accelerator, where protons and antiprotons, rotating in opposite directions inside the same beam pipe, are accelerated from 150 GeV to 1 TeV. Making use of the upgrades in the rest of the accelerator chain, the Tevatron can provide an initial luminosity of $5 \times 10^{31} cm^2 s^{-1}$.

During a collider store, instant luminosity slowly decreases. In the early stages of the store, the most important cause for this decrease is intra-beam scattering; some hours later, the depletion of antiprotons during collisions becomes more relevant. Luminosity is expected to decrease to 50% in about seven hours, and to 1/e in twelve hours. After a typical store duration of eight hours, 75% of the antiprotons are still available; they are decelerated in the Tevatron and in the Main Injector, and then sotred in the Recycler Ring and re-cooled Recycler is not used for the current $p\bar{p}$ collisions.

The Tevatron can also be used in fixed-target mode: it can accelerate up to $3 \cdot 10^{13}$ protons at a time to an energy of 800 GeV, and deliver single bunches to be used in proton, meson and neutrino experiments.

other operational parameters of the Tevatron are listed in Table 2.1 and Table 2.2

2.1.6 Beam Monitors

Operation of colliders at the Tevatron requires a constant monitoring of the beam position and luminosity. From a conceptual point of view, this is done in Run II as it was done in Run I.

The luminosity monitor consists in two arrays of scintillators, placed on both sides of the interaction region. A coincidence of particles moving away from the interaction point, both in the p and \bar{p} direction, is interpreted as contribution to luminosity; bunches of particles moving in a single direction, without a coincident bunch in the opposite direction, are flagged as beam losses.

The beam position, on the other hand, is measured by the collider detectors themselves. During Run I, the detector was able to locate the beam within $5 \mu m$ in about five minutes; other beam parameters, such as slope and transverse profile, were calculated over longer time intervals (about two hours). In Run II, the same operations are performed more quickly.

2.2 The CDF Detector

As stated above, one of the aims of Run II is to reconstruct and store a large sample of rare events. To achieve this results, the number of bunches in each beam increased first by a factor of six with respect to Run I. An immediate consequence is that the time between two successive interactions decreased by the same factor. Several parts of the detectors have been rebuilt from scratch in order to accommodate the higher collision rate.

While the detector was redesigned, efforts were also made to extend its acceptance. The geometrical coverage was increased, by adding new detector elements or enlarging the previously existing ones; the trigger system became able to detect some interesting event features at an earlier stage than in Run I, thus improving the signal to background ratio.

As shown in Fig. 2.1, the tracking system of CDF II is placed inside a superconducting solenoid, while calorimeter and muon systems are outside the magnet. the rest of this chapter will provide a short description of the detector subsystems, with an emphasis on the upgrades since Run I. A complete description of CDF can be found in [41].

In the standard CDF geometry, the \hat{z} axis is oriented along the axis of the solenoid, the \hat{x} axis points away from the center of the Tevatron, and the \hat{y} axis points up. The origin is at the interaction point. The polar angle θ is measured starting from the positive \hat{z} axis; the rapidity y is defined by

$$y = \frac{1}{2} \ln \left(\frac{E + p_z}{E - p_z} \right) \quad (2.2)$$

For the high energy particles, $E \sim p$ and $p_z = p \cos \theta$, hence the pseudo-rapidity is defined as

$$\eta = -\ln \left(\tan \frac{\theta}{2} \right) \quad (2.3)$$

In hadron-hadron collision, a rapidity y (or pseudo-rapidity η), a transverse momentum p_T and an azimuth angle ϕ are usually used. The invariant cross section is written as

$$E \frac{d^3\sigma}{d^3p} = \frac{d^3\sigma}{d\phi dy p_T dp_T} \rightarrow \frac{d^2\sigma}{\pi dy dp_T^2} \quad (2.4)$$

The second form is obtained using the identity $dy/p_z = 1/E$, and the third form represents the average over ϕ . The total multiplicity of particles in collisions is given by $d\sigma/dy$ and this means that the multiplicity is flat in η .

2.3 Tracking System

The innermost parts of the CDF II detector are devoted to tracking charged particles.

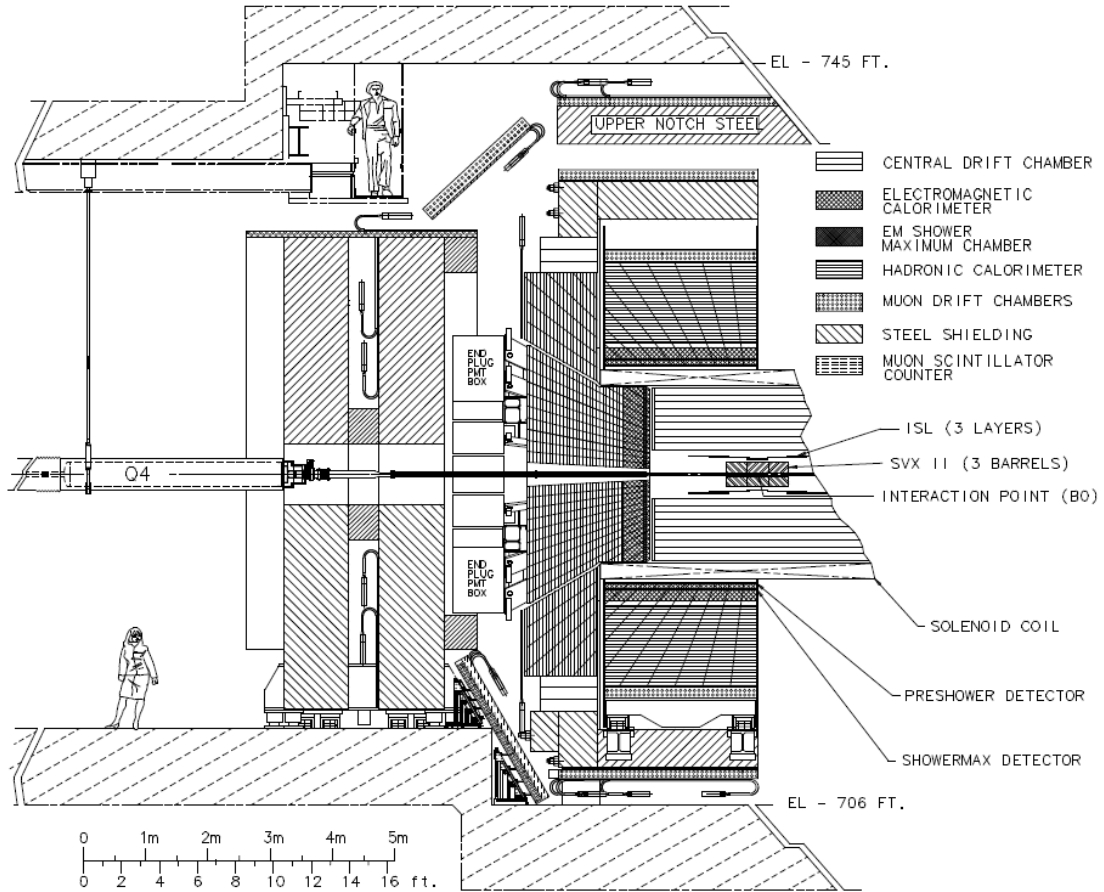


Figure 2.1: Elevation view of one half of the CDF II detector

2.3.1 Silicon Vertex Detector

CDF II makes use of three concentric silicon detectors: “Layer 00”(L00), the Silicon Vertex Detector (SVX II or SVX in short), and the Intermediate Silicon Layers(ISL) [42].

SVX II is the Run II baseline detector. It consists of five layers of double-sided silicon wafers. One side of each wafer provides measurements in the transverse plane (axial strips); the other side’s strips deliver 3D information. SVX II extends radially from 2.5 to 10 cm, and along z up to 45 cm on either side of the interaction point.

The ISL consists of a double sided silicon layer, similar to those in SVX II, placed at $r = 22$ cm in the central η region, and of two forward layers ($1 < |\eta| < 2$) respectively at 20 and 29 cm from the beam line. Together with SVX II, the ISL makes it possible to reconstruct tracks in the forward region, which lies beyond the acceptance region of the outer tracker.

Layer 00 is the most recent addition to the CDF II tracker. It is a single sided, radiation hard silicon layer, placed immediately outside the beam pipe, at $r \simeq 1.5$ cm. Being so close to the interaction point, Layer 00 improves noticeably the impact parameter resolution. In case the innermost SVX II layer suffers from radiation damage during Run II, Layer 00 also acts as a backup.

Compared to the shorter, 4-layer, single-side vertex detector of Run I, the new silicon tracker provides a much wider acceptance, better resolution, three-dimensional reconstruction, and can be used in stand-alone mode, without input from the Central Outer Tracker (described hereafter).

2.3.2 Central Outer Tracker

Outside the silicon detector, at a distance between 40 and 138 cm from the beam, lies the Central Outer Tracker [43]. It is a new open-cell drift chamber, able to reconstruct tracks in the $|\eta| < 1$ region. The COT replaces an older drift chamber, the CTC [44], that would have been unable to cope with the expected occupancy and event rate of Run II.

Each of the eight super-layers of cells consists of twelve layers of sense wires, alternating with field-shaping wires. Axial super-layers alternate with stereo super-layers, thus providing 48 axial and 48 stereo measurements for each track.

In the COT, the cell size is roughly four times smaller than in the CTC. Usage of a faster gas(Ar - Ethane - CF_4 instead of Ar - Ethane) reduces the maximum drift time by a further factor of two, down to 100 ns. This makes the COT immune from event pile-up, even at the highest collision rate of $1/(132 \text{ ns})$.

2.3.3 Time of Flight

A recent addition to CDF II, the time-of-flight detector is an array of scintillator bars, placed at the outer edge of the COT, at a radial coordinate of 140 cm. An accurate measurement of a particle’s time of flight in the CDF tracking volume can be used

quite effectively in particle identification.

Scintillator bars are about three meters long, matching the COT active volume; their thickness (4 cm) is limited by the space which remained available between the previously designed COT and magnet. Their width was determined by occupancy and resolution considerations; the best choice turned out to be also of the order of 4 cm. The bars have a trapezoidal cross section, in order to minimize cracks in the geometry; the scintillating material is Bicron 408, which has a short rise time and long (380 cm) attenuation length.

Photomultiplier tubes, attached to both ends of each bar, provide time and pulse height measurements. By comparing the two pairs of results, the detector determines the instant in which a particle crossed the scintillator with an accuracy of about 100 ps, and the z coordinate of the intersection. The latter measurement is compared to results of 3D track reconstruction in the inner tracking volume, to associate a time of flight to each track.

2.3.4 Magnet

The CDF tracking system are enclosed in a superconducting solenoid, which provides a uniform magnetic field of up to 1.5 T along the detector axis, over a cylindrical fiducial volume 3.5 m long and 2.8 m in diameter.

The solenoid is built of an Al-stabilized NbTi superconductor, able to withstand currents up to 5000 A, and operating at liquid helium temperature. During most of Run I, the magnet operated at 4650 A. corresponding to a current density of 1115 A/m and a central field of 1.14 T.

Although the design lifetime of the solenoid was only ten years, it is possible to reuse the magnet during Run II. The cool-down procedures that were used during Run I limited mechanical stress to the coil, avoiding fatigue damage.

2.4 Calorimetry

2.4.1 Overview

CDF uses scintillator sampling calorimeters, divided into separate electromagnetic and hadronic sections, and providing coverage for $|\eta| \leq 3.64$. The calorimeter was an essential tool in selection and reconstruction of events in Run I; in Run II it continues to measure the energy of photons, electrons, jets, and the missing transverse energy associated to neutrinos and possibly to neutral exotic particles.

Calorimeter calibration can be performed by matching the tracks found in the tracking system to the corresponding calorimetry towers; during Run I, this provided a 2.5% accuracy on jet energy measurements.

The entire calorimeter is segmented into projective towers, whose geometry is summarized in Table 2.3. Each tower consists of alternating layers of passive material (lead for the e.m. section, iron for the hadronic compartment) and scintillator; light from

the WLS is then carried to photomultiplier tubes. Table 2.4 shows the most important characteristics of each calorimeter sector. The central and end-wall calorimeters ($|\eta| < 1.1$) [45, 46] were recycled from Run I; the plug ones ($1.1 < |\eta| < 3.64$) were built anew, to replace an older gas calorimeter that would not be able to function at the increased event rate of Run II.

$ \eta $ range	$\Delta\phi$	$\Delta\eta$
0 - 1.1 (1.2 had)	15°	0.1
1.1 (1.2 had) - 1.8	7.5°	0.1
1.8 - 2.1	7.5°	0.16
2.1 - 3.64	15°	0.2 - 0.6

Table 2.3: Calorimeter segmentation. “had” means Hadron Calorimeter.

	Central and End-wall	Plug
Electromagnetic:		
Thickness	19 X_0 , 1 <i>lambda</i>	21 X_0 , 1 <i>lambda</i>
-per sample (Pb)	0.6 X_0	0.8 X_0
-per sample (scint.)	5 mm	4.5 mm
Light yield	160 p.e./GeV	300 p.e./GeV
Sampling resolution	11.6% / \sqrt{E}	14% / \sqrt{E}
Stochastic resolution	14% / \sqrt{E}	16% / \sqrt{E}
Hadronic		
Thickness	4.5 λ	7 λ
-per sample (Fe)	1 in (central) 2 in (end-wall)	2 in
-per sample	6 mm	6 mm
Light yield	40 p.e./GeV	39 p.e./GeV
Resolution	75% / $\sqrt{E} \oplus 3\%$	80% / $\sqrt{E} \oplus 5\%$

Table 2.4: Characteristic of CDF II calorimeter. X_0 means one radiation length.

2.4.2 Central Calorimeter

Apart from the electrons, the central calorimeter in CDF Run II is the same as used during Run I. The energy measurement response time is already fast enough to accommodate a 132 ns bunch spacing.

Central Electromagnetic Calorimeter

The central electromagnetic calorimeter consists of projective towers of alternating lead and scintillator. The signal is read via a PMMA wavelength shifter, and carried via clear fiber to light yield loss is expected to be around 1% per year; 60% of this loss is explained by the gradual shortening of the attenuation length in the scintillator.

A two-dimensional wire chamber is embedded in the calorimeter, to act as a preshower detector (CPR) which uses the tracker and solenoid coil as radiators. The CPR has proved to be extremely useful in rejection of electron background; it also reduced systematic uncertainties for direct photon measurements by a factor of three [47].

Central Hadronic Calorimeter

The central and end-wall hadronic calorimeters use 23 iron layers as radiator. The scintillator should not suffer radiation damage from measured events.

The hadronic compartment geometry matches the projective towers of the electromagnetic calorimeter.

2.4.3 Plug Calorimeter Upgrade

The CDF II plug calorimeter, shown in Fig. 2.2, covers the η region between 1.1 and 3.64, corresponding to polar angles between 37° and 3° . It replaces an older gas calorimeter, whose response speed was too slow for usage at the CDF II 132 ns inter-bunch. Being based on the same principles as the central calorimeter, the new plug calorimeter also makes experimental data more homogeneous.

The calorimeter is divided in 12 concentric η regions, which are further segmented in 24 (for $|\eta| < 2.11$) or 12 (for $|\eta| > 2.11$) projective towers.

Plug Electromagnetic Calorimeter

The EM section of the plug calorimeter consists of 23 absorber-scintillator layers. A calcium-tin-lead alloy, enclosed between steel plates, is used as absorber.

The first layer of the EM section is used as a preshower detector. In order to distinguish γ from π^0 reliably, the light yield needs to be higher than on other layers. Therefore, the first scintillator layer is thicker (10 mm instead of 6 mm) and made of a brighter material; it is read out separately from the rest of the calorimeter, via multi-anode photomultiplier tubes (MAPMT).

As in the central calorimeter, a shower maximum detector (PES) is also embedded in the plug EM calorimeter, at a depth of about six radiation lengths. The PES consists of eight 45° sectors, each covering six (or three) calorimetric towers in ϕ ; each sector is further segmented in two η regions, in order to reduce occupancy. Within each region, scintillating strips are arranged on two layers, in directions parallel to either edge of the sector; this provides a two-dimensional measurement of the shower. The strips are 5 mm wide and 6 mm thick; they are read out via WLS fibers and MAPMT.

The PES is used to measure the position of electromagnetic showers with an accuracy

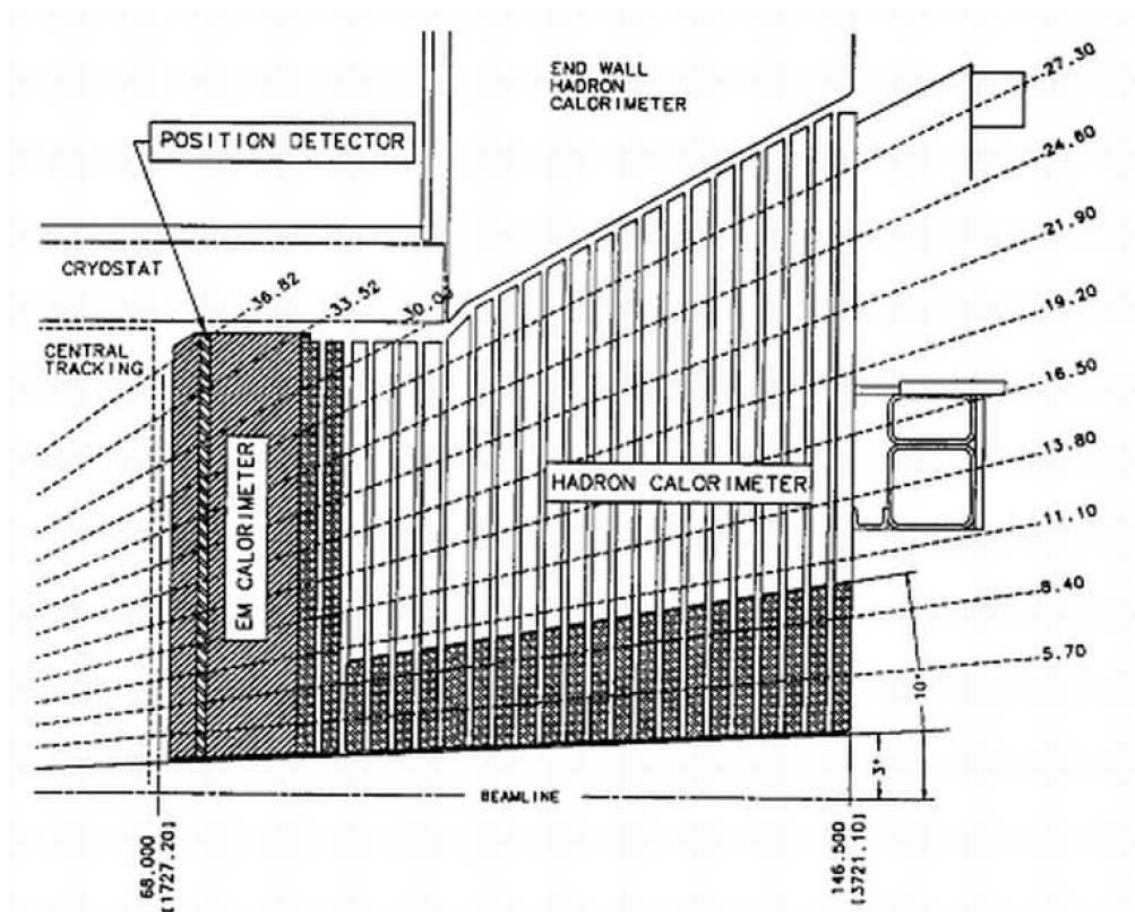


Figure 2.2: Cross section of half CDF II plug calorimeter

reaching 1 mm for high-energy electrons, and to discriminate pions from photons and electrons.

Plug Hadronic Calorimeter

The hadron plug calorimeter was designed to optimize detector performance on b, electroweak and jet physics, and to help in muon detection by analyzing their rate of energy loss. It achieves an energy resolution of about $80\%/\sqrt{E} \oplus 5\%$, which is dominated by the sampling fluctuations from the steel absorber plates. The most strict requirement is that the light yield within each tile should be uniform to 4% or better; dis-uniformity between different tiles is not as important, as the hadron shower usually affects ten or more layers.

2.5 Muon Chambers

The outermost component of CDF II is a set of scintillators, drift tubes and steel absorbers, used for the detection of muons.

During Run I, detection of muons has proved to be an important requirement, both for the analysis of several physics channels and for calibration. For example, a clean sample of W bosons is obtained by reconstructing their muon decay mode; $J/\psi \rightarrow \mu^+\mu^-$ decays are an important part of the heavy quark physics program, as well as a tool to measure systematic effects in the detector.

The tracking improvements from Run I to Run II have a deep impact on muon detection. Before the upgrades, muons in the central region were identified by their penetrating power, and their momentum was measured in the central tracking chamber. On the contrary, the momentum of forward muons had to be measured in the muon chambers themselves, by resorting to a toroidal magnet, as the central tracker only covered the $|\eta| < 1$ region.

With the SVX II upgrade, this distinction falls: measurement of muon momentum can be performed in the central tracker, where the multiple scattering effects are smaller, and the toroidal magnets are not required any longer. Central tracks are measured in the drift chamber; forward tracks ($|\eta| > 1$) are tracked in the silicon only.

Run I central muon chambers (CMU) are reused without major changes; some upgrades which started under Run I (CMP and CSP, the Central Muon/Scintillator Upgrades; CMX and CSX, the Central Muon/Scintillator Extension) are completed; and a new set of chambers, the Intermediate Muon Detector IMU, replaces the previous Forward Muon Detectors (FMU) [48]

Due to their size, muon systems are unable to take data within the Run II inter-bunch interval of 400 or 132 ns; this is not a problem, since the low occupancy of the muon chambers allows integration over multiple events. Scintillators are used to associate muon stubs to the appropriate event.

	CMU	CMP/CSP	CMX/CSX	IMU
η coverage	0 - 0.6	0 - 0.6	0.6 - 1.0	1.0 - 1.5
Drift tubes:				
thickness	2.68 cm	2.5 cm	2.5 cm	2.5 cm
width	6.35 cm	15 cm	15 cm	8.4 cm
length	226 cm	640 cm	180 cm	363 cm
max drift time	$0.8 \mu s$	$1.4 \mu s$	$1.4 \mu s$	$0.8 \mu s$
# tubes (Run Ib)	2304	864	1536	-
# tubes (Run II)	2304	1076	2208	1728
Scintillators:				
thickness	N/A	2.5 cm	1.5 cm	2.5 cm
width	N/A	30 cm	30 - 40 cm	17 cm
length	N/A	320 cm	180 cm	180 cm
# counters (Run Ib)	N/A	128	256	-
# counters (Run II)	N/A	269	324	864
π^0 int. lengths	5.5	7.8	6.2	6.2 - 20
Min P_t (GeV/c)	1.4	2.2	1.4	1.4 - 2.0
MS resol. (cm GeV)	12	15	13	13 - 25

Table 2.5: Parameters of muon detection at CDF. Pion interaction length and the limit on resolution due to multiple scattering are computed at $\theta = 90^\circ$ in the central detectors CMU, CMP and CSP; at $\theta = 55^\circ$ in CMX and CSX; and on the entire θ coverage for the IMU.

Table 2.5 summarizes the information on the muon subsystems; the following sections will describe their characteristics in deeper detail.

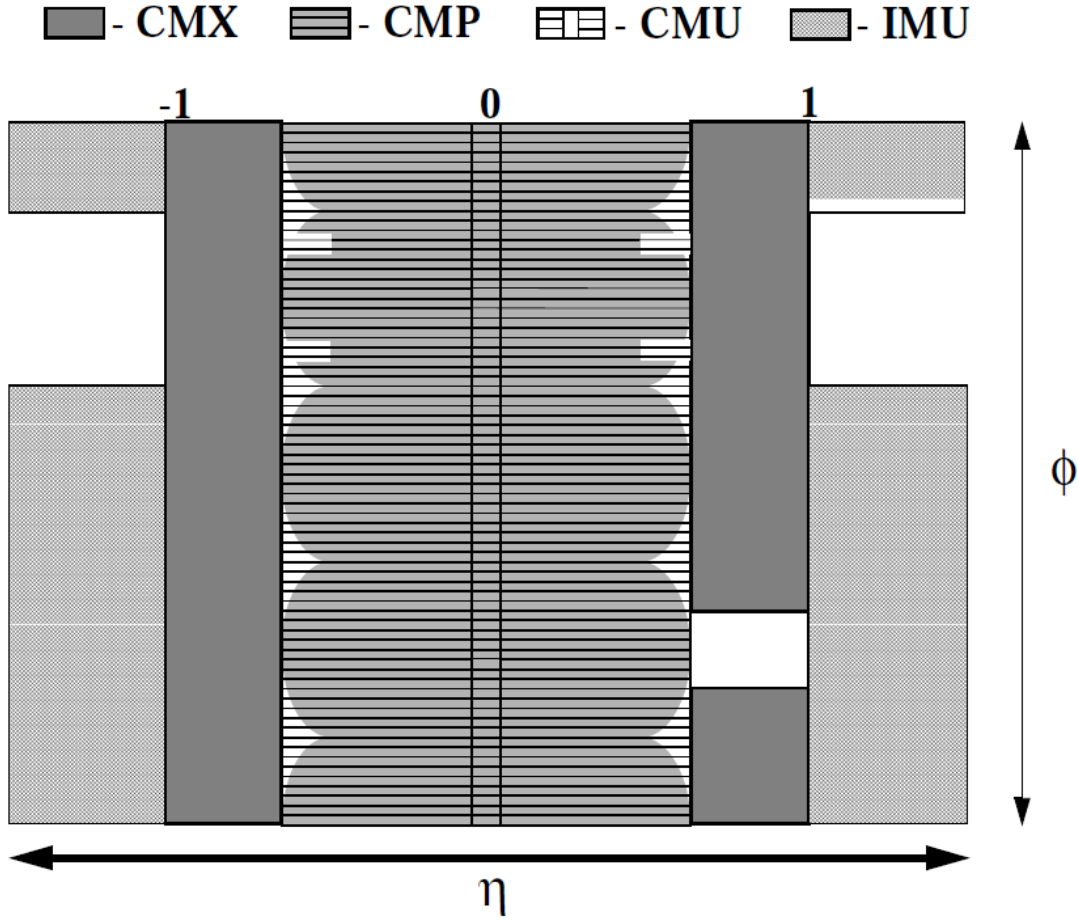


Figure 2.3: η and ϕ coverage of the Run II muon systems

2.5.1 Central Muon Detectors

The first muon system built at CDF, the Central Muon Detector (CMU) [49], is a set of 144 modules, each containing four layers of four rectangular cells. It is placed just outside the central hadronic calorimeter, whose 5.5 interaction lengths absorb more than 99% of the outgoing charged hadrons.

A second set of muon chambers, the Central Muon Upgrade (CMP) [50], forms a square box around the CMU, and is shielded by an additional layer of 60 cm of steel. Due to the detector geometry, the η coverage varies with azimuth as shown in fig. 2.3. The CMP consists of four layers of single-wire drift tubes, staggered by half cell per layer, and operated in proportional mode. On the outer surface of the CMP lies the Central

Scintillator Upgrade(CSP), a layer of rectangular scintillator tiles.

Another upgrade which had begun in Run I is the Central Muon Extension(CMX) with the associated Central Scintillator Extension (CSX). It is a conical array of drift tubes, with scintillators on both sides; it extends the CMU/CMP θ coverage from 55° to 42° , except in a $30^\circ\phi$ gap which is used by the solenoid cryogenic system.

2.5.2 Intermediate Muon Detectors

Detection of muons in the forward region is accomplished by the Intermediate Muon Detectors (IMU). This detector recycles the older Forward Muon toroidal magnets, which is moved closer to the interaction point (just outside the plug calorimeter PMT arrays). The steel toroids, together with a new pair of steel rings, act as shielding for a new array of drift tubes and scintillator counters, placed on the outer radius of the toroids.

Like the CMX/CSX, the IMU has four staggered layers of drift tubes, and two layers of scintillator. Contrarily to the CSX, one of the scintillator layers is separated from the drift tubes by a thick layer of steel; this geometry strongly suppresses fake triggers due to hadrons.

2.6 Data Acquisition and Trigger

Due to the increase in collision frequency, the DAQ (Data Acquisition) and trigger systems of CDF had to be almost completely replaced. The new three-level architecture, schematized in Fig. 2.4, is fully capable of withstanding a 132 ns bunch separation, while keeping dead time as short as possible.

2.6.1 Level 1 Trigger

The front-end electronics of all detectors is fitted with a synchronous pipeline, 42 events deep, where the entire data regarding each event is stored for 5544 ns. Meanwhile, part of the data is examined in a first dedicated, synchronous, highly parallel hardware processors:

- XFT, the extremely Fast Tracker, which reconstructs tracks on the transverse plane of the COT (Central Outer Tracker) to propagate these tracks to the calorimeters and muon chambers;
- the Calorimeter Trigger, which detects electron and photon candidates, jets, total transverse energy, and missing transverse energy;
- the Muon Trigger, which matches XTRP tracks to stubs in the muon chambers.

“Objects” from the level one trigger subsystems are combined in a flexible decision module, which takes a decision by requiring the presence of a certain number of features

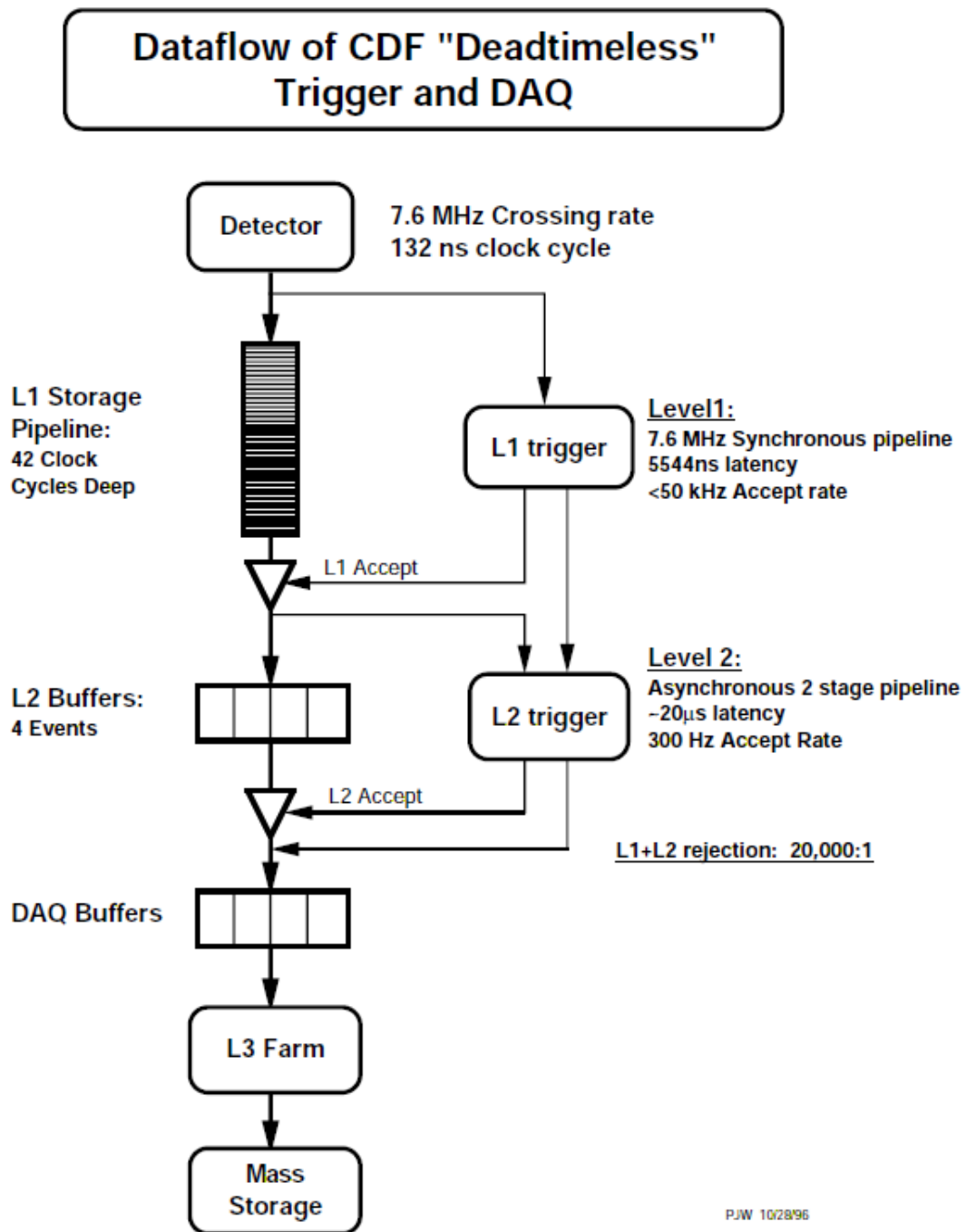


Figure 2.4: Block diagram of the CDF II Trigger

in the event: for example, two muon candidates with P_t above 3 GeV. Up to 64 different sets of requirements can be checked at the same time; each of these triggers can be pre-scaled independently of the others.

The total level 1 trigger takes a decision within $4 \mu s$, while the event's data is still in the pipeline. This makes the first trigger level truly dead-timeless. The rejection factor is about 150 and the event rate is about 50 kHz.

2.6.2 Level 2 Trigger

Events matching the requirements of level 1 are downloaded into one of four asynchronous event buffers, and further analyzed by a second set of hardware processors. Trigger level 2 is asynchronous: events remain in the buffer until they are accepted or rejected. This can cause dead time, when all four buffers are full. In order to keep dead time at 10%, with a level 1 rate of 50 kHz, level 2 has been split in two pipelined steps of $10 \mu s$ each.

- Jets usually affect more than a single calorimetric tower. Calorimeter clustering (L2CAL) sums the energies collected by single towers and provides a measurement of the total jet energy.
- The calorimeter shower maximum (XCES) is used to reduce the rate of fake electrons and photons. It also makes it easier to match XFT tracks to their calorimetric clusters.
- The Silicon Vertex Tracker (SVT) reconstructs tracks in the vertex detector, measuring their impact parameter d . Triggering on d proves extremely helpful in b-quark physics.
- Data is also collected from the level 1 track and muon triggers.

During the second pipelined step, the results of the first phase are fed to a set of Alpha processors; each processor examines the event for a different set of characteristics. The level 2 accept rate is around 300 Hz, with a rejection of about 150.

2.6.3 Level 3 Trigger

After being accepted by the level 2 trigger, the entire event data is read out and loaded into a Linux PC farm, where the event is fully reconstructed in software. The level 3 reconstruction program is almost fully written in C++, using object-oriented techniques.

After an event is reconstructed, it is sent to an event counter, where its characteristics are histogrammed; if the event passes the level 3 cuts, it is also permanently stored to tape.

Assuming a level 3 input rate of 300 Hz, a level 3 rejection of 10, and an average event size of 250 kB.

2.6.4 On-line Monitoring

The CDF detector consists of many detector subsystems and runs in a high rate large bandwidth data transfer environment. To take data with high efficiency and high quality, it is necessary to quickly spot problems with one of these sub-detectors in real time. Multiple event monitor programs are attached to the DAQ system [51, 52, 53]. The on-line monitoring programs are called Consumers, where a consumer is defined as a process which receives events from Consumer Server Logger (CSL) in real time. CSL sends the data to the computer center where they are written to tape and forward copies of a subset of the data to the on-line monitoring programs. Fig. 2.5 shows a schematic view of the CDF on-line monitoring system (Consumer Framework). The task of Consumers is to analyze and monitor the event data and to make histograms and tables. These results could be viewed by the display browser via a server in real time. Results of the monitor are also stored as data files periodically during a run, and also archived systematically. The display browser provides a GUI (Graphical User Interface) to view the on-line monitored results, while also providing some basic utilities to do comparisons with previously stored results. By separating the two tasks of monitoring and displaying, we remove CPU bound associated with displaying graphics from the machine which runs the consumers. During the data taking, multiple consumer processes run in parallel, receiving event data with the desired trigger types from the CSL. Communication between a consumer and run control which control overall CDF DAQ system is handled by the Error Receiver. Severe errors detected by a consumer monitor program are forwarded to run control to take necessary actions. The state manager watches the state of consumers.

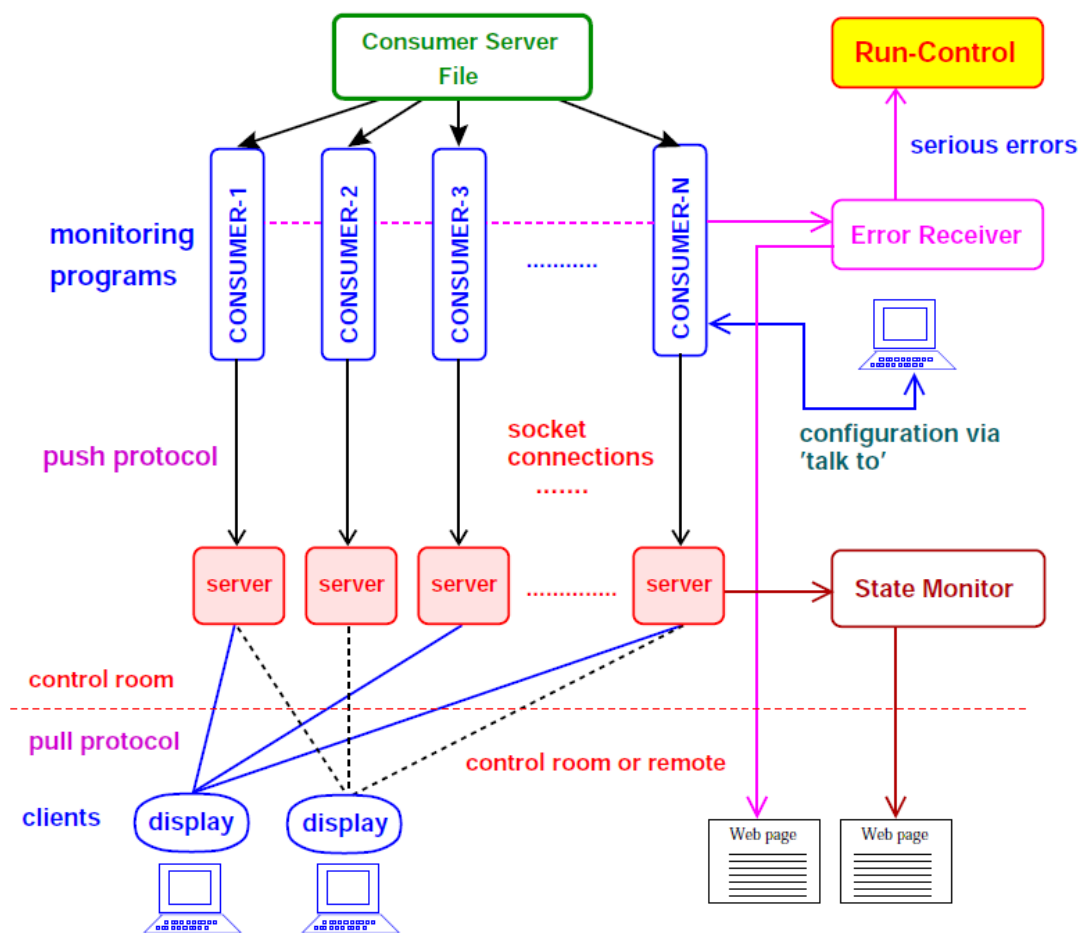


Figure 2.5: Design of the CDF on-line consumer framework

Chapter 3

Reconstruction and Event Selection

This chapter describes how we obtain events that we desire. As we already discussed, the lepton + jets channel is used to reconstruct the top quark mass in this analysis. So we need to look for the events which contain a energetic charged lepton (electron or muon) from the decay of a W boson, four jets originating from four quarks and missing E_T which is regarded as a neutrino from the W boson decay. First we describe how the leptons and jets are identified and then the selection criteria.

Although we desire that the collected data contains signal ($t\bar{t}$) events only, the background events such as W plus jets, single top and QCD events contaminate the data. We also describe the estimation of the numbers of each background events after the event selection.

3.1 Electron Identification

Energetic electrons are identified as electromagnetic showers within the central EM calorimeter corresponding to a high- p_T track. The energy of an electron is measured with calorimeter, and initial momentum direction is determined from the track.

Electron Trigger

Electron events are collected using a central high- E_T electron trigger. Level 1 requires at least 8 GeV in a calorimeter trigger tower with the ratio of hadronic to electromagnetic energy deposited (E_{had}/E_{em}) less than 0.125. It also requires an XFT track pointing to this tower with a p_T of at least 8 GeV/ c . Level 2 forms a calorimeter cluster by adding adjacent towers to the seed tower found with the level 1 trigger. The adjacent towers must have E_T of at least 16 GeV with E_{had}/E_{em} less than 0.125. At this level, the XFT track is confirmed to be pointing to the seed tower. At level 3, an EM cluster is formed and required to have E_T of at least 18 GeV and E_{had}/E_{em} less than 0.125. A fully reconstructed COT track with p_T greater than 9 GeV/ c must point to the cluster within 8 cm in z . Trigger accept rate (bandwidth) were approximately

80 Hz, 8 Hz and 1 Hz for level 1, 2 and 3, respectively. The efficiency of the CEM trigger has been found to be 0.9656 ± 0.0006 .

Electron Cluster Reconstruction

In the central electromagnetic calorimeter (CEM), electrons are reconstructed as an energy cluster of neighboring towers originating from an EM shower. Towers are stored according to E_T and added to a list of possible seeds if their E_T is greater than 2 GeV. The highest E_T tower is the initial seed. Neighboring towers in η are added to the seed if they have energy greater than 100 MeV (sum of electromagnetic and hadronic calorimeter). All cluster towers are in the same wedge (ϕ -segment). A cluster is also formed in the CES detector by adding neighboring channels over a threshold. Fitting this CES cluster with the expected shower profile results in an accurate measurement of the shower position in the calorimeter.

Electron Energy Calibration

Reconstructed electron energy is calibrated to remove instrumental effects and to set the absolute energy scale. Instrumental effects include detector edge effects, light attenuation, and light loss; and are corrected with test beam data. Some detector effects are time dependent and are corrected by averaging over periods of experimental data. The absolute energy scale is set using the $Z \rightarrow e^+e^-$ data; the invariant mass distribution is fit with a Gaussian and tuned to be the world average of $91.18 \text{ GeV}/c^2$ [6].

Electron Identification

An electron is identified if it meets the following requirements: an EM cluster is formed with two adjacent towers in detector η in the offline reconstruction in the CEM region. The cluster E_T must be greater than 20 GeV and the E_{had}/E_{em} less than $0.055 + 0.00045 \cdot E$, where E is the total energy of the EM cluster. Further, the electron must be isolated, such that after removing the candidate cluster towers, the sum of the E_T within an $\eta - \phi$ cone with a radius of 0.4 around the candidates is less than 10% of the E_T of the candidate. A COT track with p_T more than $10 \text{ GeV}/c$ and not consistent with a conversion must point to the most energetic tower. The ratio of the cluster E_T to the track p_T must be less than 2 for clusters with E_T less than 100 GeV. This requirement is not unity to accommodate Bremsstrahlung radiation of the electron. It is removed at high E_T due to imprecision in measuring high p_T tracks. The track is also required to match the position of the EM cluster according to the cluster formed from CES wire hits. The requirements are $-3\text{cm} < q\Delta x < 1.5\text{cm}$ and $|\Delta z| < 3\text{cm}$, where $\Delta x \equiv r\Delta\phi$ and q is the charge in units of e . The $q\Delta x$ requirement is asymmetric to account for Bremsstrahlung radiation.

3.2 Muon Identification

Muons have a larger mass than electrons and at high momentum are nearly minimum ionizing particles. They pass through the calorimeters without showering and are detected with drift chambers placed on the outside region of the detector. A muon is identified as a high momentum track corresponding to hits in the drift chambers and energy consistent with a minimum ionizing particle in the calorimeters. The track provides the measurement of muon momenta and energy.

Muon Trigger

Muon events are collected with three triggers CMU, CMP and CMX. The CMU and CMP triggers are merged into a single CMUP trigger. The CMUP trigger covers detector $|\eta| < 0.6$ and the CMX trigger covers $0.6 < |\eta| < 1.0$. At level 1, there must be hits in one or more layers consistent with a charged particle within the CMU or CMX detectors. Additionally, for the CMUP trigger, there must be 3-4 hits in CMP consistent with those in the CMU. Also required is a XFT track matching in the $r - \phi$ plane of the hits with a p_T of at least 4 GeV/ c for CMUP and 8 GeV/ c for CMX. Level 2 increases the p_T requirement of the XFT track to 15 GeV/ c for both CMUP and CMX triggers. At level 3, muon stubs and COT tracks have been reconstructed, and a COT track with p_T of at least 18 GeV/ c is required to match the muon stub in the $r - \phi$ plane within 10 cm in the CMU and 20 cm in the CMP or within 10 cm of the CMX.

Trigger accept rates (bandwidth) for CMUP were approximately 90 Hz, 9 Hz and 0.4 Hz for levels 1, 2 and 3, respectively. Those for the CMX trigger were approximately 9 Hz, 7 Hz and 0.25 Hz. The efficiency of the CMUP trigger was found to be 0.887 ± 0.007 and that of CMX to be 0.954 ± 0.006 .

Muon Stub Reconstruction

Muons are reconstructed in the CMU, CMP and CMX muon detectors as stubs, or a set of hits consistent with particle trajectory. This requires hits in 3 to 4 out of the 4 layers of the muon chambers. The hits are fit to a straight line, from which a position and direction can be determined.

Muon Momentum Calibration

Since particle four momentum is measured from the track associated with the muon, the relevant calibrations are applied to tracks, specifically curvature corrections affecting the p_T measurement. Calibrations also include the relative alignment within and between the silicon and COT tracking systems. The absolute energy scale is set using $Z \rightarrow \mu^+ \mu^-$ experimental data: The invariant mass distribution is fit with a Gaussian and tuned to be the world average of 91.18 GeV/ c^2

Muon Identification

A muon is identified if it meets the following requirements: stubs are formed from hits in the CMU, CMP and CMX detectors with the offline reconstruction. The position of these stubs in $r - \phi$ space must match a COT track with p_T greater than 20 GeV/ c extrapolated to the position of the stub within 3 cm for the CMU, 5 cm for the CMP and 6 cm for the CMX. Note that these sizes are mostly determined by the effects of multiple scattering rather than detector position resolution. Further, calorimeter energy in towers corresponding to the extrapolated track trajectory must be consistent with that of minimum ionizing particles - a maximum energy on the order of a few GeV depending on track p_T . Muons also have isolation requirements where the sum of the E_T deposited in the calorimeters within an $\eta - \phi$ cone with a radius of 0.4 must be less than 10% of the p_T of the muon candidate.

3.3 Jet Reconstruction

Quark and gluon fragmentation and radiation create showers of particles in the detector known as jets. Jets deposit energy in the broad region of the electromagnetic and hadronic calorimeters. Reconstructed jets are clustered energy depositions and generally provide much less precise energy measurements of the originating quark or gluon than reconstructed charged leptons. The large multiplicity of possible hadronization and their non-perturbative nature make it impossible to exactly reconstruct the originating quark or gluon from a jet. Energy calibrations are performed by obtaining the average of the energy ratio of measured to the original parton and introduce significant uncertainty in analyses.

Jet Reconstruction

Jets are reconstructed as energy depositions in calorimeter towers. Towers are clustered using the JETCLU algorithm, and are included if they have $E_T > 1$ GeV, and do not correspond to an electron. The jets used in this analysis have been reconstructed after the final selection of the lepton in the event, and are clustered accordingly. Towers are merged if they are in an $\eta - \phi$ cone with a radius of 0.4 to form a proto-jet described by

$$E_T^{jet} = \sum_{i=0}^{N_{tow}} E_{T_i} \quad (3.1)$$

$$\phi^{jet} = \sum_{i=0}^{N_{tow}} \frac{E_{T_i} \phi_i}{E_T^{jet}} \quad (3.2)$$

$$\eta^{jet} = \sum_{i=0}^{N_{tow}} \frac{E_{T_i} \eta_i}{E_T^{jet}} \quad (3.3)$$

Note there is appropriate handling of the 2π boundary in ϕ . This process is run iteratively, dropping and adding towers, and the variables recalculated until the cluster centroid does not change. After reaching this stable point, jets overlapping by more than 50% in $\eta - \phi$ space are merged. If overlap is less than this amount, then towers are assigned to the closest other jet. E_T , ϕ and η of the jet are calculated by summing the information from the towers as shown in Equations (3.1)-(3.3).

Jet Energy Corrections

Compared to electrons and muons, jets are very complicated objects. Various instrumental, algorithm and physics effects combine to make the jet energy measurement uncertain. Corrections to jet energies are derived from studies using both experimental and simulated data.

The hadronic and electromagnetic calorimeters are equilibrated before forming jets or determining any corrections. Electromagnetic calorimeters are calibrated using electrons as described in section 3.1. Hadronic calibrations are initially set using a test beam of 50 GeV/ c charged pions. The CHA and WHA calorimeters are further calibrated with a laser system, a Cs^{137} radioactive source system, muons from events containing $J/\psi \rightarrow \mu^+ \mu^-$, and minimum bias experimental data. The PEM and PHA calorimeters are calibrated with a laser system and a Co^{60} radioactive source system. The energy loss from muons coming from $W \rightarrow \mu\nu$ events are used to verify the stability of the calibrations over time.

Jet energy corrections are derived and applied in six separate levels as shown in Table 3.1: relative, multiple interactions, absolute, underlying event, and out of cone. These corrections are applied in the order. After absolute corrections, jets should be independent from instrumental effects.

Level	Contents
1	Relative corrections
2	Not in use
3	Not in use
4	Multiple Interactions
5	Absolute
6	Underlying event
7	Out-of-cone
8	Splash-out(uncertainty only)

Table 3.1: The jet energy correction levels.

Relative corrections equilibrate the response of the calorimeter as a function of detector η . This dependence arises because of the physical separation of the two central calorimeter components at $\eta = 0$, the separation of the central and plug calorimeters at $\eta = 1.1$, and the non-uniform response between central and plug calorimeters.

Corrections are derived from balancing the p_T between a trigger jet and a probe jet in events with two jets and no additional hard QCD radiation.

Since we are dealing with $p\bar{p}$ collisions, more than one inelastic collision is possible

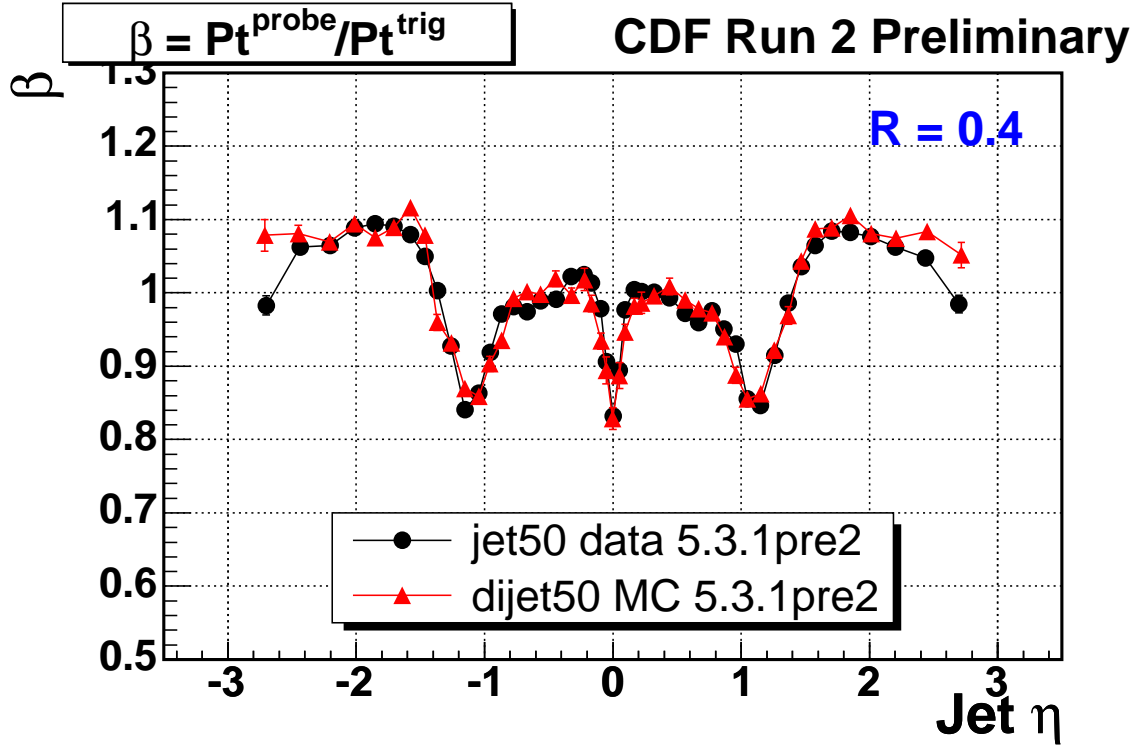


Figure 3.1: Example of dijet balancing in relative jet energy corrections as a function of jet detector η .

in a given bunch crossing. This is known as multiple interactions. It is unlikely to have two hard scattering processes in a single crossing, but the energy from the second scattering contributes to the energy deposited in the calorimeters and therefore in the jet cone. To keep from biasing the measurement, the average energy from secondary collisions is subtracted from the hard scattering process. This amount depends on the instantaneous luminosity and therefore the number of reconstructed vertices. On average, the correction is 0.36 GeV per jet per additional interaction, or 1% of the energy of the average jet. This correction is derived from minimum bias experimental data by studying the average transverse energy deposited in a jet cone as a function of the number of reconstructed vertices.

The absolute energy correction attempts to map the energy measured in the calorimeter back to that of the particles creating the jet. For this reason, corrections are independent of the CDF detector to the first order after this point. Note that this correction does depend on the parton causing the shower: quark showers are different from gluon showers. Since there is no way to a priori determine if the shower was caused by a

quark or a gluon, the effects are averaged. This correction also averages the effects of parton species and momentum inside of a jet. Electromagnetic particles have a linear calorimeter response, while charged hadronic particles have a non-linear response depending on p_T . This correction is derived using simulated data with two jets in an event by comparing the p_T of particle jets and reconstructed jets, and depends on the accuracy of the modeling of the transformation of particle jets into reconstructed jets.

The final three corrections, underlying event, out of cone and splash out, are not used in this analysis because they depend on the underlying hard scattering process. They are intended to finish mapping jet energy to parton level. Rather than using a generic correction averaging over all possible data, we use a mapping specific to $t\bar{t}$ production. Described here for completeness, the underlying event correction averages out effects from initial state radiation and/or spectator partons with color connection to the other partons of the proton. The out-of-cone correction averages the effects of final state radiation at large angles, particles exiting the cone due to fragmentation, and low p_T particles. Splash-out is used in only systematic uncertainty estimation. As with the absolute energy corrections, these corrections are determined using simulated data events with two jets. They are solely determined from simulation at particle generator level and not dependent on the CDF detector.

In order to validate the jet energy scale determination, several consistency checks are done. The jet energy corrections, which are mostly derived from dijet samples, are applied to γ -jet and Z -jet events to verify the validity of the corrections and systematic uncertainties. The γ -jet data sample is ideal for studying the jet energy scale. The photon energy p_T^γ is measured accurately in the CEM calorimeter and thus provides a perfect reference for the jet energy. At tree-level the jet energy should always balance the photon energy: $p_T^{jet}/p_T^\gamma = 1$. Another excellent calibration sample are $Z \rightarrow l^+l^-$ events where the p_T of the Z boson provides a reference scale for the jet. The advantage compared to the γ -jet samples is that it is nearly free from background contamination, at the expense of smaller statistics. With the both validation using γ -jet and Z -jet valance, it is verified that the jet energy scale is well determined.

In the process of determining corrections to the jet energy scale, we estimates the uncertainty for each correction. Figure 3.2 shows these uncertainties as a function of jet p_T . Uncertainties on corrections to the jet energy scale are a source of systematic uncertainty in the top quark mass measurements. This analysis measures the jet energy scale. The uncertainty from this measurement is a statistical uncertainty which represents most of the systematic uncertainty due to the jet energy scale uncertainty. [62]

Secondary Vertex Tagging of Jets (b-tags)

Hadrons containing b quarks are unusual in that they have long lifetimes and will travel a significant distance from that interaction point before decaying, creating a secondary vertex. Those from top quark decay are highly boosted and will travel a few millimeters from the interaction point. These secondary vertices are identified in jets with E_T greater than 15 GeV. All SVX tracks with $p_T > 0.5$ GeV/c within an

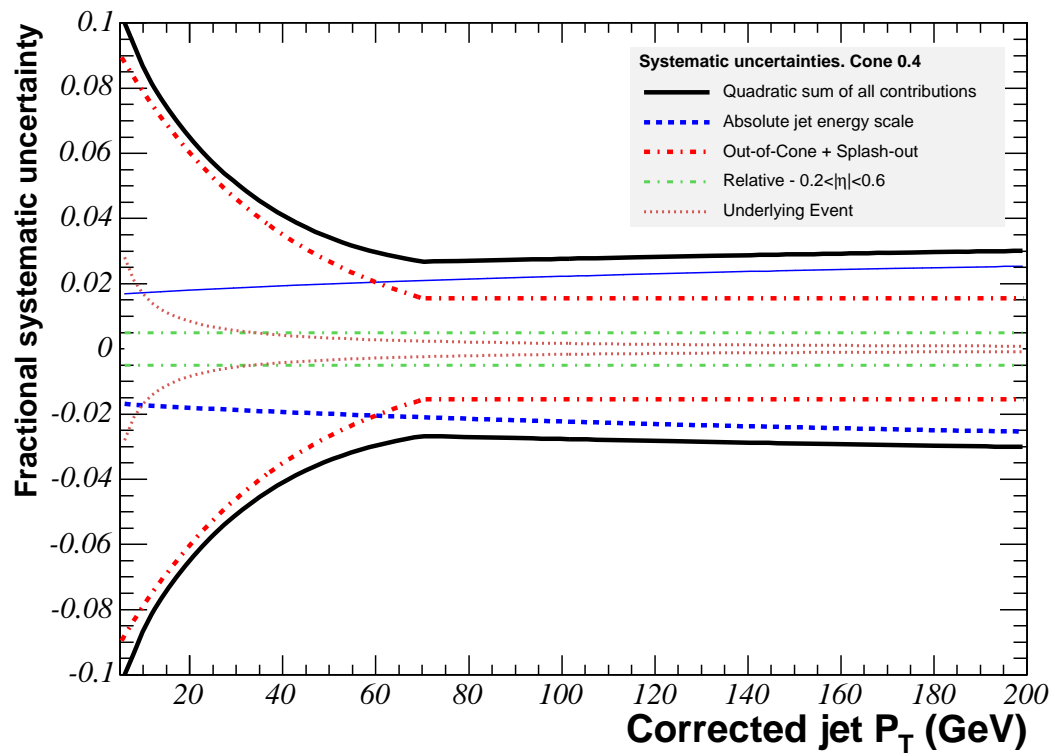


Figure 3.2: Relative contributions to uncertainty on jet energy scale corrections.

$\eta - \phi$ cone of radius 0.4 around the jet center are considered for vertex determination. A secondary vertex is formed by the “SecVtx” algorithm. Firstly, we arrange the tracks in the jet in order according to p_T and quality and then determine the two best tracks which form a vertex. Also another track is required. This third track must be associated with the vertex which is formed by the former two tracks. If a third track is not found, the next two best tracks are selected and continues until no tracks are left. If the three tracks which forms the vertex are not found, two tighter tracks ($p_T > 1.0$ GeV/ c and $|d_0/\sigma_{d_0}| > 2.0$ where d_0 is impact parameter) are required. Vertices consistent with long-lived neutral particles (K_s^0 and Λ) are removed. If the distance in $r - \phi$ space between primary and secondary vertices (L_{xy}) is greater than 7.5 times its uncertainty ($\sigma_{L_{xy}}$), the secondary vertex is considered tagged. This is considered as positive identification of a jet originating from a b quark, a “b-tag”. Figure 3.3 shows the efficiency to tag jets in top quark Monte Carlo samples which have been matched to b quarks and Figure 3.4 shows the false tag rate using inclusive jet data. ‘Tight SecVtx’ is used in this analysis and ‘Loose SecVtx’, which is required looser cut than tight tag such as $L_{xy}/\sigma_{L_{xy}} > 6.0$, is not used in this analysis.

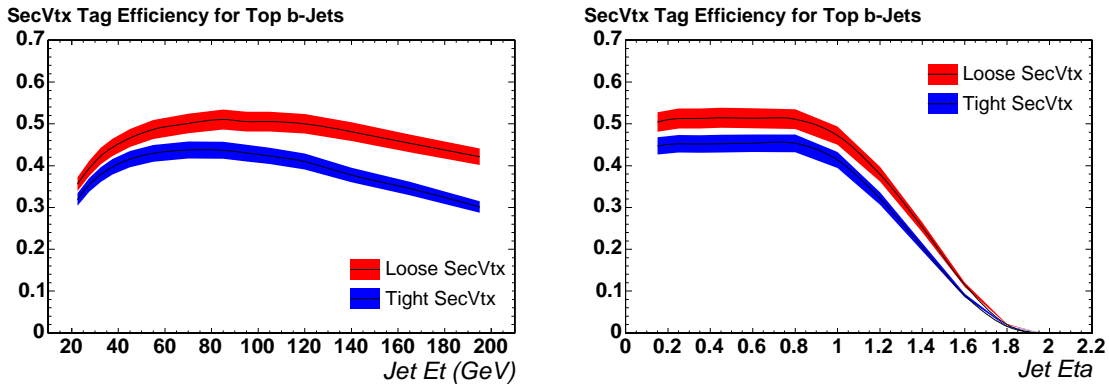


Figure 3.3: The plots show the tagging efficiency with top quark Monte Carlo samples

3.4 Missing Transverse Energy

Since the CDF detector is essentially in the center of mass frame of the $p\bar{p}$ collisions, we expect the energy deposited in the detector to balance in the transverse plane, satisfying energy conservation. Energy in the z-dimension is difficult to measure because of loss of particles in the beam pipe. The extent to which the energy is unbalanced is known as the missing transverse energy (\cancel{E}_T). Neutrinos escape the detector without detection and are often indicated by a significant amount of \cancel{E}_T . Missing transverse energy is defined as the magnitude of the vector formed by the negative sum over calorimeter

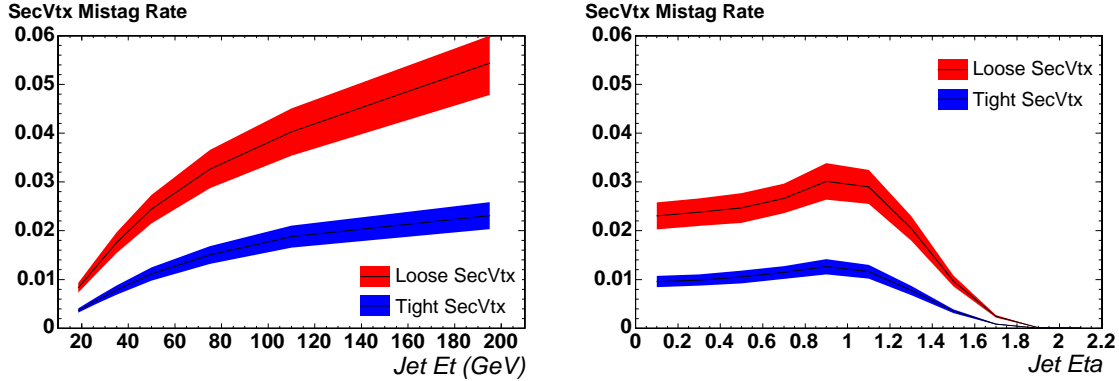


Figure 3.4: The plots show the false b-tag rate with inclusive jet data.

towers with $|\eta| < 3.6$:

$$\cancel{E}_T = - \sum_i E_T^i \hat{n}_i \quad (3.4)$$

where \hat{n}_i is a unit vector perpendicular to the beam axis pointing at tower i . The corrected for jets with detector $|\eta| < 2.4$ and energy greater than 8 GeV after multiple interaction correction. In muon events, the \vec{p}_T of the track associated with the muon is also included in the sum.

3.5 Event Selection and Collected Data

We look for in the $t\bar{t}$ production $lepton + jets$ channel which contains a high p_T lepton (electron or muon), missing transverse energy which is considered as neutrino from a W decay, and four jets in which two jets are expected from b quarks and other two jets are from a W boson decay.

A high p_T lepton is required to be isolated, and to have E_T greater than 20 GeV and $|\eta| < 1.0$, which is called 'tight lepton'. The event that has more than one tight lepton is removed. Missing transverse energy \cancel{E}_T is required to be greater than 20 GeV. Events with Z bosons candidates are removed by requiring that there is no second object which forms an invariant mass with the primary lepton within the window of $76 < M < 106$ GeV/ c^2 . In the case of an electron event, the second object is either an isolated electromagnetic object (for instance another electron), a jet with $E_{had}/E_{em} < 0.05$, or an oppositely signed single track. In the case of a muon event, the second object is either another isolated muon or an oppositely signed track. A cosmic ray veto removes virtually all cosmic muons from events by comparing timing information in the COT to the beam crossing and by identifying tracks consistent with particles entering and exiting the detector. Electrons from photon conversions are removed by searching for tracks with opposite curvature that extrapolate to an origin within 0.2 cm in the $r - \phi$ plane and a difference in angle less than 0.04 radians at the

closest approach. The primary z vertex of the event must be within 60 cm from the center of the CDF detector. Events must have exactly four jets which has $E_T > 20$ GeV and $|\eta| < 2.0$, and then we require at least one tagged jet as a b-jet with the Secondary Vertex Tagging algorithm. Table 3.2 shows the summary of event selection criteria.

The data we use in this analysis were collected during the period March 2002 - March 2007. The total integrated luminosity for this period is 1.7 fb^{-1} with good silicon tracking. Finally the number of observed events with this selection criteria are 343 events.

Object	Requirement
A tight lepton	$E_T > 20 \text{ GeV}, \eta < 1.0$
Missing E_T	$\cancel{E}_T > 20 \text{ GeV}$
Z veto	$M_{ll} < 76 \text{ GeV}/c^2$ and $M_{ll} > 106 \text{ GeV}/c^2$
Cosmic ray veto	Timing information
Conversion veto	$\Delta R < 0.2 \text{ cm}$ and $\theta < 0.04$
Z vertex	$< 60 \text{ cm}$
Four tight jets	$E_T > 20 \text{ GeV}$ and $ \eta < 1.0$
At least one b-tagged jet	SecVTX b-tagging algorithm

Table 3.2: The summary of event selection criteria.

3.6 Background Composition

Background composition for *lepton + jets* channel in real data is estimated as follows. We employ a combination of data and MC-driven approaches.

Background sources are diboson production such as WW , WZ and ZZ , and single top production, QCD production which does not contain W , and W +jets production.

Diboson and single top

These processes have well-defined theoretical cross sections, and are analogous to the $t\bar{t}$ acceptance, so the contributions from these processes are derived from Monte Carlo samples. These contribution before applying b-tagging is basically estimated by applying $N_{pre} = \mathcal{L}^{tot} A_{t\bar{t}} \sigma$ where N_{ev} is the expected number of events, \mathcal{L}^{tot} is a total integrated luminosity of 1.7 fb^{-1} , $A_{t\bar{t}}$ is a acceptance of event selection to the Monte Carlo samples, and σ is the production cross section. Then b-tagging efficiency is applied to N_{pre} to obtain the expected number of these background. The b-tagging efficiency is estimated by Monte Carlo. However it is needed to be corrected by the difference between Monte Carlo and real data. This b-tagging scale factor is the measured ratio fo single jet and single b-tagging efficiencies in a low- E_T sample.

QCD

The electron conversion, b -semileptonic decays and jet fake electron could be considered as QCD(Non-W) background. This background is estimated using the anti-electron real data sample. We make the missing E_T distribution for the W +jets, $t\bar{t}$ Monte Carlo sample, which is generated with top quark mass of $175 \text{ GeV}/c^2$ at 6.7 pb, and the anti-electron data sample as follows. The anti-electron is defined as an electron which fails at least two of all tight lepton selection requirements. We fit the missing E_T distribution in the range between 0 and 120 GeV to a sum of the W +jets Monte Carlo template and the anti-electron template, while $t\bar{t}$ Monte Carlo is fixed. We take the integral of the anti-electron shape divided by the integral of the W +jets and $t\bar{t}$ shape over the missing E_T larger than 20 GeV as the QCD fraction F_{QCD} . The number of QCD background is obtained by multiplying F_{QCD} to observed data.

W +light flavor

The W +light flavor contribution is estimated using mistag rate. The mistag matrices give a b -tagging ratio for each jet, which parametrizes the generic jet negative tag rate in terms of the jet energy, η , N_{tracks} , number of Z vertices, primary vertex position, and the sum of the transverse energy. Since the mistag rate is obtained using only the negative tag rate in the generic jet samples, further corrections are needed to account for the facts that there are real heavy flavor jets in the generic samples the increase the tag rates, the negative tag rate is smaller than the positive rate even for light tags due to long lived light-flavor (K_S and Λ), and tags due to material interactions. The mistag asymmetries correct these effects. Then the contribution from this source is calculated as $N_{events} = \sum_{events} \sum_{jets} P_{jet}^{mistag}$ where P_{jet}^{mistag} is the mistag rate corrected for mistag asymmetry and N_{event} is the number of events.

W +heavy flavor

The W +heavy flavor contribution is not known a priori, therefore we take the overall normalization from the data sample before applying SecVTX b -tagging. We subtract the QCD and those with non-QCD jet production ($t\bar{t}$, dibosons and single top) from the events, and assume the remainder is W +jets, and then heavy flavor fraction and b -tagging efficiencies are applied to each sources.

$$N_{pre}^W = N_{pre}^{data} (1 - F_{QCD}) - N_{pre}^{t\bar{t}} - N_{pre}^{diboson} - N_{pre}^{singletop} \quad (3.5)$$

$$N_{tag}^W = N_{pre}^W \sum_i \epsilon_i F_i^{hf} \quad (3.6)$$

where F_{QCD} is the QCD fraction in real data, $N_{pre}^{t\bar{t}}$, $N_{pre}^{diboson}$ and $N_{pre}^{singletop}$ are the expected numbers before applying the SecVTX b -tagging for the $t\bar{t}$, diboson and single top events, respectively. ϵ_i is b -tagging efficiency and F_i^{hf} is the heavy flavor fraction in W +jets events, and the sum is over different heavy flavor configurations or $i = Wb\bar{b}$, $Wc\bar{c}$, and Wc .

The $t\bar{t}$ contribution before SecVTX b-tagging is basically estimated by applying $N_{t\bar{t}}^{pre} = \mathcal{L}^{tot} A_{t\bar{t}}^{pre} \sigma_{t\bar{t}}$ where \mathcal{L}^{tot} is a total integrated luminosity of 1.7 fb^{-1} , $A_{t\bar{t}}^{pre}$ is a selection acceptance before applying SecVTX b-tagging to the Monte Carlo samples generated with a top mass of $175 \text{ GeV}/c^2$, and $\sigma_{t\bar{t}}$ is the $t\bar{t}$ production cross section fixed to 6.7 pb .

In order to evaluate the heavy flavor fraction in W +jets events, the fraction containing real bottom and charm jets. We assume that the fractions are more stable at higher order than the absolute cross section. These quantities are measured at leading order in a Monte Carlo sample, which specifically takes into account $Wb\bar{b}$, $Wc\bar{c}$, and Wc processes, and the overall scale for $b\bar{b}$ and $c\bar{c}$ is calibrated using generic jets data sample. This scale, called K, is primarily intended to cover a mis-estimate of $g \rightarrow b\bar{b}$ and $g \rightarrow c\bar{c}$, processes which contribute largely to the heavy flavor content of both W +jets and generic QCD.

ϵ_i 's are basically estimated using Monte Carlo samples. In order to correct the difference between Monte Carlo and Data, we introduce b -tagging scale factor. This scale factor is measured in both the 8-GeV electron and 8-GeV muon samples. The first method uses electrons with and without conversion partners as corresponding light and heavy flavor samples and measures the tag rate differences to extract the efficiency, and compares it with the efficiency in simulation. The second determines the b content of the sample by performing p_T^{rel} fits (μ p_T relative to the jet axis) and extracts the absolute tag rate in those events. The results are combined into a single value to be applied in all tagging analysis. Thus the b -tagging scale factor is estimated to be 0.95 ± 0.05 and tagging efficiency ϵ 's corrected for b -tagging scale factor are $40 \pm 2\%$ for b jets and $8 \pm 1\%$ for c jets.

Background Summary

Table 3.3 shows the final number of expected events for each background source.

Source	Number
Diboson	3.19 ± 0.32
Single top	3.61 ± 0.34
$Wb\bar{b}$	14.37 ± 5.82
$Wc\bar{c}/Wc$	11.41 ± 4.66
W+LF	14.57 ± 3.29
Non-W	12.48 ± 10.97
Signal	232.29 ± 32.15
Total	293.69 ± 35.95

Table 3.3: The number of expected events for individual background source.

3.7 Monte Carlo Simulations

Monte Carlo simulations are used for a lot of purpose in this analysis: to correct jet energy specifically for this analysis, to validate this method, to estimate the effect from the backgrounds and to estimate the systematic uncertainties.

The simulation of $t\bar{t}$ events relies mainly on the HERWIG [55] and PYTHIA [54] Monte Carlo program which employ the leading order QCD matrix elements for the hard process, followed by parton showering to simulate the gluon radiation and the fragmentation. The CTEQ5L [56] parton distribution function was used heavy flavor jets, with b and c hadrons, use the decay algorithm QQ [58]. The dominant background, W+jets events, are generated with ALPGEN [57], a leading-order matrix element generator capable of final states with a large number of jets.

The CDF II detector simulation reproduces the response of the detector to particles produced in $p\bar{p}$ collisions. Tracking of particles through matter is performed with GEANT3 [59]. Charge deposition in the silicon detectors is calculated using a sample geometrical model based on the path length of the ionizing particle and an unrestricted Landau distribution. The drift model for the COT uses the GARFIELD package [60], with the default parameters tuned to match COT data. The calorimeter simulation uses the GFLASH [61] parameterization package interfaced with GEANT3. The GFLASH parameters are tuned using test beam data for electrons and high p_T pions, and they are checked by comparing the calorimeter energy of isolated tracks in the collision data to their momenta as measured in the COT.

Chapter 4

Top Quark Mass Measurement

This chapter describes how we reconstruct the top quark mass with selected data as discussed in chapter 3. To reconstruct the top quark mass, we use dynamical likelihood method (DLM). This method is based on maximum likelihood method. The likelihood is defined by differential cross section and a transfer function(TF). The likelihood is a function of a pole mass of top quark and jet energy scale(JES) so that we can measure not only the top quark mass but also jet energy scale. By measuring the jet energy scale, the uncertainty of jet energy scale can be reduced.

We also describe the performance of our method with Monte Carlo simulations for variety of input top quark mass and jet energy scale, wrong jet-parton assignments and background effects.

Finally, the result with $1.7fb^{-1}$ is revealed.

4.1 Dynamical Likelihood Method

Differential cross section for the final parton state

Parton level process, i.e. hard scattering process, in $p\bar{p}$ collision can be generally written as,

$$a/A + b/B \rightarrow \dots \rightarrow C \quad (4.1)$$

$$C \equiv \sum_{i=1}^n c_i \quad (4.2)$$

where a and b are the initial partons, each representing a quark or an anti-quark or a gluon, in hadrons A(=proton) and B(=anti-proton), respectively, and c_1, c_2, \dots, c_n are final state partons. States of partons are after the initial and before the final-state radiation. In case of the lepton+jets channel for $t\bar{t}$ production, initial parton set (a, b) is (q, \bar{q}) , (\bar{q}, q) , (g, g) , and the final partons are $e/\mu, \nu$, and b and light quarks. Symbol c_i stands for 4-momentum, and \mathbf{p} its 3-momentum.

In general, hadronic cross-section for n-body final state partons is given by

$$d\sigma = dz_1 dz_2 d^2\mathbf{p}_T f_{a/A}(z_1) f_{b/B}(z_2) f_T(p_T) d\hat{\sigma}(a + b \rightarrow C; \boldsymbol{\alpha}) \quad (4.3)$$

where $d\hat{\sigma}$ is the parton level cross section,

$$d\hat{\sigma}(a + b \rightarrow C; \boldsymbol{\alpha}) = \frac{(2\pi)^4 \delta^4(a + b - C)}{4\sqrt{(a \cdot b)^2 - m_a^2 m_b^2}} |\mathcal{M}(a + b \rightarrow C; \boldsymbol{\alpha})|^2 d\Phi_n(a + b; C) \quad (4.4)$$

In eq.(4.3) symbol $\boldsymbol{\alpha}$ represents a set of dynamical constants, e.g. masses, decay widths and coupling constant ratios. In the present analysis, $\boldsymbol{\alpha}$ is simply the top quark mass M_{top} . Variables z_1 and z_2 are energy fraction of a and b in hadrons A and B respectively, and \mathbf{p}_T is the total momentum of the initial/final system in the plane transverse to the beam axis. Functions $f_{a/A}(z_1)$ and $f_{b/B}(z_2)$ denote Parton Distribution Functions(PDFs), while f_T is the probability density function for the total transverse momentum p_T of the system acquired by the initial state radiation. In eq.(4.4), \mathcal{M} is the matrix element of the process which is being looked at(in our case, $t\bar{t}$ process), and $d\Phi_n$ is the Lorentz invariant phase space factor,

$$d\Phi_n^{(f)} = \prod_{i=1}^n \frac{d^3 \mathbf{c}_i}{(2\pi)^3 2c_i^0} \quad (4.5)$$

Integration eq.(4.3) combined with eq.(4.4), one gets

$$d\sigma = I(a, b) |\mathcal{M}(a + b \rightarrow C; \boldsymbol{\alpha})|^2 d\Phi_n^{(f)} \quad (4.6)$$

where

$$I(a, b) = \frac{(2\pi)^4}{4|\mathbf{A}||\mathbf{B}|\sqrt{(a \cdot b)^2 - m_a^2 m_b^2}} f_{a/A}(z_a) f_{b/B}(z_b) f_T(p_T) \quad (4.7)$$

is the integration factor for the initial state. If one assumes final partons occupy a unit phase volume in a single scattering process, $d\sigma/d\Phi_n$ gives the total probability for the final quantum state specified by $c(c_1, \dots, c_n)$.

Differential cross section for primary partons

Resonances, primary and secondary partons DLM is a procedure to reconstruct (infer) the parton states, i.e. a set of momenta of partons which appear in the Feynman graph process (4.1). We call intermediate partons (internal lines) ‘resonances’. The number of partons in process (4.1), excluding a and b , is generally greater than that of final partons n . In the reconstruction, if one infers momenta of n partons, the momenta of other partons are determined by the energy-momentum conservation at vertices. We call n inferred partons ‘primary’, and others ‘secondary’ partons. Specifically, if resonance r decays into m daughters $d^{(r)}(d_1^{(r)}, \dots, d_m^{(r)})$, the invariant mass squared of the resonance should satisfy

$$s_r = \left(\sum_{l=1}^m d_l^{(r)} \right)^2. \quad (4.8)$$

If all daughters of r are primary partons, eq.(4.8) gives s_r , while if resonance r is a primary parton, eq.(4.8) gives a constraint to daughter momenta. The choice of the

primary parton set is optional, depending on the process and the reconstruction algorithm.

Propagator factor of a resonance When one uses theoretical formulate for the production and decay matrix elements of a resonance, \mathcal{M}_{prod} and \mathcal{M}_{decay} , then the matrix element squared associated with the resonance can be written as

$$|\mathcal{M}^{(r)}|^2 = |\mathcal{M}_{prod}^{(r)}|^2 \Pi(s_r) |\mathcal{M}_{dec}^{(r)}|^2, \quad (4.9)$$

where $\Pi(s_r)$ is the propagator factor. In general, we take the Breit-Wigner form of propagator factor,

$$\Pi(s_r) = \frac{1}{(s_r - M_r^2)^2 - \Gamma_r^2 M_r^2} \quad (4.10)$$

as an approximation. More discussions on the propagator factor will be given in the next subsection.

Phase volume $d\Phi_n^{(*)}$ for primary partons If resonances are taken as primary partons, their phase space factors are to be taken into account. This is because the parton states should be inferred uniformly with respect to their phase volume. If we denote the n-body phase volume of primary partons by $d\Phi_n^{(*)}$, it is shown by using the recursion formula of the phase space that

$$\frac{d\sigma}{d\Phi_n^{(*)}} = F_r \frac{d\sigma}{d\Phi_n^{(f)}} \quad (4.11)$$

In eq.(4.11), F_r is called 'resonance' factor. If resonance (r_1, \dots, r_h) are taken as primary partons, the resonance factor is given by

$$F_r = \begin{cases} \prod_{i=1}^h \frac{E(r_i)}{E(d_0^{(r)})} & \text{for } h \geq 1, \\ 1 & \text{for } h = 0, \end{cases} \quad (4.12)$$

where $\bar{E}(d_0^{(r)})$ stands for the energy of the daughter parton whose momentum is determined from eq.(4.8).

Transfer Function

Final partons are not directly observed: they undergo parton evolution plus hadronization and are observed by detectors with finite resolutions. In the data analysis, quarks and gluons are reconstructed as jets. To describe the correlation between the final parton state and observed quantities(observables), we introduce the transfer function(TF) $w(\mathbf{x}|\mathbf{y}||\boldsymbol{\alpha})d\mathbf{x}d\mathbf{y}$, where \mathbf{y} represents a set of observables and \mathbf{x} is a parton variable set which corresponds to \mathbf{y} . The TF is the probability density function for \mathbf{x} and \mathbf{y} , namely

$$dP(\mathbf{x}, \mathbf{y}) = w(\mathbf{x}|\mathbf{y}||\boldsymbol{\alpha})d\mathbf{x}d\mathbf{y} \quad (4.13)$$

The selection of variables as \mathbf{y} is optional, e.g. if daughters of a resonance are all observable, one may choose the observed invariant mass (or its squared) of the daughters as one of \mathbf{y} . In the analysis of this paper for *lepton + jets* process, \mathbf{y} consists of

momenta of e and μ and 4 jets, and the missing E_T

Quantization of transfer variable space

- Jacobian scaled transfer variables

Let us call \mathbf{x} and \mathbf{y} ‘transfer variables’, and consider how the condition $\Delta\Phi_n^{(i)} = 1$ characterize the variable spaces. This condition applies only to the primary partons, and the transfer variables only make sense for observable partons. We denote transfer variables of the i -th observable primary partons by \mathbf{x}_i and the corresponding observables by \mathbf{y}_i where $i = 1, \dots, N_{obs}^*$. Variable \mathbf{x}_i is a 3-component function of \mathbf{p}_i , and generally $N_{obs}^* \leq n$.

For the i -th observable primary parton, we introduce Jacobian-scaled variables by

$$d\mathbf{X}_i = \frac{d\Phi_1^i}{d\mathbf{x}_i} d\mathbf{x}_i \equiv J_{x_i} d\mathbf{x}_i \quad (4.14)$$

$$d\mathbf{Y}_i = \frac{d\Phi_1^i}{d\mathbf{y}_i} d\mathbf{y}_i \equiv J_{y_i} d\mathbf{y}_i \quad (4.15)$$

where J_{x_i} and J_{y_i} are Jacobian factors. Obviously, the unit phase volume $\Delta\Phi_1^i = 1$ corresponds to the unit variable spaces

$$\Delta\mathbf{X}_i = 1, \Delta\mathbf{Y}_i = 1 \quad (4.16)$$

The differential cross sections for a single quantized path is

$$\frac{d\sigma}{d\Phi_1^{(i)}} = \frac{d\sigma}{d\mathbf{X}_i} \quad (4.17)$$

$$\frac{d\sigma}{d\mathbf{Y}_i} = \frac{d\sigma}{d\mathbf{X}_i} W(\mathbf{Y}_i|\mathbf{X}_i) \quad (4.18)$$

- Transfer functions for scaled variables

The differential area (dx, dy) corresponds to (dX, dY) in terms of the scaled variables. The number of events generated by Monte Carlo generator, dN , can be expressed with the two variable sets as

$$dN = L_{int} \frac{d\sigma}{dx} w(y|x|M) dx dy = L_{int} \frac{d\sigma}{dX} W(Y|X|M) dX dY \quad (4.19)$$

where $W(Y|X|M)$ stand for TF from X to Y. Thus

$$W(Y|X|M) = \frac{1}{J_y} w(y|x|M) \quad (4.20)$$

Note that factor J_y is a constant for a given event.

Likelihood for a single path, multiple paths and multiple events

- Single path likelihood

A path is specified by a set of dynamical parameters α and 3 integers, $I_p (= 1, \dots, N_p)$ the process number to show signal or background, or which background, $I_t (= 1, \dots, N_t)$ the topology (jet-parton combination) number to show the assignment of jets with partons, and $I_s (= 1, \dots, N_s)$ the solution number of eq.(4.8) for $d_0^{(r)}$ when r is a primary parton. A single path of a process consists of two steps, (a) from the initial partons to produced partons, and (b) from the produced partons to observables. The probability density function for process (a) is $d\sigma/d\Phi_n^*$ for primary partons $p(p_1, \dots, c_n)$ and that for (b) is $W(Y|X|\alpha)$ where observed quantities Y are given. Since processes (a) and (b) are consecutive, the likelihood for a single reconstructed path k for a given event i is given by

$$L_1(\mathbf{p}, \alpha | \mathbf{y} | I_p, I_t, I_s, i, k) = l_0 \left[\frac{d^2\sigma}{d\mathbf{X}d\mathbf{Y}} \right]_{i,k} \quad (4.21)$$

$$= l_0 \left[\frac{d^2\sigma}{d\Phi_n^{(*)}} W(\mathbf{X}|\mathbf{Y}|\alpha) \right]_{i,k} \quad (4.22)$$

$$= \frac{l_0}{J_y^{(i)}} \left[F_r \frac{d^2\sigma}{d\Phi_n^{(f)}} w(\mathbf{x}|\mathbf{y}|\alpha) \right]_{i,k} \quad (4.23)$$

abbreviating I_p, I_t, I_s on the right hand side. If we denote the Jacobian factor for the l -th observable primary parton in the i -th event by $J_{yl}^{(i)}$, then $J_y^{(i)}$ in Eq.(4.23) is defined by

$$J_y^{(i)} \equiv \prod_{l=i}^{N_{obs}^*} J_{jl}^{(i)} \quad (4.24)$$

- Expectation value of likelihood for multiple inferences in an event

The expectation value of the likelihood for dynamical parameters as obtained by a total of K scanning of path for the i -th event is defined by

$$\langle L_1(\alpha | \mathbf{y} | I_p, I_t, I_s, i) \rangle = \frac{1}{K} \sum_{k=1}^K L_1(\mathbf{p}, \alpha | \mathbf{y} | I_p, I_t, I_s, i, k) \quad (4.25)$$

$$= \frac{l_0}{J_y^{(i)} K} \sum_{k=1}^K \left[F_r \frac{d^2\sigma}{d\Phi_n^{(f)}} w(\mathbf{x}|\mathbf{y}|\alpha) \right]_{I_p, I_t, i, k} \quad (4.26)$$

In the form of integration,

$$\langle L_1(\alpha | \mathbf{y} | i) \rangle = \frac{l_0}{J_y^{(i)} \Omega_x} \int ds_r \int d\mathbf{x} \left[F_r \frac{d\sigma}{d\Phi_n^{(f)}} \prod_{r=1}^h \delta(s_r - (\sum_{j=1}^{J_{rp}} d_{rpj})^2) \right] w(\mathbf{y}|\mathbf{x}|\alpha) \quad (4.27)$$

where

$$\Omega_x \equiv \int_{w>0} d\mathbf{x} \quad (4.28)$$

in the multi-dimensional variable \mathbf{x} .

- Likelihood of dynamical parameters from multiple events

The likelihood for α from a set of events, $i = 1, \dots, N_{event}$, is given by the joint likelihood,

$$L_{N_{ev}}(\alpha) = \prod_{i=1}^{N_{ev}} L_1(\alpha|\mathbf{y}|i) > \quad (4.29)$$

since events are mutually independent. The maximum likelihood estimate for α is the value of α that maximizes $L_{N_{ev}}(\alpha)$.

4.2 Application of DLM for *lepton + jets* Channel

As discussed in previous section, DLM can be applied for various analyses such as Higgs boson search, $t\bar{t}$ resonance search and of course top mass measurement. In this section, we describe the way to apply DLM for the top mass measurement in the *lepton + jets* channel.

4.2.1 Reconstruction Procedure in *lepton+jets* Channel

The $t\bar{t}$ decay process in this channel is

$$t_H t_L \rightarrow (W_H b_H)(W_L b_L) \rightarrow (q\bar{q}' b_H)(l\nu b_L)$$

where $l = e, \mu$ suffixes H and L stands for the hadronic decay and leptonic decay of W , respectively. We assume there is no observable difference in b_H and b_L .

Observable partons in this channel are l and 4 jets. The secondary partons are t_H , t_L , W_H , and ν . We summarize the procedure of parton momenta reconstruction from observables and the propagator factor of W_L . The reconstruction procedure is as follows. Our final purpose is to obtain the likelihood using reconstructed parton momenta.

1. Generate top quark mass and determine ΔJES :

In order to search one point which minimize 2D likelihood, we generated M_{top} and ΔJES random-uniformly in a search region, which is $[160, 190]$ GeV/ c^2 and $[-3, 3]$ σ respectively, where ΔJES is a shift from default JES in unit of σ , so that we can calculate the likelihood at this point.

2. Assign jets to quarks:

SECVTX b-tagged jets are regarded as b-jets. In this analysis, at least one b-tagged jet is required for each event. Then we have 12 and 4 combinations in one and double b-tag events, respectively, counting the (q, \bar{q}') and (\bar{q}', q') assignments for W -jets as two combinations. So we have to calculate the likelihood for each combination later.

3. Generate quark momenta:

By procedure 2, we have already known/assumed the correspondence of jets to quarks(b, \bar{b}, q, \bar{q}). We assume directions of quark momenta are equal to those of corresponding jets. Energies of quarks are generated statistically from those of assigned jets by using transfer functions w_b and w_q .

4. Generate the transverse momentum of the neutrino:

The total transverse momentum of the $t\bar{t}$ system at the parton level and the measured one are given,

$$\mathbf{p}_T = \sum_{j=1}^4 \mathbf{c}_{jT} + \mathbf{l}_T + \boldsymbol{\nu}_T, \quad (4.30)$$

$$\mathbf{p}_T^* = \sum_{j=1}^4 \mathbf{c}_{jT}^* + \mathbf{l}_T^* + \boldsymbol{\cancel{E}}_T. \quad (4.31)$$

where asterisk indicate observed quantities. From these equations above, one gets

$$\boldsymbol{\nu}_T = \boldsymbol{\cancel{E}}_T + \sum_{j=1}^4 (\mathbf{c}_{jT}^* - \mathbf{c}_{jT}) + \mathbf{l}_T^* - \mathbf{l}_T + \mathbf{p}_T - \mathbf{p}_T^*. \quad (4.32)$$

$$(4.33)$$

The parton level transverse momentum of the jets denoted as \mathbf{c}_{jT}^* is generated by using the transfer function, In this version of the note we assume $\mathbf{p}_T = \mathbf{p}_T^*$. We also assume that the lepton momentum is measured precisely $\mathbf{l}_T = \mathbf{l}_T^*$.

5. Extract Z-component of the neutrino momentum:

We obtain Z-component of the neutrino ν_Z by solving the mass equation,

$$S_{l\nu} = (l + \nu)^2, \quad (4.34)$$

where $S_{l\nu}$ is generated by random numbers according to the Breit-Wigner shape. If there is no solution of ν_Z (actually there is a case of imaginary solution), we go back to step 3.

6. Calculate dynamical likelihood assuming the event is signal, i.e. $N_p=1$: The explicit form of the likelihood function will be discussed in the next subsection.7. Sum up the likelihood in each mass bin (0.5 GeV/c² step): The number of paths generated from step 1 to 5 is $1(M_{top}) \times 1(N_p) \times N_{top} \times 2(N_{sol})$, where $N_t = 12$ or 4 for 1 or 2 b-tagged event, respectively. We call this unit of paths, i.e. procedures from step 1 to 7, a scan and the total number of scans is denoted by N_{scan} . We made more than 100,000 scans to obtain smooth distributions of the mass likelihood function. After 100,000 times of scanning, we get a stable event likelihood distribution as a function of the top mass and ΔJES .

8. Estimate the effect from wrong jet assignments and background with many pseudo-experiments and then determine the correction factor for the real data in advance.

Figure 4.1 shows summary of analysis procedure. At first, given four jets are corrected by generic jet energy correlation, which is general correction for jets, so we correct jets specifically for this analysis with transfer function. Also we have to correct missing E_T because jet energies are changed by TF. These corrected momenta are considered as parton level quantities, and used for likelihood calculations. The likelihood calculations are divided into three steps: path likelihood, event likelihood and joint likelihood. Details of event likelihood calculations are shown in Figure 4.2. Once we obtain the joint likelihood, we fit the joint likelihood with 2D function to evaluate a top quark mass and JES which maximize the joint likelihood. However, the likelihood calculations are done assuming the event is signal, that is to say, we have to take account for the effects from wrong jet assignments and background. In order to correct these effect, we introduce 2D mapping function as a function of top quark mass and JES. When we evaluate the M_{top} and JES which maximize the likelihood, these values are extracted to true value with 2D mapping function at last.

4.2.2 Transfer Function

Transfer function (TF) deals with relations between parton variables and observables, and corresponds to so-called ‘top specific correction’. TF $w(\mathbf{x}, \mathbf{y}, \Delta JES)$ can be expressed as a function of variable ξ as

$$w(\mathbf{x}, \mathbf{y}, JES) = f(\xi, \mathbf{y}, \Delta JES) \quad (4.35)$$

where \mathbf{x} and \mathbf{y} correspond to parton and jet momentum respectively, and ΔJES is a shift from default jet energy scale in unit of σ . We call variable ξ a ‘response variable’ and defined as the following functional form,

$$\xi = \frac{E_T(parton) - E_T(jet)}{E_T(parton)} \quad (4.36)$$

Since TF depends on E_T and η of jets(See Figures 4.3 and 4.4), the function is divided into 10 E_T bins and 3 η bins so that the number of TF’s we use is 30 in total.

With transfer functions, we reconstruct energy of jets to that of partons as:

1. Obtain ξ randomly along with TF w .
2. Reconstruct energy with ξ

$$\xi = \frac{E_T(parton) - E_T(jet)}{E_T(parton)} \rightarrow E_T(parton) = \frac{E_T(jet)}{1 - \xi} \quad (4.37)$$

3. Reconstruct (p_x, p_y, p_z) of partons with E_T, η, ϕ and mass, where η and ϕ are those of jets, assuming light quark are massless and bottom quark mass is 4.7 GeV/ c^2 .

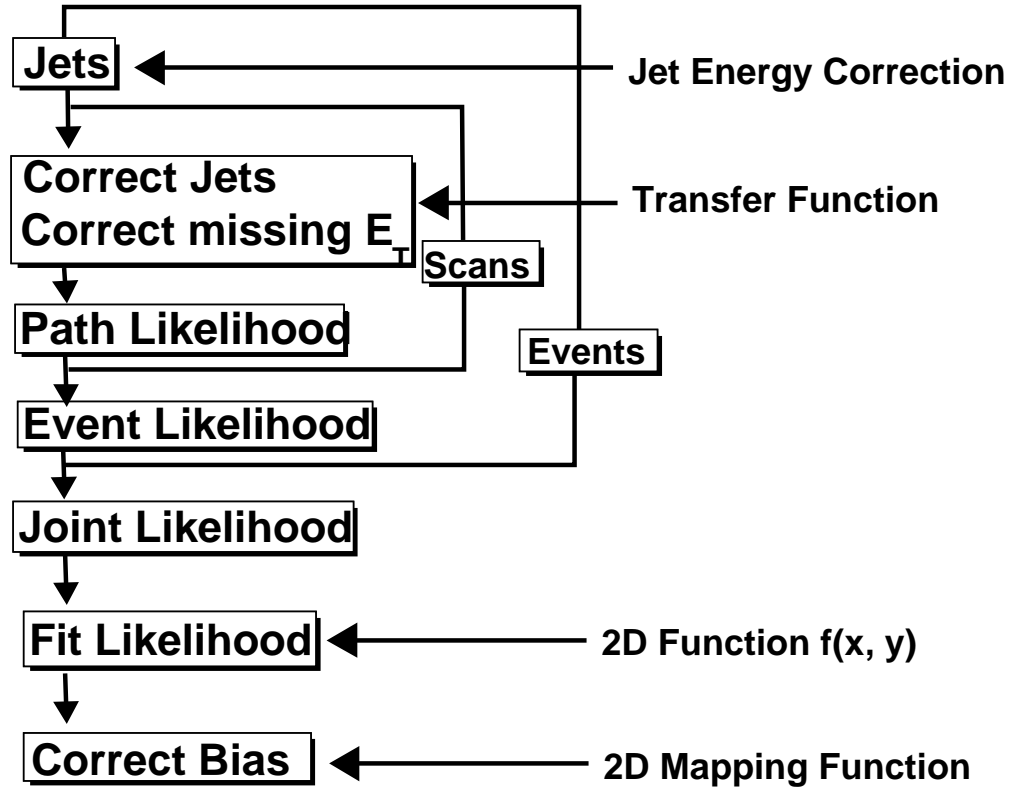


Figure 4.1: Summary of analysis procedure.

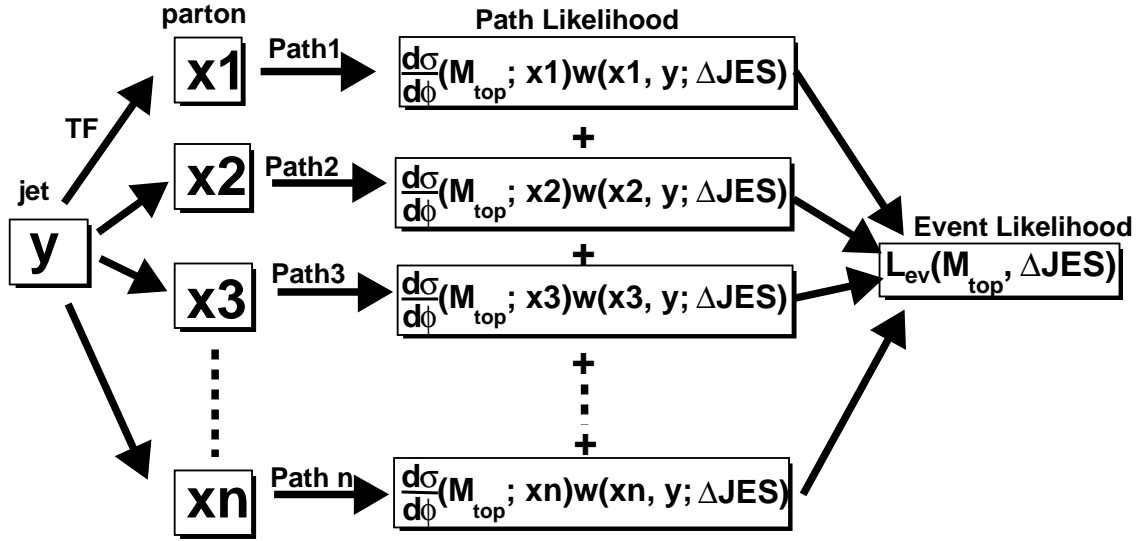


Figure 4.2: A concept of event reconstruction. For a given jet, there are a lot of possibilities that the jet originates from a parton. One of these possibilities are called a path. transfer functions give a weight of a path from a jet to a parton. Actually we take 10000 paths in an event. For each path, we calculate a path likelihood, and the path likelihoods are summed up to obtain an event likelihood. Finally a joint likelihood is obtained by multiplying the event likelihoods each other.

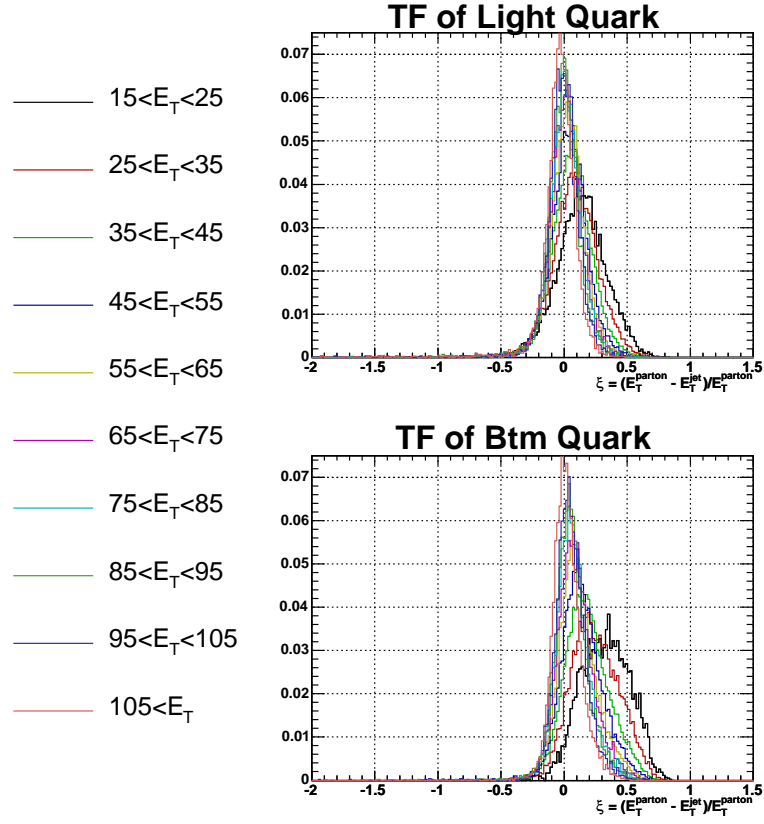


Figure 4.3: E_T dependence of transfer function. Transfer function is divided by 10 bins of E_T . Top and bottom plots are used for light jets and b-jets respectively.

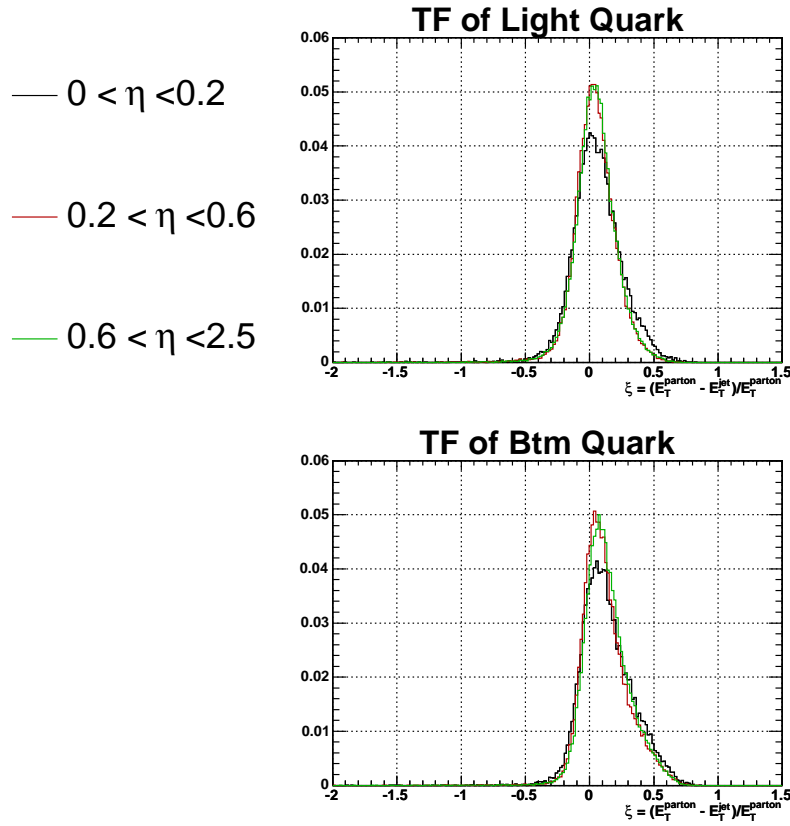


Figure 4.4: η dependence of transfer function. Transfer function is divided by 3 bins of η . The top and bottom plots are used for light jets and b-jets respectively.

4.2.3 TF and Jet Energy Scale

One of the most important point in this analysis is to measure the top quark mass with jet energy scale calibration. In integrating the jet energy scale into the likelihood, we use the transfer function which depends on the jet energy scale. Figure 4.5 shows the transfer function which depends on the jet energy scale. We make 61 transfer functions for each ΔJES ($-3 \leq \Delta JES \leq 3$) so that the likelihood as a function of M_{top} and ΔJES is obtained as,

$$\mathcal{L}^{path}(M_{top}, \Delta JES) = \frac{d\sigma}{d\Phi}(M_{top}, \mathbf{x}) w(\mathbf{x}, \mathbf{y}, \Delta JES) \quad (4.38)$$

By considering dependence of the transfer function on the jet energy scale, we can

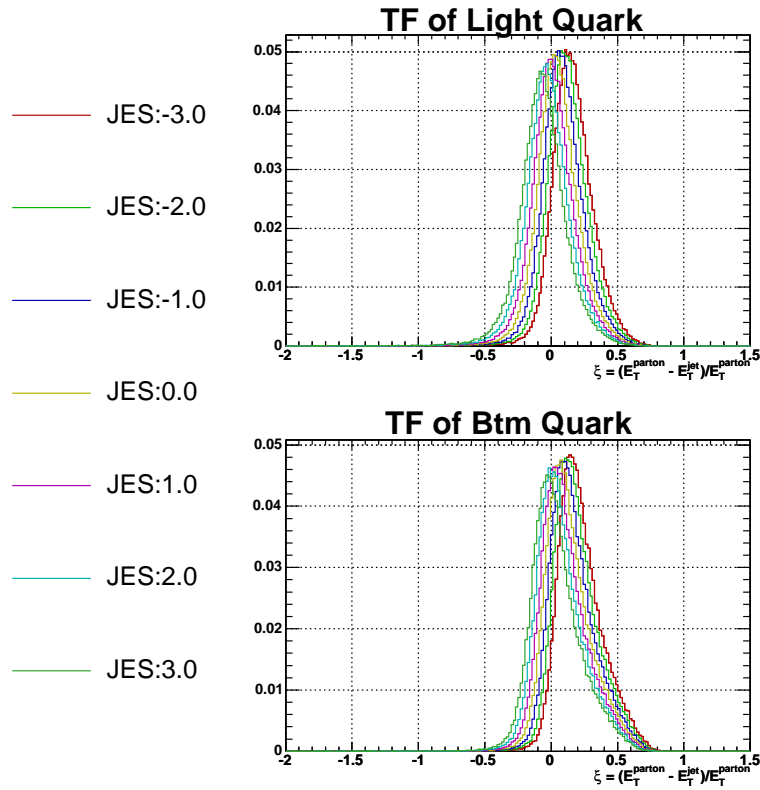


Figure 4.5: JES dependences of transfer function. JES is calibrated by using this dependence of transfer function. We generated 61 transfer function for each ΔJES ($-3 \leq \Delta JES \leq 3$). This plots shows only 7 transfer functions for each ΔJES . Top and bottom plots is used for light jets and b-jets respectively.

calibrate the jet energy scale on real data. Of course in the Monte Carlo event, the jet energy determined by the default jet energy scale should give the most probable likelihood at $\Delta JES = 0.0$ because the transfer function is determined to do so, however,

with real data, if it has offset from the default JES, the likelihood is given at the most probable point which is not $\Delta JES = 0.0$.

Figure 4.6 shows how we reconstruct a jet to a parton in a path with transfer function which depends on JES. In this analysis, there are 61 parton quantities reconstructed with the transfer functions for each ΔJES in a path. Do not confuse that there are two kind of ΔJES , one is ΔJES for transfer function, the other one is ΔJES for input jet energy. In Figure 4.6, the ΔJES for input jet energy y is fixed, on the other hand, ΔJES for transfer function is changed.

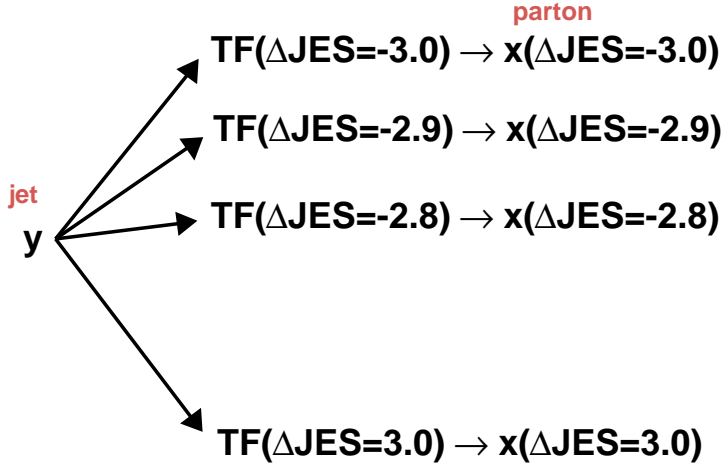


Figure 4.6: Reconstruction procedure for each ΔJES with transfer function. In this analysis, there are 61 parton quantities which reconstructed by transfer functions for each ΔJES in a path. The 'y' is input jet energy whose ΔJES is fixed, on the other hand, ΔJES for transfer function is changed to obtain 'x', which is parton energy.

4.2.4 Performance of Transfer Function

To check the transfer function performance, we apply the transfer function to the events which passed our baseline cuts in the following procedures.

1. jet-parton matching
 Exclusive matching for jets and partons by requiring that the distance(ΔR) between jet direction and parton direction is less than 0.4. 'Exclusive matching' means that if two or more jets are within $\Delta R \leq 0.4$ along a parton direction, we reject the event.
2. Applying the transfer function
 This is performed by random generations of the response variable along each

distribution. Then 2 jets(W) and 3 jets(Top) invariant mass are calculated. The random number generation is repeated more than 10K times(we call it 'scan'). After the scanning, distribution of 2jets/3jets invariant masses are obtained for each event.

3. Pick up the mean of the distribution obtained in procedure 2 for each event. And fill the output mean into the histogram all over the events.

The comparisons of W 2-jets and Top 3-jets invariant masses, before and after transfer function, are illustrated in Figure 4.7. Obviously transfer function improves jets energy from jets energy corrected by generic correction. However this reconstruction by applying transfer function is not enough as you can see. To improve this, we introduce a likelihood using differential cross section and parton level quantities from transfer function. The details of the reconstruction with the likelihood is described in 4.2.5

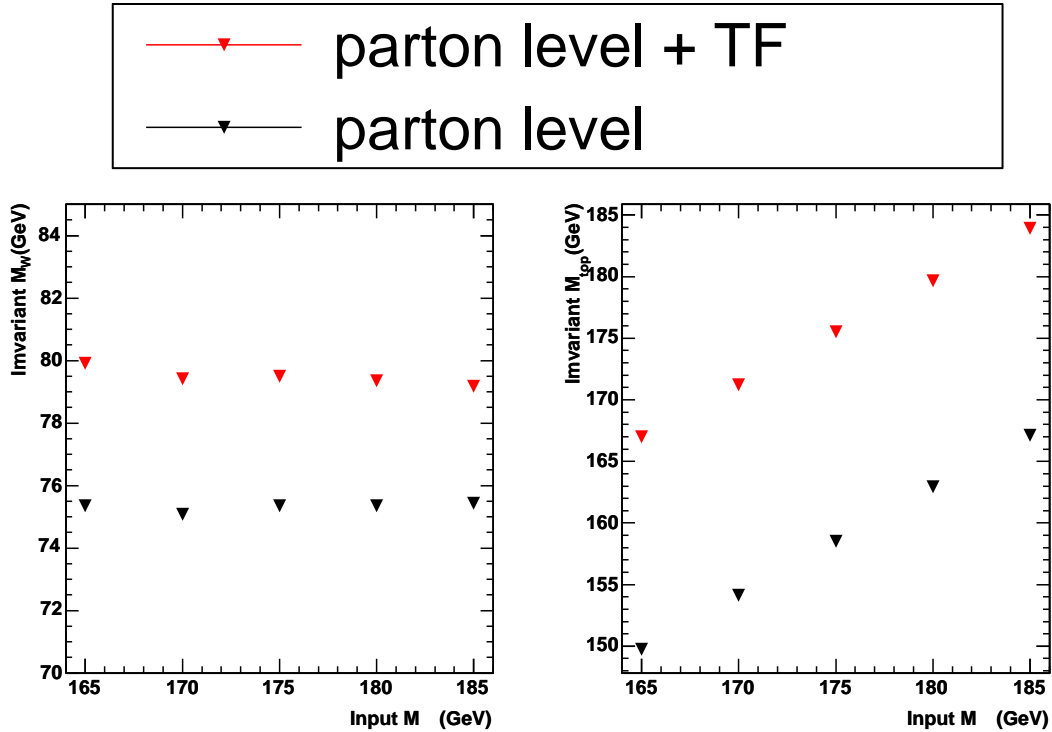


Figure 4.7: The comparisons of W 2-jets and Top 3-jets invariant masses, before and after transfer function is applied. Obviously transfer function improves invariant masses of jet systems compared with those obtained by by Level 5 correction.

We also checked the performance of the transfer function for each ΔJES . Figure 4.8 shows invariant mass for each ΔJES for transfer function, while input jet energy

is fixed at $\Delta\text{JES} = 0.0$. The x-axis represents ΔJES for transfer function. The y-axis shows the invariant mass of hadronic decay W boson in the left plot and the invariant mass of hadronic decay top quark in the right plot.

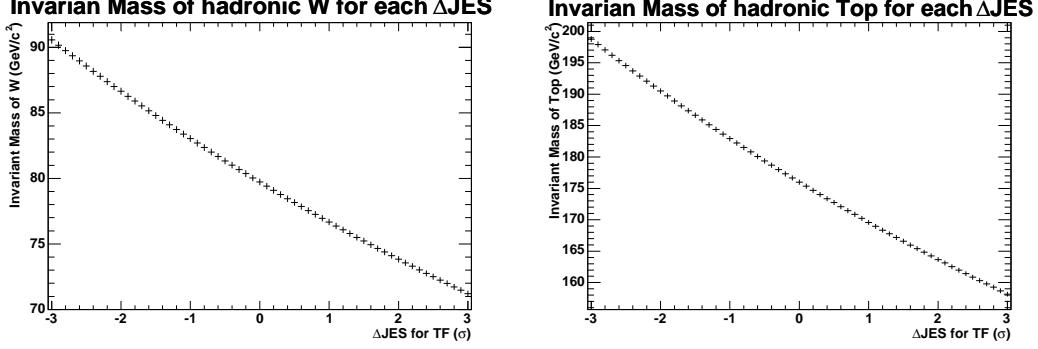


Figure 4.8: Invariant mass for each ΔJES for transfer function, while input jet energy is fixed at $\Delta\text{JES} = 0.0$. The x-axis represents ΔJES for transfer function. The y-axis of the left plot shows the invariant mass of hadronic decay W boson and of the right plot show the invariant mass of hadronic decay top quark.

4.2.5 Likelihood Function in $l+jets$ Channel

As discussed in the previous subsection, we assign l , W_l and b, \bar{b}, q, \bar{q}' as primary partons. Since all reconstructed paths are mutually exclusive, we define the i -th path event likelihood by equations. The i -th event likelihood obtained by the reconstruction procedure described in the previous subsection is given by

$$\mathcal{L}^i(M_{top}) = A_i \sum_{scan} \sum_{I_t} \sum_{I_s} \frac{1}{z_1 z_2} |\mathcal{M}|^2 f_{a/A}(z_1) f_{b/B}(z_2) f_T(p_T) w(\mathbf{y}^i | \mathbf{x} || M_{top}) \quad (4.39)$$

writing variable explicitly, and assuming that $m_a, m_b \approx 1$, in equation above,

$$A_i = \frac{l_0}{J_{y_i} N_{scan} N_t N_s} \cdot \frac{(2\pi)^4}{8P_{beam}^2} \quad (4.40)$$

is a M_{top} independent constant and gives no effect for the maximum likelihood estimate. The parton kinematics is inferred from \mathbf{y}^i and W_L propagator factor by the procedure described in the previous subsection, and used for the evaluation of the parton distribution functions and $|\mathcal{M}|^2$. As for parton distribution function $f_{a/A}(z_1)$ and $f_{b/B}(z_2)$, we employ CTEQ5L in order to be consistent with leading order calculation. The $t\bar{t}$ system transverse momentum distribution $f_T(p_T)$ has been obtained by running PYTHIA generator.

The spin averaged matrix element squared of this channel $|\mathcal{M}|^2$ is factorized to 3 parts: (1) $t\bar{t}$ production $|\mathcal{M}_{t\bar{t}}|^2$, (2) the propagators of the top and anti-top ($|\mathcal{P}_t|^2$

and $|\mathcal{P}_{th}|^2$, and (3) the decay matrices for leptonic and hadronic top decays ($|\mathcal{D}_{tl}|^2$ and $|\mathcal{D}_{th}|^2$). where tl and th indicate leptonic and hadronic decay channels of top respectively. Namely,

$$|\mathcal{M}|^2 = |\mathcal{M}_{t\bar{t}}|^2 |\mathcal{P}_{tl}|^2 |\mathcal{P}_{th}|^2 |\mathcal{D}_{tl}|^2 |\mathcal{D}_{th}|^2 \quad (4.41)$$

The production matrix element for $q\bar{q}$ process can be written as

$$|\mathcal{M}_{t\bar{t}}(q\bar{q} \rightarrow t\bar{t})|^2 = \frac{2g_s^4}{9}(2 - \beta^2 \sin^2 \theta^*) \quad (4.42)$$

where θ^* is an angle between top and incident quark/gluon in the proton in the $t\bar{t}$ center of mass system, and β is a velocity of top and g_s is a strong coupling constant. For gg process, the matrix element can be expressed as,

$$|\mathcal{M}_{t\bar{t}}(gg \rightarrow t\bar{t})|^2 = g_s^4 \left(\frac{1}{6\tau_1\tau_2} - \frac{3}{8} \right) (\tau_1^2 + \tau_2^2 + \rho - \frac{\rho^2}{4\tau_1\tau_2}) \quad (4.43)$$

where

$$\tau_1 = \frac{2(q \cdot t)}{\hat{s}}, \tau_2 = \frac{2(\bar{q} \cdot t)}{\hat{s}}, \rho = \frac{4M^2}{\hat{s}}, \quad (4.44)$$

In these equation, $t\bar{t}$ spin correlation for both $q\bar{q}$ and gg processes are averaged out, for the mass measurement correlations are not required. Besides, whether the $t\bar{t}$ production is via $q\bar{q}$ or gg has no effect on the mass measurement, hence the likelihoods for the two processes are summed up in the event likelihood. The decay matrix elements for the leptonic and hadronic channels are expressed as

$$|\mathcal{D}_{tl}|^2 = \frac{g^4}{4} \frac{(t \cdot l)(b \cdot \nu)}{(S_{l\nu} - M_W^2)^2 + M_W^2 \Gamma_W^2}, \quad (4.45)$$

$$|\mathcal{D}_{th}|^2 = \frac{g^4}{4} \frac{1}{2} \sum_{i \leftrightarrow j} \frac{(t \cdot jet_i)(b \cdot jet_j)}{(S_{2j} - M_W^2)^2 + M_W^2 \Gamma_W^2}, \quad (4.46)$$

where g is weak coupling constant, and $S_{l\nu}$ and S_{2j} represent the invariant masses squared of lepton + neutrino and 2 jets from W respectively. As for the top mass and the decay width of W , we assume the world average value, $M_W = 80.4 \text{ GeV}/c^2$ and $\Gamma_W = 2.1 \text{ GeV}/c^2$. Since z-component of the neutrino momentum is not measured, $S_{l\nu}$ can not be determined directly from observed quantities. Therefore we evaluate this matrix element by generating $S_{l\nu}$ randomly according to the Breit-Wigner form. The generated value of $S_{l\nu}$ also gives the z-component of the neutrino momentum. We make two possible assignments of 2 jets to q and \bar{q}' from W , and the likelihoods corresponding to the two possibilities are averaged.

- **Propagator factors $|\mathcal{P}|^2$**

The top quarks and W bosons are treated as resonances. The simplest form of the propagator factor with resonance mass M is given by the Breit-Wigner form,

$$|\mathcal{P}|^2 \equiv \prod(s) = \kappa \frac{1}{(s - M^2)^2 + M^2 \Gamma^2} \quad (4.47)$$

with $\kappa = 1$.

- **Top mass likelihood**

To extract the top mass, we used the maximum likelihood method. The event likelihood functions are mutually multiplied to get the global likelihood function from N_{ev} events,

$$-2\log(\mathcal{L}(M_{top})) = -2\log\left(\prod_{i=1}^{N_{ev}} \mathcal{L}^i(M_{top})\right) = -2\sum_{i=1}^{N_{ev}} \log(\mathcal{L}^i(M_{top})). \quad (4.48)$$

By the standard treatment of equation above, we obtain the maximum likelihood estimate \hat{M}_{top} and its uncertainty.

4.2.6 Example of the Likelihood

Event likelihood, i.e. the likelihood for each event, is obtained as a sum of the path likelihoods,

$$\mathcal{L}^{event}(M_{top}, \Delta JES) = \sum_{i=0}^{N_{path}} \mathcal{L}_i^{path}(M_{top}, \Delta JES) \quad (4.49)$$

In this analysis, we take 100k paths per event to obtain the event likelihood. Figure 4.9 shows examples of part of an event likelihood with right jet assignments using events which passed the parton-jet matching requirement. Figure 4.10 shows two typical event likelihoods including wrong jet assignments. There are 12 jet assignments for one b -tagged events and there are 4 jet assignments for two b -tagged events. The path likelihood is calculated for all possible jet assignments and summed up each other to obtain the event likelihood. These event likelihoods is contaminated by effect from wrong jet assignments so the maximum points are shifted and blurred from the maximum point using right jet assignment only. Figure 4.11 shows the two typical event likelihoods with background events, one is $Wb\bar{b}$ background and the other one is QCD background.

To obtain a joint likelihood, the event likelihoods are multiplied with all events as

$$\mathcal{L}(M_{top}, \Delta JES) = \prod_{i=0}^{N_{ev}} \mathcal{L}_i^{event}(M_{top}, \Delta JES) \quad (4.50)$$

We use a negative log likelihood defined by

$$-2\log(\mathcal{L}(M_{top}, \Delta JES)) = \sum_{i=0}^{N_{ev}} (-2\log(\mathcal{L}_i^{event}(M_{top}, \Delta JES))) \quad (4.51)$$

to fit and evaluate maximum point and its error. Figure 4.12 shows a typical negative log joint likelihood in a pseudo-experiment(PE).

4.2.7 The Likelihood Fit

To evaluate the maximum point of likelihood and its uncertainties, we fit the joint likelihood with 2D function of the top quark mass and Δ JES as

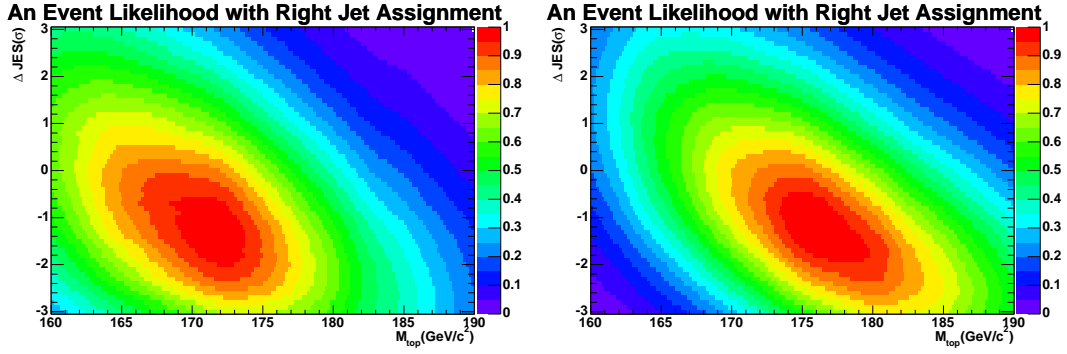


Figure 4.9: Two examples of the signal event likelihoods as a function of M_{top} and ΔJES with right jet assignment with Monte Carlo simulation. Input top quark mass is $175 \text{ GeV}/c^2$ and input ΔJES is 0.0σ .

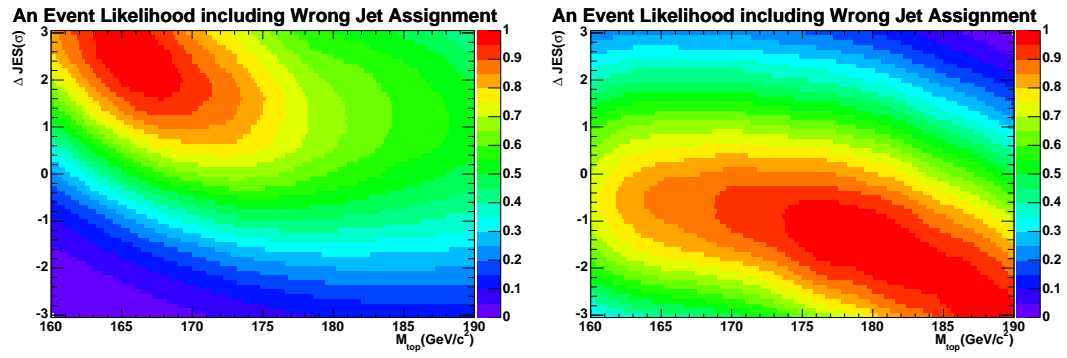


Figure 4.10: Two typical signal event likelihoods as a function of M_{top} and ΔJES including wrong jet assignments with Monte Carlo simulation. Input top quark mass is $175 \text{ GeV}/c^2$ and input ΔJES is 0.0σ .

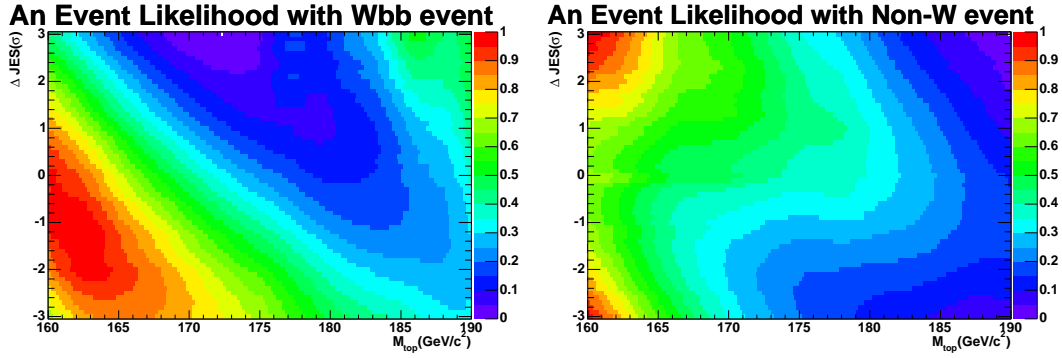


Figure 4.11: Two typical background event likelihoods as a function of M_{top} and ΔJES with Monte Carlo simulation. The left plot is calculated with $Wb\bar{b}$ background and the right plot is calculated with QCD background.

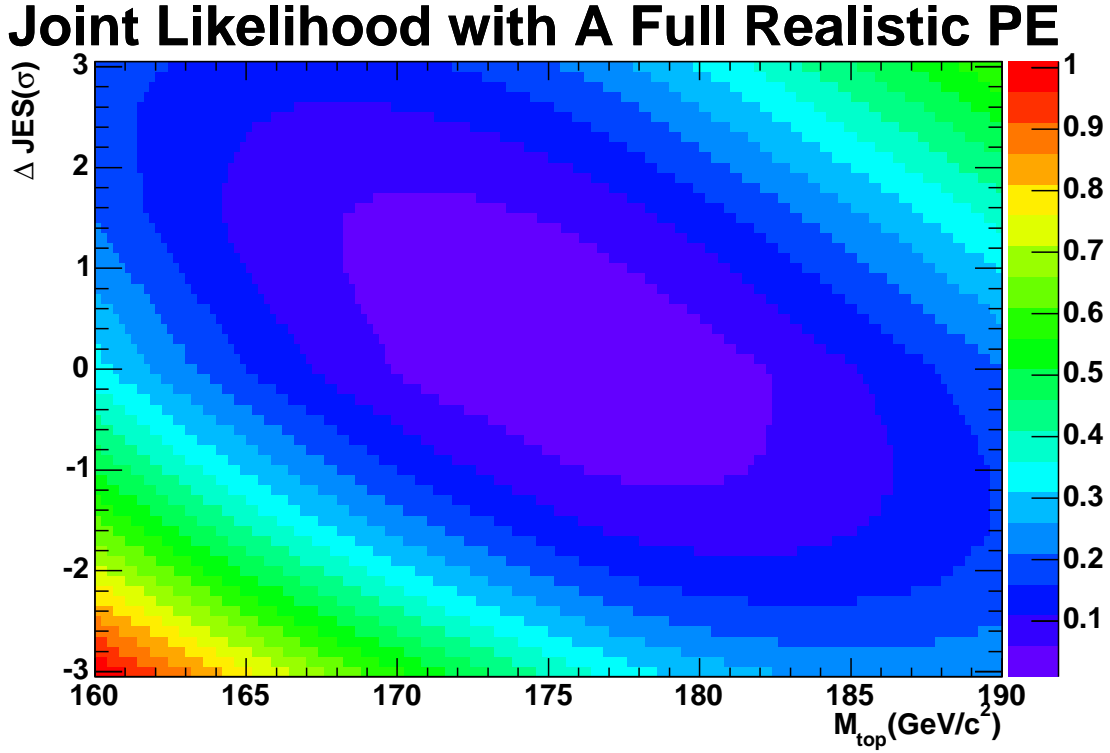


Figure 4.12: An example of the negative log joint likelihood as a function of M_{top} and ΔJES by a realistic pseudo-experiment with Monte Carlo simulation.

$$f(x, y) = ax^2 + by^2 + cxy + dx + ey + f \quad (4.52)$$

where x and y are top mass and Δ JES respectively. Figure 4.13 shows an example of fitting a joint likelihood to this function.

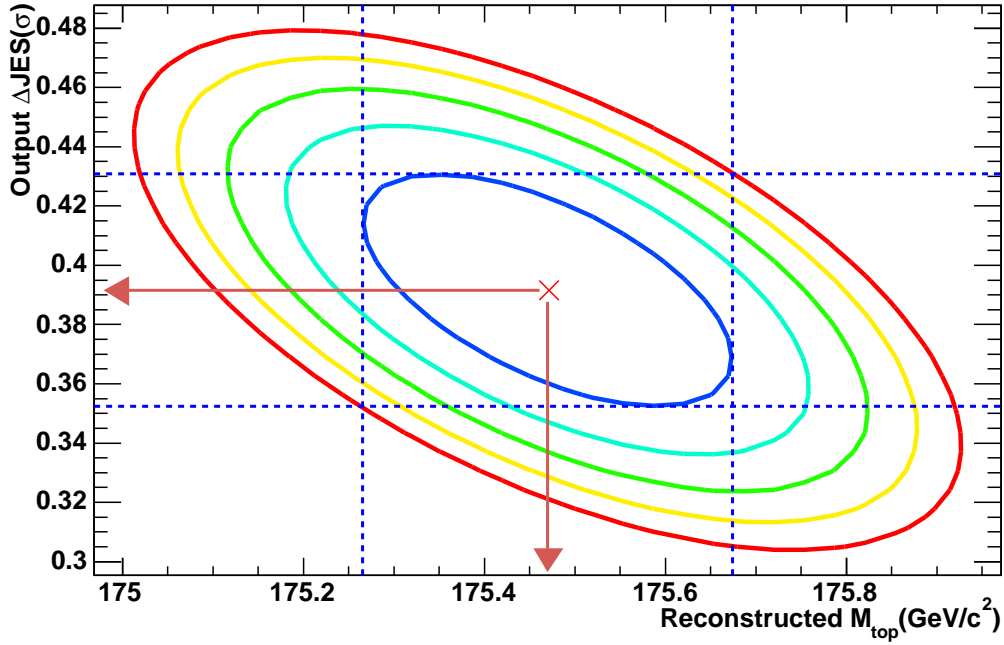


Figure 4.13: Example of 2D fitting. We take a minimum point of negative log likelihood as top mass and Δ JES. The most inner ellipse represents 1σ .

4.3 Performance of the Method

This method is constructed based on ideal assumption that all jet assignments are right and there is no background effect. When we apply this method to real data, we have to take account of the effect from the wrong jet assignments and the background. First we test the method with signal only, then consider the realistic case.

4.3.1 Test with Signal Only

First, we test if our method can reconstruct the true top mass for Monte Carlo samples with five input top masses. The events for each mass sample are selected into three categories as

1. Ideal case:
The events satisfy the jet-parton matching conditions, and we use only right jet assignment for reconstruction.
2. The events satisfy the jet-parton matching conditions, but we use all possible jet assignments for reconstruction.
3. Realistic case with signal only:
We do not require jet-parton matching condition, and use all possible jet assignments for reconstruction.

We reconstruct M_{top} for five mass samples and three categories. For further check, we also use 1D likelihood which is calculated with TF generated by default JES only. Since 1D likelihood is not taken account for dependences on JES, large JES uncertainty is taken. On the other hand 2D likelihood naturally deals with JES. Figure 4.14 and Figure 4.15 show the reconstructed top quark masses and its residuals from input top quark mass, for five input top quark mass, 165, 170, 175, 180 and 185 GeV/c^2 , with signal Monte Carlo sample only. In case of using the sample with right jet assignment, the top quark mass is reconstructed well at 175 GeV/c^2 because TF is made from $M_{top} = 175 \text{ GeV}/c^2$.

4.3.2 Pseudo-experiments with Background

To obtain the numbers of signal events and background events in one pseudo-experiment, first we get a random numbers according to a Gaussian with mean and sigma of the number of background events. Then we fluctuate the number according to a Poisson fluctuation. Next we fluctuate the number of observed events(343) according to a Poisson statistics and then obtain the number of signal events by subtracting number of background events from total number of events. The pseudo-experiments are performed about 140 times for each top quark mass Monte Carlo sample. Figure 4.16 shows the results of the pseudo-experiments. The slopes and constants of the results of pseudo-experiments are not perfect due to the wrong jet assignments and the background contaminations.

4.3.3 Top Mass Extraction

The effects of the wrong jets assignments, the events which do not satisfy jet-parton matching requirement, and the background contaminations shift the reconstructed mass as we already discussed. To correct this effects, we introduce the following 2D mapping functions,

$$x' = ax + by + c \quad (4.53)$$

$$y' = dx + ey + f \quad (4.54)$$

where x , y , x' and y' are the input M_{top} , the input ΔJES , the reconstructed M_{top} and the reconstructed ΔJES , respectively.

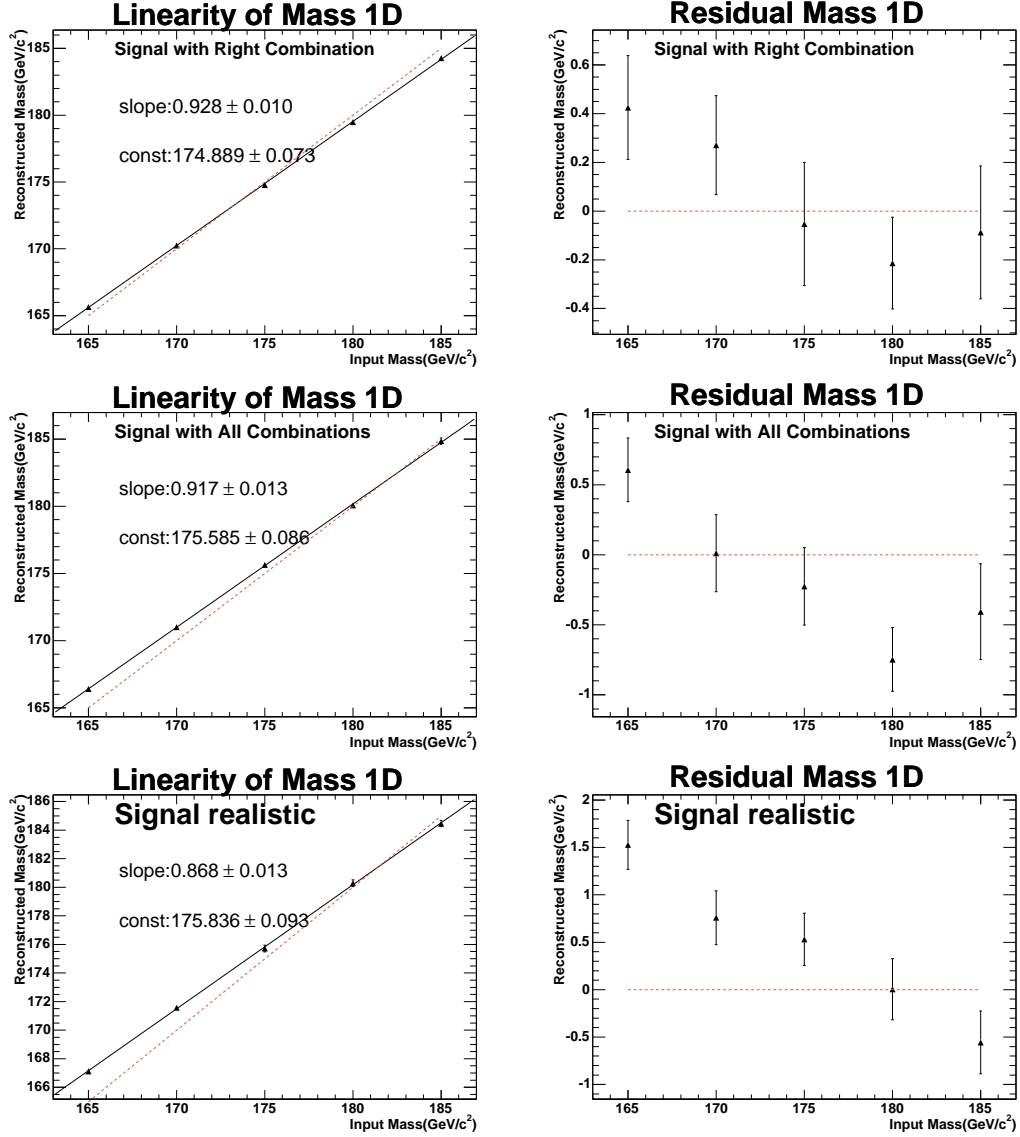


Figure 4.14: Linearities (left three plots) and Residuals (right three plots) of reconstructed mass for different mass samples with 165, 170, 175, 180 and 185 GeV/c^2 , which are obtained by 1D likelihood. Residual is defined by $M_{top}^{reconstructed} - M_{top}^{input}$. The top two plots obtained by using correct jets assignments with matched events with parton, middle two plots obtained by using all possible jets assignments with matched events with parton, and the down two plots obtained by using all possible jets assignments including unmatched events with parton.

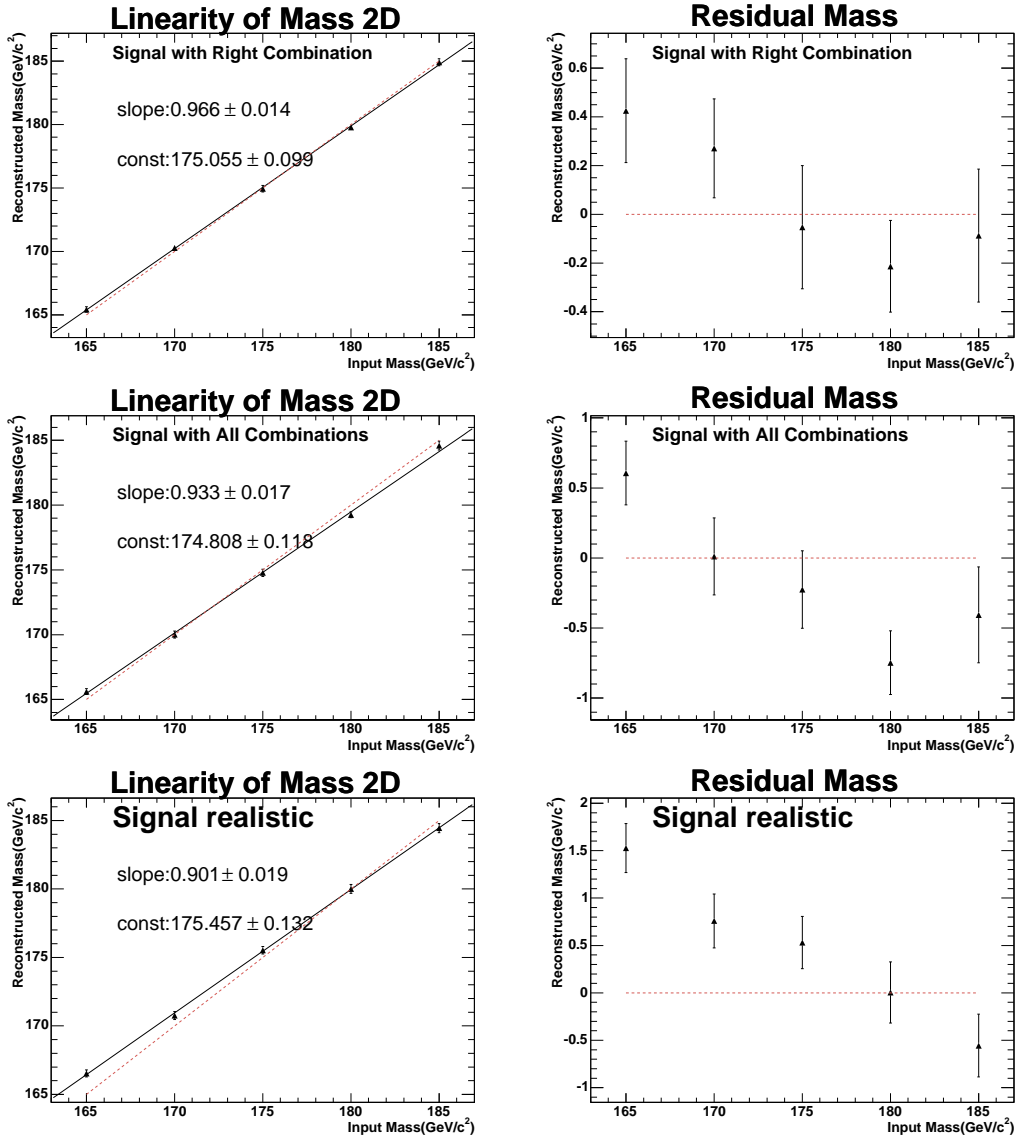


Figure 4.15: Linearities of reconstructed mass for each mass sample with 165, 170, 175, 180 and 185 GeV/c^2 , which are reconstructed with 2D likelihood. The top two plots obtained by using correct jets assignments with matched events with parton, the center of two plots obtained by using all possible jets assignments with matched events with parton and the down two plots obtained by using all possible jets assignments including unmatched events with parton.

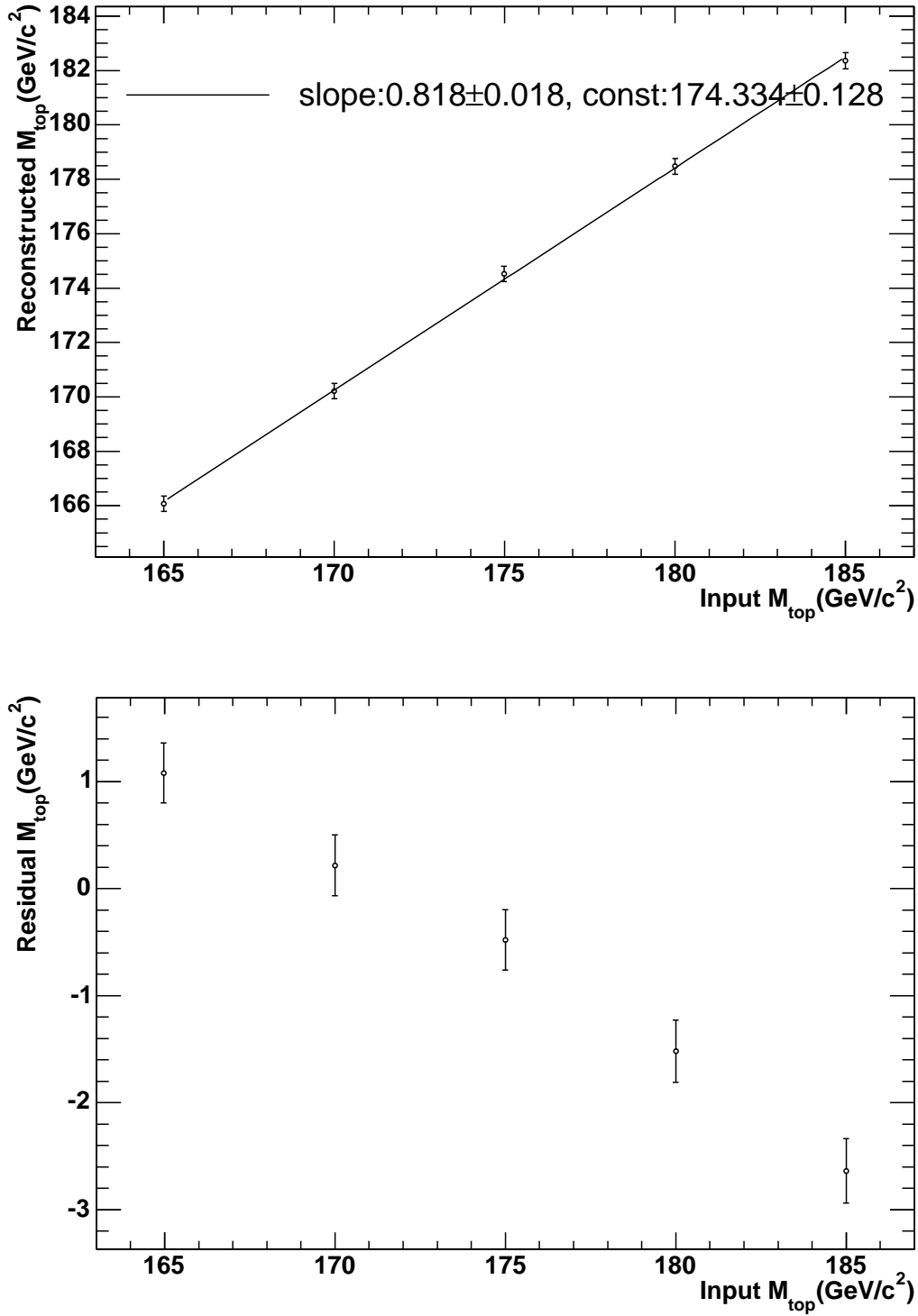


Figure 4.16: The top plot shows the reconstructed M_{top} as a function of input M_{top} and the down plot shows the residual reconstructed M_{top} as a function of input M_{top} . Since the bias can be seen due to wrong jet assignments and background contaminations, the bias should be corrected by a mapping function which is discussed in the next section.

Figure 4.17 shows that 2D mapping functions for M_{top} and ΔJES respectively, which is a function of input M_{top} and input ΔJES . 2D mapping functions represent the responses of the method for each input M_{top} and ΔJES . On the other hand, we can extract true values by solving Equations (4.53) and (4.54) about input M_{top} and ΔJES as:

$$x = Ax' + By' + C \quad (4.55)$$

$$y = Dx' + Ey' + F \quad (4.56)$$

When M_{top} and ΔJES as maximizing the likelihood are obtained by fitting with Equation (4.52), for example, these values are substituted for Equation (4.55) and (4.56) to obtain the true M_{top} and ΔJES . Figure 4.18 shows the residuals between the reconstructed value and the input value as a function of the input M_{top} and ΔJES after correcting with 2D mapping function.

4.3.4 Sanity Check

To check if we can reproduce the true values using the 2D mapping functions, we perform about 140 pseudo-experiments for each samples which include the signal and background, and for five mass samples and five input ΔJES . Figures 4.19 and 4.20 shows that how well we extract the true values. Figure 4.19 shows the relation between the input M_{top} and the reconstructed M_{top} for five input ΔJES 's. As shown in Figure 4.19, any slopes and constants are consistent with the true values within one sigma. Figure 4.20 plot shows the residuals between the input M_{top} and the reconstructed M_{top} for five input M_{top} and five input ΔJES ($5 \times 5 = 25$ in total), fitted to $y = \text{constant}$. The constant from the fit corresponds to 0 within the uncertainty. These plots demonstrate that our method can extract true top quark mass, and also the likelihood is independent of the input JES.

4.3.5 Pull Width

To validate the estimation of the statistical uncertainty, we make the pull distributions. Pull is defined as

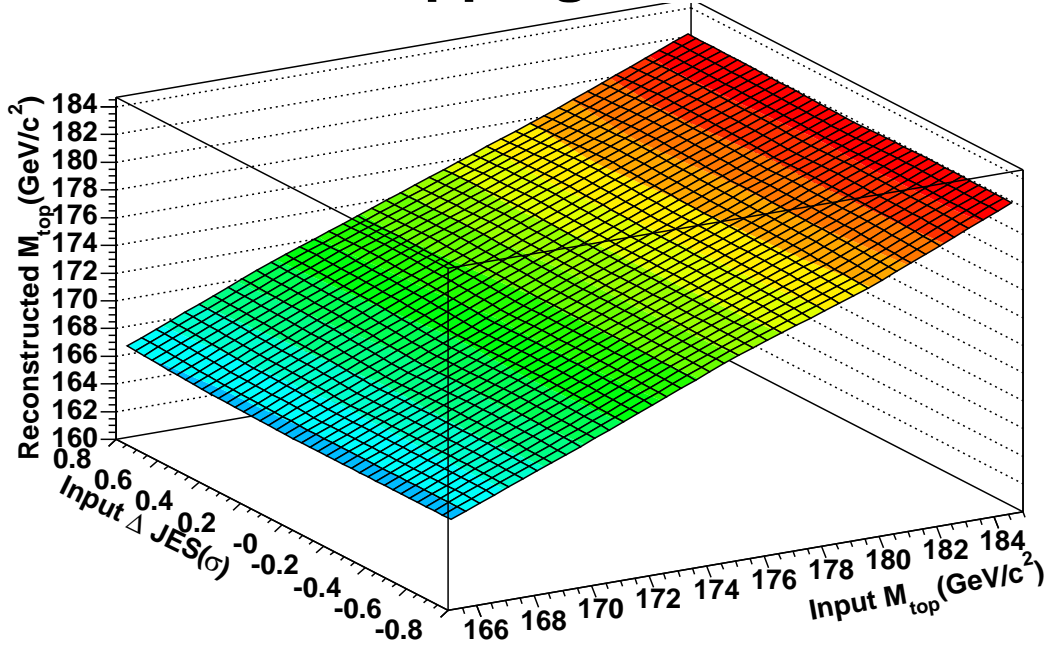
$$\text{Pull} = \frac{M_{rec} - M_{input}}{\sigma} \quad (4.57)$$

$$\sigma = \sigma^+(M_{rec} < M_{input}) \quad (4.58)$$

$$= \sigma^-(M_{rec} > M_{input}) \quad (4.59)$$

We obtain the pull in every pseudo-experiments and fill it in a histogram over all pseudo-experiments and fit the pull distribution to a Gaussian. If our estimation of statistical uncertainty is valid, the σ of fit result with Gaussian (which is called 'pull width') should be 1 otherwise the statistical uncertainty needs to be corrected by the pull width. Figure 4.21 shows the pull width from many pseudo-experiments for five input M_{top} and five input ΔJES , fitted to $y = \text{constant}$. The constant from fit results is

2D Mapping Function



2D Mapping Function for JES

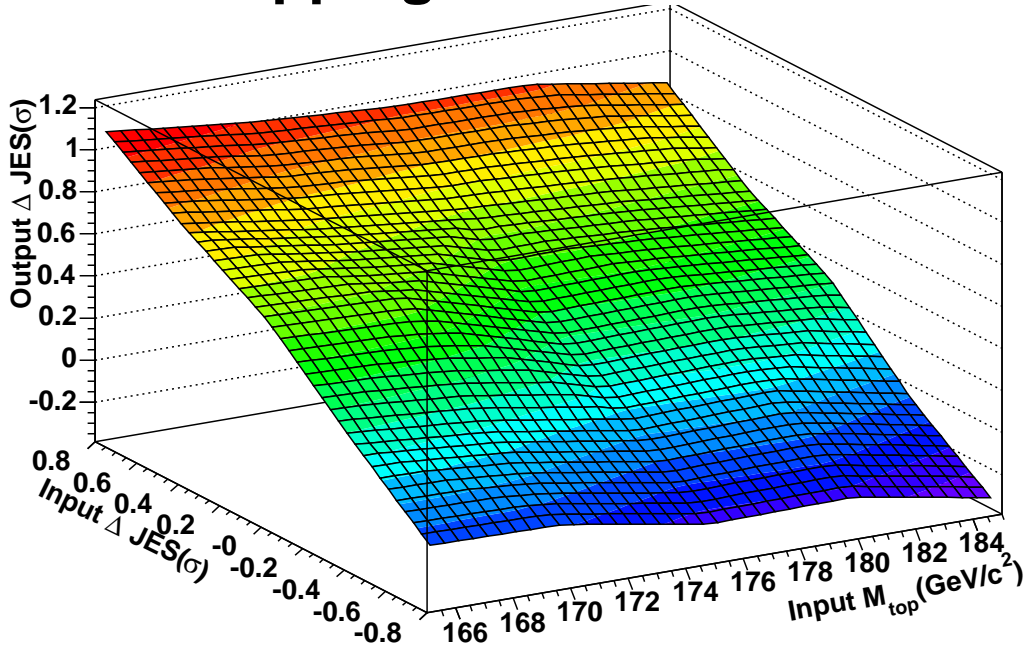


Figure 4.17: 2D mapping function. Since wrong jet assignments and background contaminations make the biases of reconstructions, we have to correct these biases with 2D mapping functions.

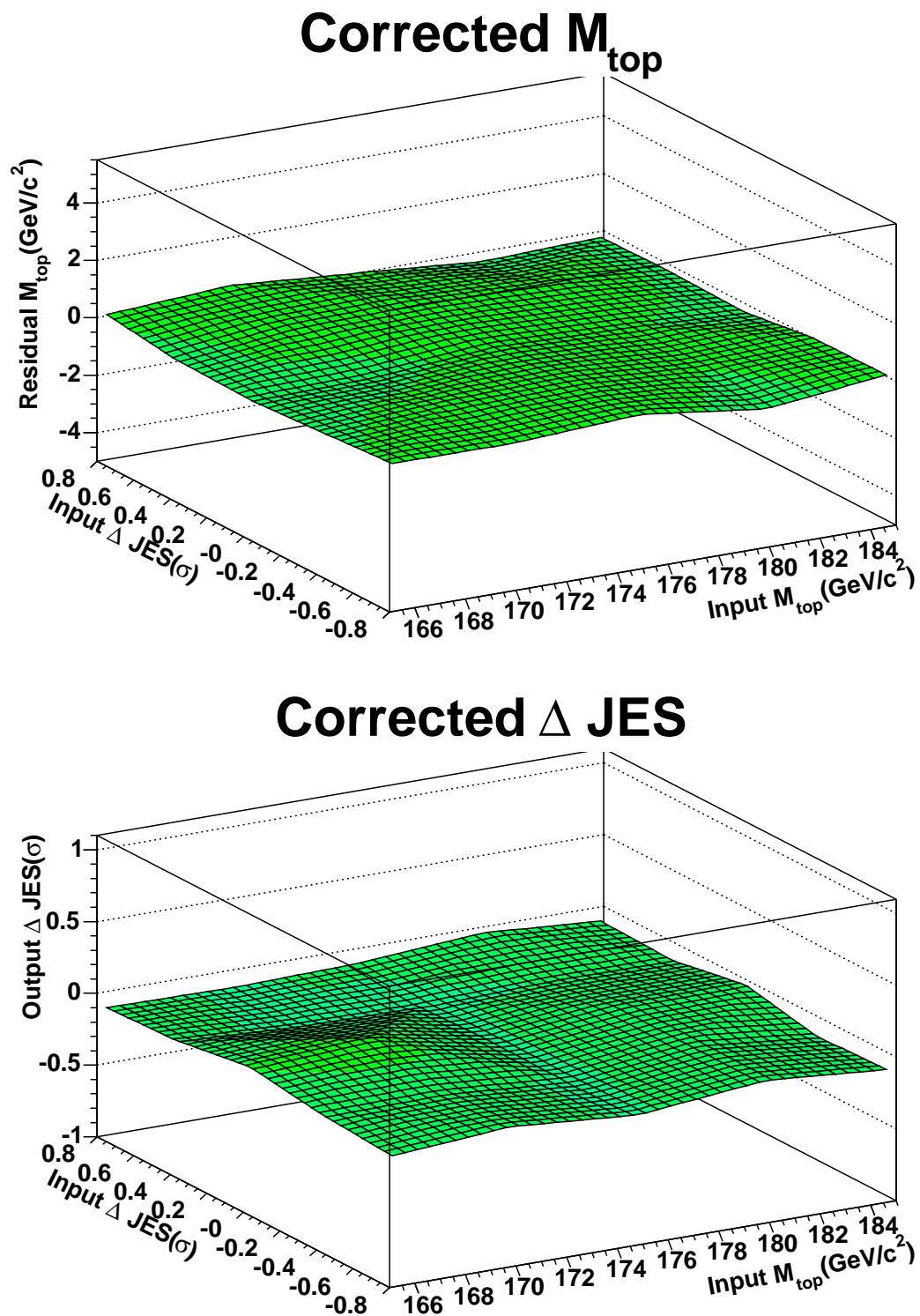


Figure 4.18: The residual reconstructed M_{top} as a function of input M_{top} and ΔJES after correction with 2D mapping function.

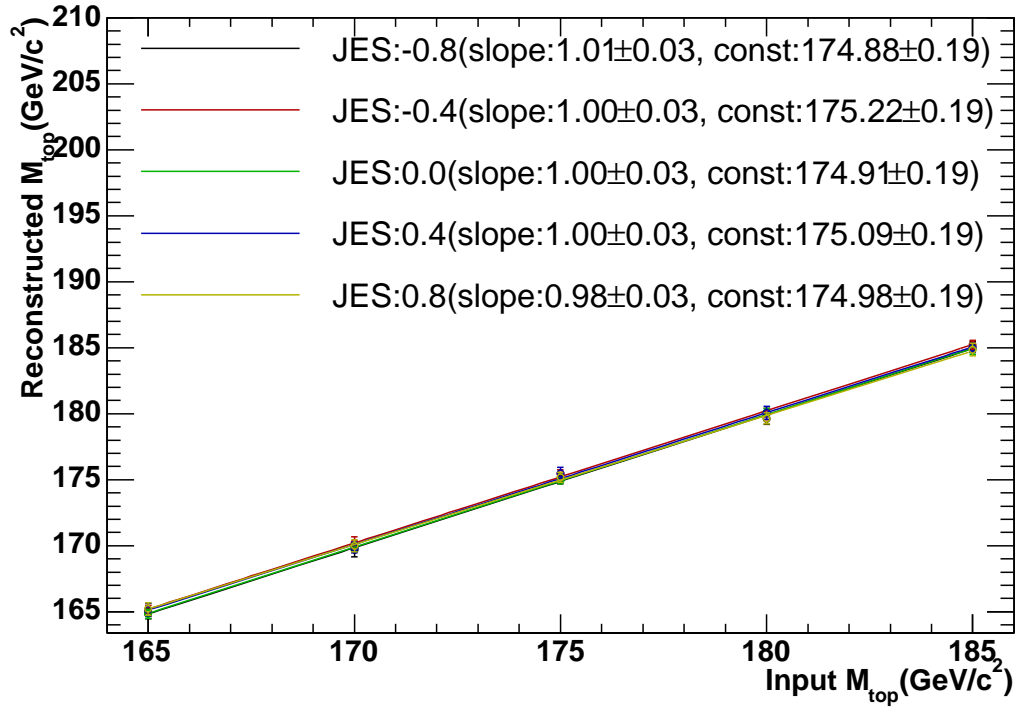


Figure 4.19: Sanity check from many pseudo-experiments including the backgrounds after applying 2D mapping function. The plot shows the relation between the input M_{top} and the reconstructed M_{top} for five input ΔJES 's. The slope of the linear fit is consistent with 1.0.

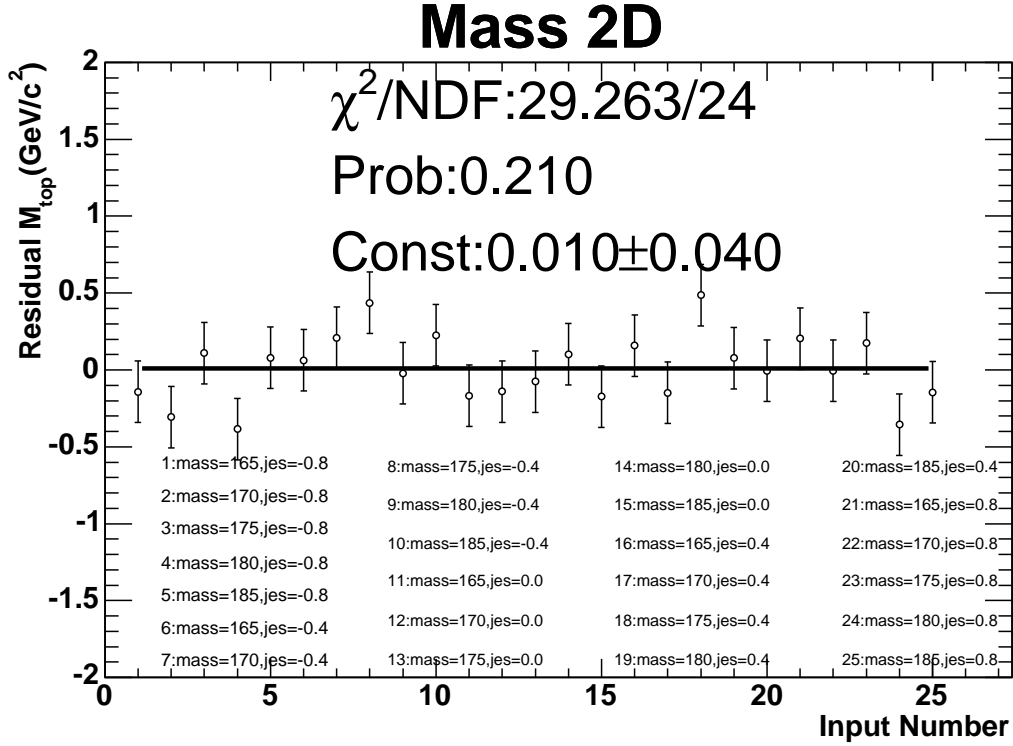


Figure 4.20: Sanity check from many pseudo experiments including background after applying 2D mapping function. The plot shows the residuals between the input M_{top} and the reconstructed M_{top} for five input M_{top} and five input ΔJES ($5 \times 5 = 25$ in total), fitted to $y = \text{constant}$. The constant from the fit corresponds to 0 within the uncertainty.

1.37, which means that we underestimate the statistical uncertainty. We have to correct the statistical uncertainty by multiplying 1.37. Figure 4.22 shows the pull width after correction by a factor of 1.37. The constant from the fit result corresponds to 1 within the uncertainty, which means that our estimation of the statistical uncertainty is good.

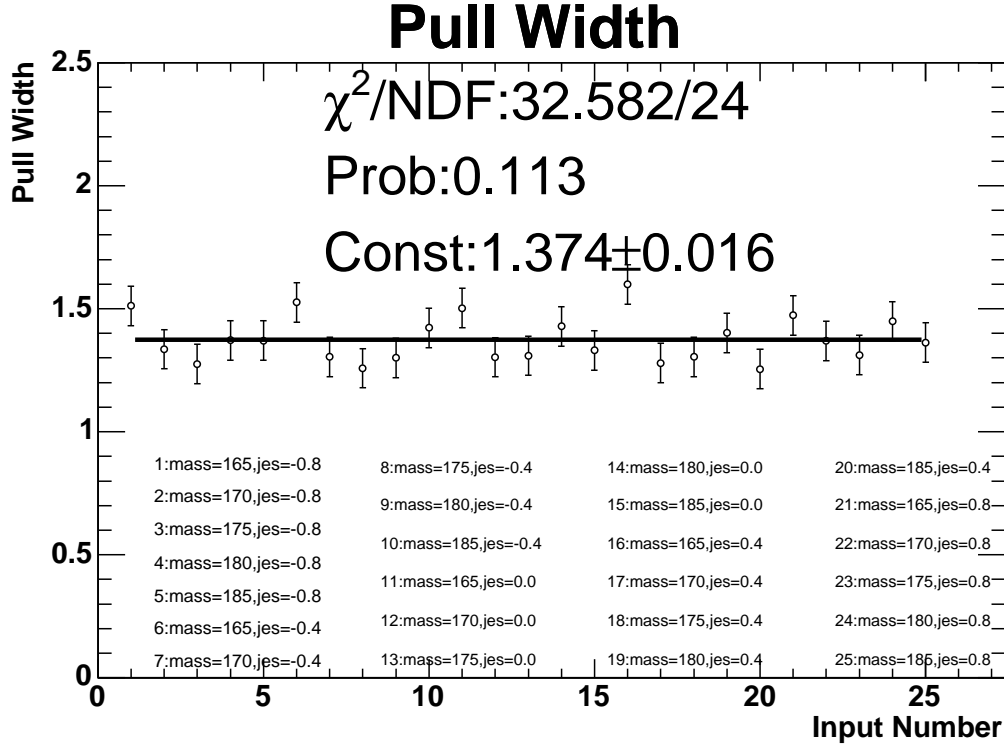


Figure 4.21: The pull width before correction for five mass samples and five input ΔJES . The pull width is 1.37, which means that the statistical uncertainty is underestimated. We have to correct statistical uncertainty by multiplying 1.37.

4.3.6 Blind Test

To investigate each analysis method, we applied this method to 10 ‘blind samples’. Blind sample by definition, its input (true) top quark mass is blinded. User were not informed input top masses and which Monte Carlo generator was used for those samples. Users were informed that the samples contain only signal $t\bar{t}$ events. Therefore, we manually added background events to those samples and applied the mapping function. There were about two thousand events available after event selections for each samples. Three samples were out of range of our analysis region so we apply our method to 7 samples. Figure 4.23 and Figure 4.24 show results. All results are found to be consistent with input top masses within their uncertainties.

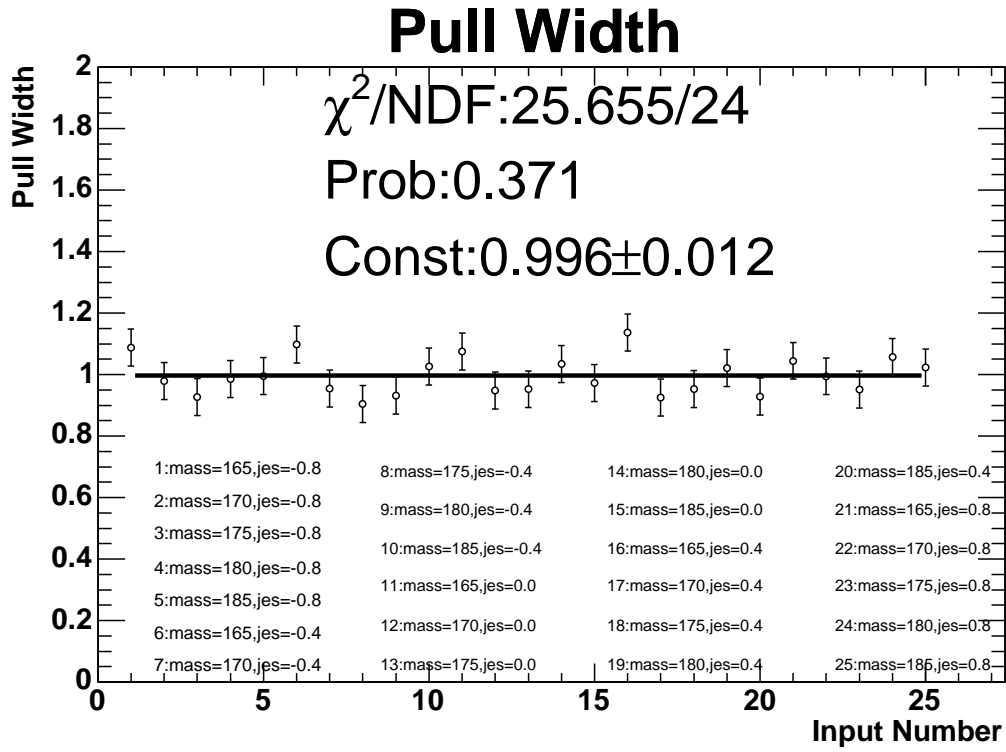


Figure 4.22: The pull width after correction by multiplying 1.37.

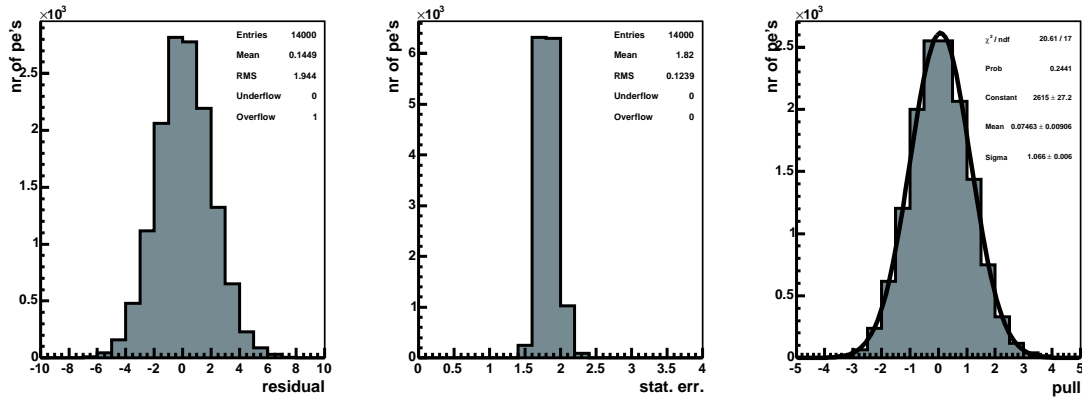


Figure 4.23: The left plot shows residuals for each PE including 7 blind samples, second plot shows statistical uncertainties and right plot shows pull distribution .

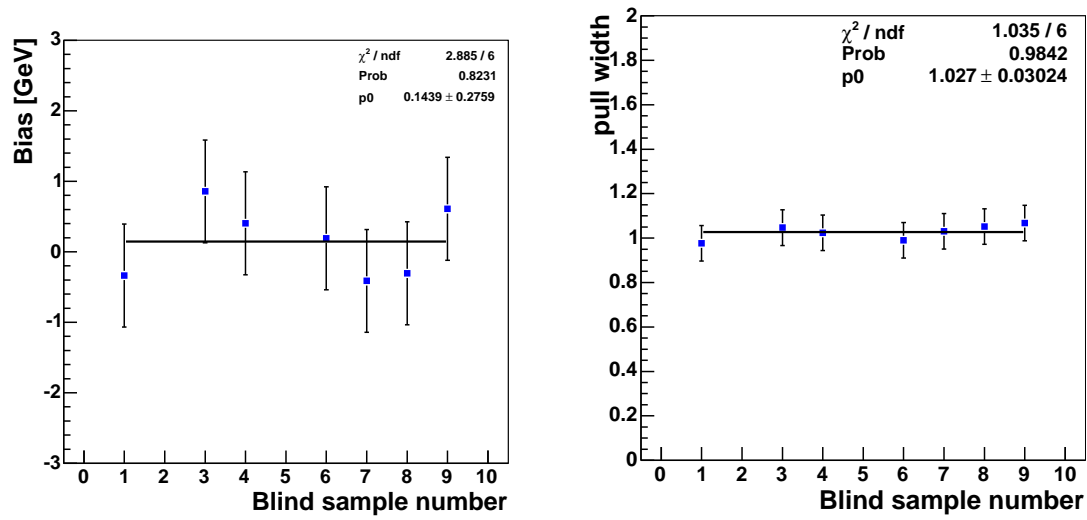


Figure 4.24: The residuals and pulls for 7 blind samples. All results are found to be consistent with input top masses within their uncertainties and pull widths are almost 1.

Chapter 5

The Systematic Uncertainty

We have performed systematics studies with respect to known sources. They are the jet energy scale, PDF's, ISR/FSR, Monte Carlo generators, background composition, background shape, background fraction, b-jet energy scale, multiple interaction, lepton p_T , NLO. The event selection, the transfer function and the likelihood definition are not changed. Systematic uncertainty is separated in two type of groups by the way of estimation. One way is to use the totally correlated samples with default sample to estimate the systematic uncertainty and another way is to use uncorrelated samples to do this. With former way of estimation, we can ignore the statistical uncertainty on reconstructed top quark mass when we compare two samples, the other hand, with another way, we have to take account of statistical uncertainty when we compare two samples, for example, if two samples are completely uncorrelated and the difference between these two samples are smaller than statistical uncertainty, the statistical uncertainty is taken as systematic uncertainty.

5.1 Residual Jet Energy Scale

In calculating the likelihood, the jets is corrected with the generic jet energy correction and the transfer function. Since the uncertainty on the generic jet energy correction is large, the systematic uncertainty on top quark mass from this source become a few GeV/c^2 , for example, it was $5.3 \text{ GeV}/c^2$ in previous analysis [66]. To improve this uncertainty, in this method, the top quark mass is measured with the jet energy scale calibration using 2D likelihood as a function of the top quark mass and the ΔJES . With this method, the likelihood is almost independent on the jet energy scale as shown in Figure 4.19. So the jet energy is calibrated for this process specifically and the statistical uncertainty on the top quark mass includes the uncertainty of the jet energy scale. However additional jet energy scale effects also contribute to the systematic uncertainty. The measured jet energy scale is determined with the W decay matrix element and the top decay matrix elements in the likelihood formula, that is to say, the invariant mass of light jets from W boson are required to be close to W boson mass and also the invariant mass of three jets, jets from W boson and the b-jet, are required

to balance with the invariant mass of charged lepton, neutrino and another b-jet, in the mean time, the same jet energy scale is used for both light jets and b-jets, which do not leads to the accurate invariant mass of W . So Additional systematic uncertainty is assigned for jets corrected by the same jet energy scale. This second order effects are estimated by fluctuating jet energies by $\pm 1\sigma$ on jet energy scale in simulated $t\bar{t}$ events with a top quark mass of $175 \text{ GeV}/c^2$ and fitting with the 2D likelihood. Uncertainty in jet energy, σ , is estimated as a function of η and p_T . The results are shown in Table 5.1, and a sum in quadrature for the differences between the masses fluctuated by $\pm 1\sigma$ for each level of JES is taken as the systematic uncertainty of the residual jet energy scale, $0.62 \text{ GeV}/c^2$ as listed in Table 5.1.

level	σ^-	σ^+	$\Delta M_{top}/2$
1	174.96 ± 0.36	175.54 ± 0.33	0.28
4	175.12 ± 0.34	175.77 ± 0.36	0.33
5	175.21 ± 0.41	174.89 ± 0.37	0.16
6	175.31 ± 0.31	175.12 ± 0.35	0.10
7	174.96 ± 0.33	174.63 ± 0.53	0.33
8	175.01 ± 0.28	175.52 ± 0.43	0.20
Total			0.62

Table 5.1: Residual jet energy scale uncertainties.

5.2 Parton Distribution Function

Parton distribution functions (PDFs) were obtained fitting to a variety of experimental data by groups such as CTEQ and MRST. The CTEQ group estimates the uncertainty in their parameterization with a set of 10 eigenvector pairs of possible variations. The effect of these variations on the top quark mass measurement is included as a systematic uncertainty. Also included are the differences between the top quark masses using CTEQ and MRST PDFs and the effect of varying the Λ_{QCD} scale by $228 \text{ MeV}/c^2$ and $300 \text{ MeV}/c^2$ used in the PDFs.

PDF systematic uncertainties are estimated in events generated at a top quark mass of $175 \text{ GeV}/c^2$ and nominal jet energy scale with CTEQ5L PDFs. The re-weighting technique is used, minimizing large pseudo-experiments with the 2D likelihood. In these pseudo-experiments, $t\bar{t}$ events are weighted according to the ratio between CTEQ5L and the PDF in question. Statistical errors are ignored as the event are almost completely correlated.

The uncertainty from the 20 CTEQ eigenvector pair is estimated by adding the differences between each set in quadrature, resulting in $0.21 \text{ GeV}/c^2$. The difference between CTEQ5L and MRST72 is $0.047 \text{ GeV}/c^2$. Also the difference between MRST75 and MRST72 is $0.034 \text{ GeV}/c^2$. Summing these contributions in quadrature results in

a total PDF systematic uncertainty of $0.23 \text{ GeV}/c^2$. Table 5.2 summarizes the PDF systematic uncertainty.

Sample	ΔM_{top}
MRST75 - MRST72	0.034
MRST72 - CTEQ5L	0.047
20 Eigen Vectors	0.21
Total	0.23

Table 5.2: The table of pdf systematic uncertainty in GeV/c^2 . We take three kind of PDF systematics summed in quadrature.

5.3 Generator

Simulated events are used to determine the transfer function parameters and to test the likelihood. Dependence of the m_t measurement on the event generator is estimated by comparing measurements in events generated with two different event generators, PYTHIA and HERWIG. These generators are independent and have different hadronization models and tuning of underlying events. Using events generated with a top quark mass of $175 \text{ GeV}/c^2$, we observe a difference of $0.54 \pm 0.33 \text{ GeV}/c^2$ in top quark mass measurement between these two generators using the 2D likelihood fit as listed in Table 5.3. We take $0.54 \text{ GeV}/c^2$ as a systematic uncertainty.

Sample	2-D mass (GeV/c^2)
Herwig	175.47 ± 0.28
Nominal(PYTHIA)	174.92 ± 0.17
ΔM_{top}	0.54 ± 0.33

Table 5.3: The systematic uncertainty for the top quark mass dependence on input generator. We compare Pythia with Herwig.

5.4 Initial and Final State QCD Radiation

Simulated events model the initial and final state radiation due to the emission of a gluon according to QCD. Uncertainty in this modeling contributes as a systematic uncertainty. Since the radiation is a non-leading order effect, this systematics also includes some of the error associated with using a leading order event generator. Simulated samples are generated with a top quark mass of $175 \text{ GeV}/c^2$ and with a radiation modeling adjusted to have less or more radiation, signifying one sigma variation from

the nominal modeling. Table 5.4 summarizes the results of measuring the top quark mass in these samples with the 2D likelihood. The largest difference from the nominal in ISR and FSR are each taken as a source of systematic uncertainty, respectively. Note that the systematic uncertainty for more ISR sample is conservatively taken as the statistical error on this difference, $0.35 \text{ GeV}/c^2$. So we take $0.35 \text{ GeV}/c^2$ and $0.54 \text{ GeV}/c^2$ for ISR and FSR as a systematic uncertainty, respectively.

Sample	2-D mass (GeV/c^2)	ΔM_{top}
more ISR	175.03 ± 0.30	0.11 ± 0.35
less ISR	175.02 ± 0.26	0.09 ± 0.32
more FSR	175.47 ± 0.25	0.54 ± 0.34
less FSR	175.44 ± 0.25	0.51 ± 0.30

Table 5.4: The systematic uncertainty for ISR and FSR.

5.5 Background Composition

The uncertainty from number of background is estimated by changing $\pm 1 \sigma$ each number of background sources with the constant total number of background. if a number of a background are increased by $+\sigma$, the number of the other background are reduced by sharing the number of increase equally. The shifts of the top quark mass for 2-D fit due to this effect are shown in Table 5.5. Since the Wcc/c , W +LF and Wbb background are correlated with each other, these errors are just summed up and we take it as the W +jets background systematic uncertainty. The systematic uncertainty for single top and diboson are treated in the same way as W +jets. And then the systematic uncertainties for Non- W , W +jets, single top and diboson are summed in quadrature, resulting in $0.31 \text{ GeV}/c^2$

5.6 Background Shape

We evaluate a systematic uncertainty due to the background generated by ALPGEN generator where the Q^2 scale was multiplied by 2.0 or 0.5. The largest difference from the nominal sample is taken as a systematic uncertainty, $0.28 \text{ GeV}/c^2$ as listed in Table 5.6.

5.7 b-jet Energy Scale

We also have to estimate uncertainty due to b fragmentation and b -semileptonic decays modeling uncertainties. The study on these uncertainties already has been done in the

Sample	$+\sigma$ 2-D mass (GeV/c^2)	$-\sigma$ 2-D mass (GeV/c^2)	$\delta M_{top}(M_{top} - nominal)$
Non-W	174.79	175.02	0.13
W+LF	174.91	175.84	0.06
Wcc/Wc	174.98	174.98	0.08
Wbb	174.85	175.03	0.11
Single top(t-ch)	174.89	174.87	0.05
Single top(s-ch)	174.95	174.93	0.03
WW	174.93	174.93	0.01
WZ	174.86	174.94	0.06
ZZ	174.92	174.93	0.01
Total			0.31

Table 5.5: The systematic uncertainty from the number of background for 2-D analysis.

Sample	2-D mass (GeV/c^2)	δM_{top}^{2D}
nominal	174.92 ± 0.17	
factor=0.5	175.17 ± 0.19	0.25 ± 0.25
factor=2.0	175.20 ± 0.17	0.28 ± 0.24

Table 5.6: The systematic uncertainty from the background shape uncertainty which is obtained using two different Q^2 samples.

top quark mass analysis in the past by changing $\pm 1\sigma$ of the parameters for b fragmentation modeling and b -semileptonic branching ratio in the Monte Carlo generators respectively. According to this study, the systematic uncertainty on the top quark mass from this effect is estimated by changing $\pm 1\%$ of b-jet energy and then multiplying half of difference on the top quark mass by 0.6. The difference of top mass is shown in Table 5.7 and $0.40 \text{ GeV}/c^2$ is taken as b-jet energy scale systematic uncertainty.

Sample	2-D mass (GeV/c^2)
b-JES -1%	174.19 ± 0.34
b-JES $+1\%$	175.52 ± 0.34
ΔM_{top}	0.67
$\Delta M_{top} \times 0.6$	0.40

Table 5.7: The systematic uncertainty for b-jet energy scale.

5.8 Multiple Interaction

Simulated events were generated in a limited range of the full dataset and therefore have lower average instantaneous luminosity. The increase in instantaneous luminosity results in an increase in multiple interactions and can be measured via the number of reconstructed vertices. A systematic uncertainty is assigned for the uncertainty on the modeled multiple interactions in simulated data. The effect is estimated by parameterizing jet E_T as a function of the number of reconstructed vertices and varying these energies according to the distribution of vertices in the full dataset. The estimate results in $50 \text{ MeV}/c^2$ for analyses directly measuring the jet energy scale systematic uncertainty.

5.9 Lepton p_T

Uncertainty in the modeling of charged lepton p_T in simulated data contributes to the systematic uncertainty in the measurement of the top quark mass. The uncertainty of the lepton p_T has been very conservatively estimated to be 1%. To estimate the effects of this uncertainty, pseudo-experiments are performed generated at a top quark mass of $175 \text{ GeV}/c^2$ and the nominal jet energy scale. Table 5.8 shows that reconstructed mass with lepton p_T shifted by $\pm 1\%$. The events are completely correlated between pseudo-experiments, so statistical error is ignored. The half of the difference between the top quark masses with lepton p_T shifted by $\pm 1\%$, $0.28 \text{ GeV}/c^2$, is taken as the systematic uncertainty as listed in Table 5.8.

Sample	2-D mass (GeV/ c^2)
lepton $p_T -1\%$	175.28 ± 0.44
lepton $p_T +1\%$	174.72 ± 0.46
δM_{top}	0.28

Table 5.8: The systematic uncertainty from effect of lepton p_T .

5.10 NLO

PYTHIA and HERWIG are both leading-order MC generators, so approximately 95% of $t\bar{t}$ events in these samples are produced from $q\bar{q}$ pairs and 5% produced from gg pairs. However, NLO expectations are closer to 85% $q\bar{q}$ and 15% gg production. Also our method uses a matrix element calculated by tree-level. We estimate the effect from NLO on the top quark mass reconstruction with our method and the results are shown in Table 5.9. The largest difference from the nominal sample is taken as the NLO systematic uncertainty, 0.41 GeV/ c^2 .

Sample	2-D mass (GeV/ c^2)	δM_{top}^{2D}
nominal	174.92 ± 0.17	
MRST02	174.87 ± 0.36	0.05 ± 0.40
CTEQ5M	174.52 ± 0.34	0.41 ± 0.38

Table 5.9: The systematic uncertainty from NLO effect.

5.11 b-tagging Efficiency

Modeling of secondary vertex tagging in simulated events has an uncertainty associated with it. This uncertainty is determined including the E_T dependence of a scale factor ϵ for b-tagging efficiency between experimental and simulated data. The nominal scale factor is 0.91. The scale factor shifted by $\pm 1\sigma$ are given by:

$$\epsilon^+ = 0.842 + 0.00118 \times E_T \quad (5.1)$$

$$\epsilon^- = 0.978 + 0.00118 \times E_T \quad (5.2)$$

where ϵ^\pm represents $\epsilon \pm 1\sigma$. A systematic uncertainty is estimated for this effect by weighting events in pseudo-experiments with the appropriate scale factor. An event is weighted for each jet associated with a secondary vertex. No weight greater than unity is allowed. The top quark masses measured in weighted pseudo-experiments with the 2D likelihood fit are shown Table 5.10. Half of the difference between ϵ^\pm is taken as the systematic uncertainty, 0.005 GeV/ c^2 .

Sample	2-D mass (GeV/c^2)
ϵ^+	175.24 ± 0.30
ϵ^-	175.25 ± 0.29
δM_{top}	0.005

Table 5.10: The systematic uncertainty from the b-tagging efficiency.

5.12 Calibration

Since we use the 2D mapping function to extract the true top quark mass, the uncertainty on calibration using 2D mapping function is taken as a systematic uncertainty. We take $0.048 \text{ GeV}/c^2$ as the calibration uncertainty from Figure 4.19.

5.13 Background Fraction

Background fraction of observed events should affect the top mass reconstruction. The systematic uncertainty is estimated by shifting the total number of background by $\pm 1\sigma$ but each background fractions is fixed. Table 5.11 shows the reconstructed top quark mass changing the total background fraction by $\pm 1\sigma$. The largest difference from the nominal sample is taken as systematic uncertainty, $0.17 \text{ GeV}/c^2$.

Sample	2-D mass (GeV/c^2)	δM_{top}^{2D}
nominal	174.92 ± 0.17	
+1 σ	174.83 ± 0.17	0.09
-1 σ	175.06 ± 0.18	0.17

Table 5.11: The systematic uncertainty from background fraction.

5.14 Summary of systematic uncertainties

The total systematic uncertainty is estimated by summing each source of systematics in quadrature and $1.32 \text{ GeV}/c^2$ is taken as a total systematic uncertainty. Table 5.12 shows a summary of systematics.

Systematic	2-D systematic (GeV/c^2)
Residual JES	0.62
PDF	0.23
ISR	0.35
FSR	0.54
Generator	0.54
lepton p_T	0.28
Background shape	0.28
Background composition	0.31
Background fraction	0.14
b-jet energy scale	0.40
b-tagging efficiency	0.01
NLO	0.41
Calibration	0.05
Multiple interaction	0.05
Total	1.32

Table 5.12: The total systematic uncertainty.

Chapter 6

Results and Discussion

6.1 Candidates Events and Results of the Fit

We have 343 events in *lepton+jets* channel as $t\bar{t}$ candidates and the joint likelihood is shown in Figure 6.1. A cross mark in Figure 6.1 is the point which maximize the likelihood and the blue ellipse represents 1σ . The range obtained by projecting the blue ellipse to an axis of M_{top} is taken as a statistical uncertainty which contains jet energy scale uncertainty. The measured top quark mass before applying the correction by 2D mapping function and pull width is $171.8 \pm 1.1 \text{ GeV}/c^2$. After the 2D mapping correction, the top quark mass was measured to be $171.6 \pm 1.4 \text{ GeV}/c^2$ and then the statistical uncertainty is $\pm 2.0 \text{ GeV}/c^2$ after the pull width correction. Finally we obtain top quark mass to be

$$M_{top} = 171.6 \pm 2.0 \text{ GeV}/c^2 \quad (6.1)$$

6.2 Validation of Statistical Uncertainty

To validate the measured statistical uncertainty obtained from data, we perform 6k pseudo experiments with $170 \text{ GeV}/c^2$ mass sample. Figure 6.2 shows the expected statistical uncertainty with pseudo-experiments using resampling technique. Since we have only about 40k $t\bar{t}$ Monte Carlo events, so if we perform the pseudo-experiments exclusively, only around 100 pseudo-experiment are done. In order to compensate the statistics to estimate the expected statistical uncertainty, the resampling technique use the events which are already used in the other pseudo-experiments. 68.3% of pseudo-experiments have smaller statistical uncertainty than the measured one.

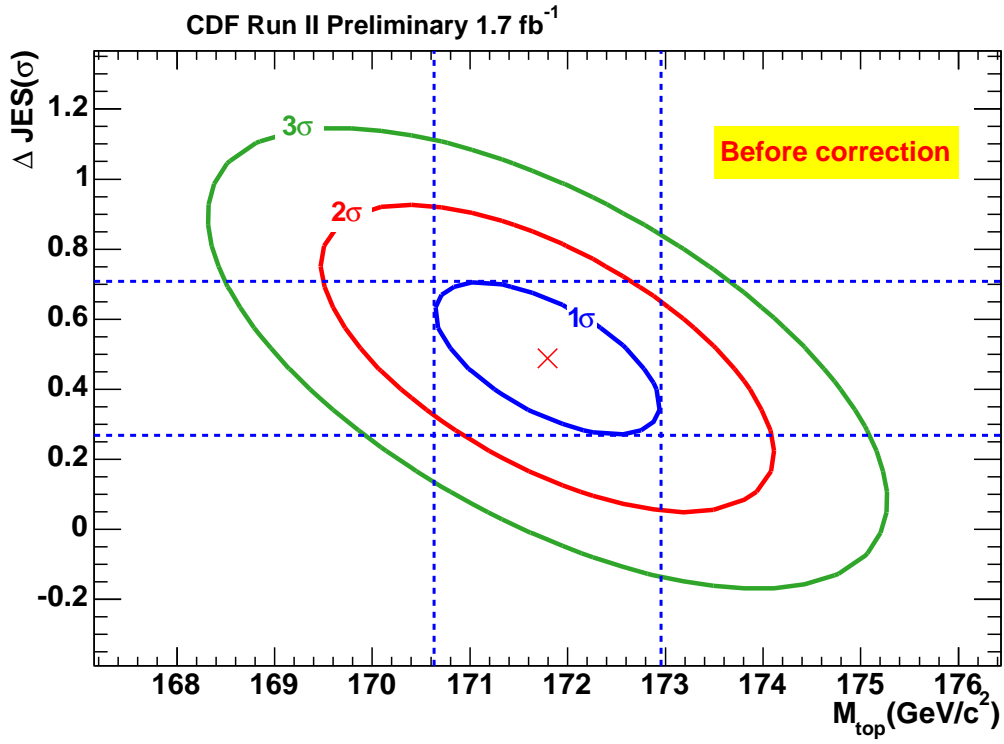


Figure 6.1: The fit result of joint likelihood with 343 events of CDF data before applying correction of 2D mapping function and pull width. The cross mark corresponds to minimum point and blue curve represents one σ .

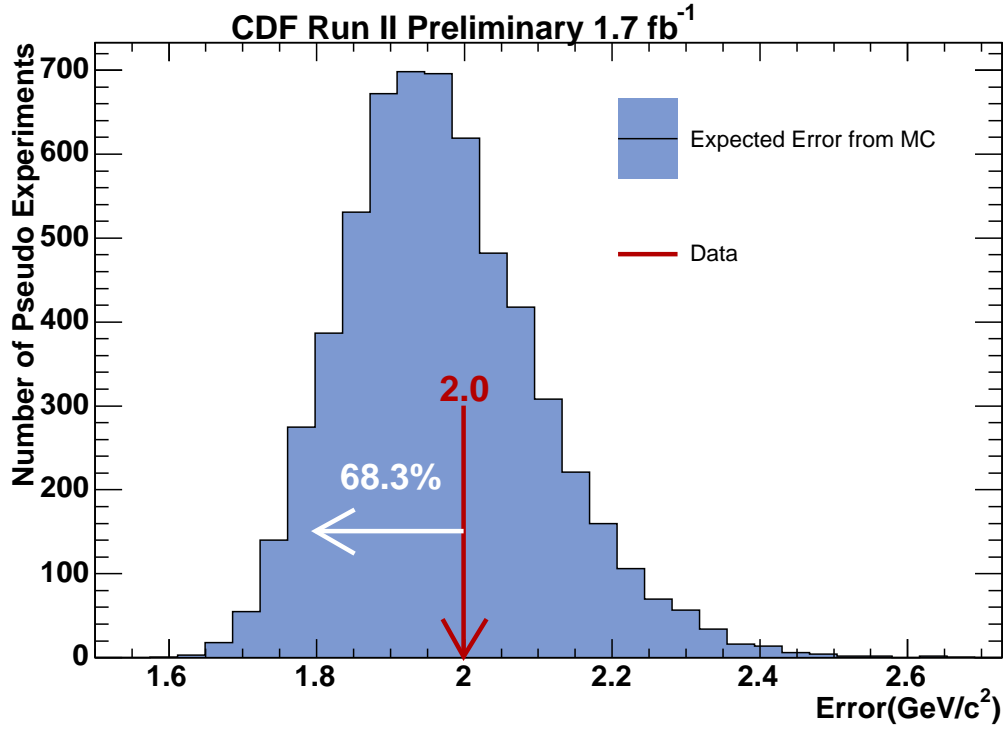


Figure 6.2: The measured statistical uncertainty with 2D fit which include JES uncertainty is consistent with expected statistical uncertainty with 6k pseudo-experiments. 68.3% of total number of pseudo-experiments are smaller than the observed statistical uncertainty.

6.3 Discussion

We measured top quark mass precisely with the jet energy scale calibration. With the 2D likelihood, about 80% of the jet energy scale uncertainty is reduced as compared with the 1D likelihood. The jet energy scale uncertainty is taken into account for statistical uncertainty, not systematic uncertainty, so the jet energy scale uncertainty is expected to be reduced more as the integrated luminosity increases. On the other hand, the statistical uncertainty on the top quark mass is approaching the total systematic uncertainty, so in the near future, the systematic uncertainty is larger than the statistical uncertainty as shown in Figure 6.3. We have to consider to reduce systematic uncertainties such as ISR, FSR and b-jet energy scale. As shown in Figure 6.3, there is a lot of analyses on the top quark mass measurement in CDF. This Figure shows the results with the total integrated luminosity of 1.0 fb^{-1} until March 2007, so the latest results with total integrated luminosity of 1.7 fb^{-1} are of course better than that. There are two other analyses with the same statistics in *lepton + jets* process. One is called “MTM method” [67], the other one is called “Template Method” [68]. These two results are also higher than the current world average of $170.9 \pm 1.8 \text{ GeV}/c^2$ on March 2007. So the world average on the top quark mass is expected to be higher than before with latest results. The prediction of Higgs boson mass as shown in Figure 1.8 is expected to approach to the Standard Model Higgs mass region.

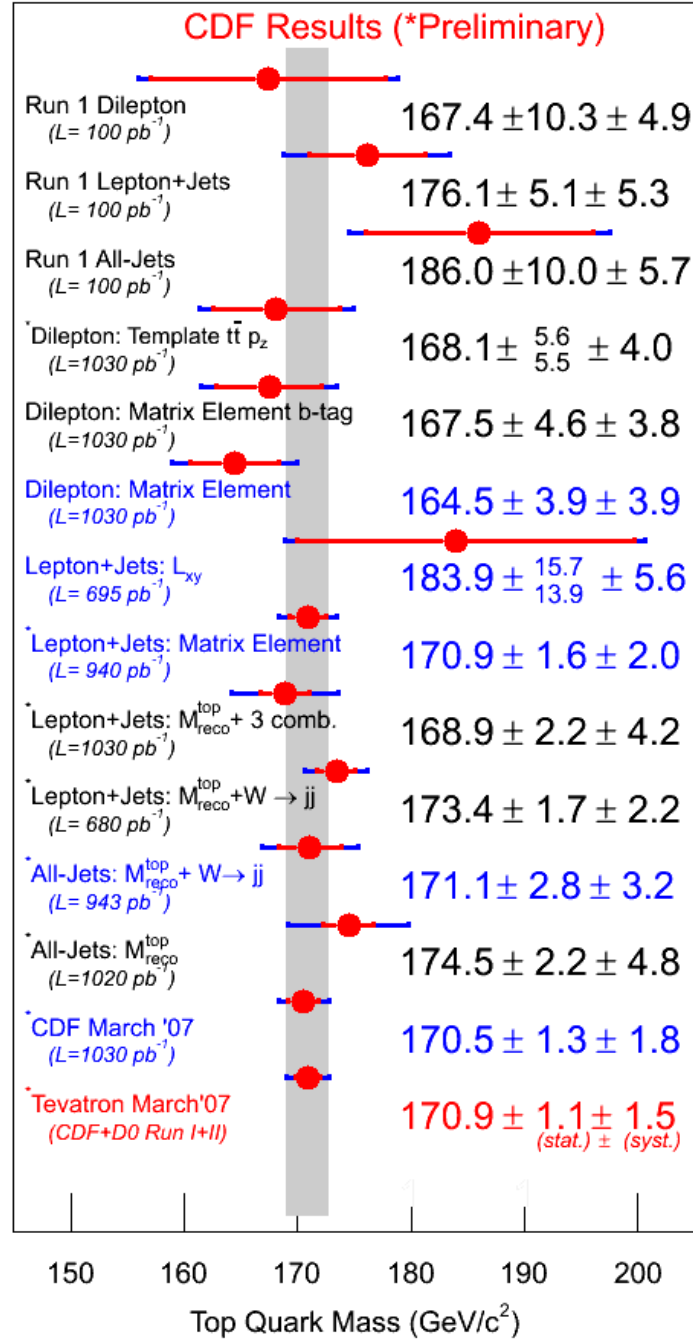


Figure 6.3: Results of top quark mass measurements using different analysis methods at CDF Run II. This figure was updated on March 2007, so this result is not listed in this figure.

Chapter 7

Conclusions

We have measured the top quark mass precisely. Collected data corresponds to an integrated luminosity of 1.7 fb^{-1} between March 2002 and March 2007 with CDF detector at Fermilab Tevatron. We selected $t\bar{t}$ candidates events which contain one high energy charged lepton, muon or electron, high missing E_T and four jets including at least one b-tagged jet, originating from top quark pair production process.

In order to measure the top quark mass precisely, we use the dynamical likelihood method which is based on a maximum likelihood method. The likelihood is defined by the differential cross section of top pair production process and the transfer function as a function of the pole mass of top quark and the jet energy scale. The transfer function is obtained as a weight of a jet energy originating from a certain parton energy using Monte Carlo samples. The transfer function reconstructs a parton energy from a jet energy statistically, and also the transfer function play an important role to calibrate the jet energy scale for the top quark pair production process specifically by creating it with a shifted jet energy scale on purpose. Thus we obtain the 2D likelihood as a function of the top quark mass and the jet energy scale so that the 2D likelihood is independent on the input jet energy scale and naturally leads to the proper jet energy scale. By calibrating the jet energy scale, the uncertainty on the jet energy scale can be much reduced as a statistical uncertainty, not a systematic uncertainty. So the total uncertainty on top quark mass is much improved.

We found 343 $t\bar{t}$ candidates events and applied the dynamical likelihood method with 2D fit to them. We measured the top quark mass to be $171.6 \pm 2.0 \text{ (stat.+JES)} \pm 1.3 \text{ (syst.)} = 171.6 \pm 2.4 \text{ GeV}/c^2$ with the dynamical likelihood method.

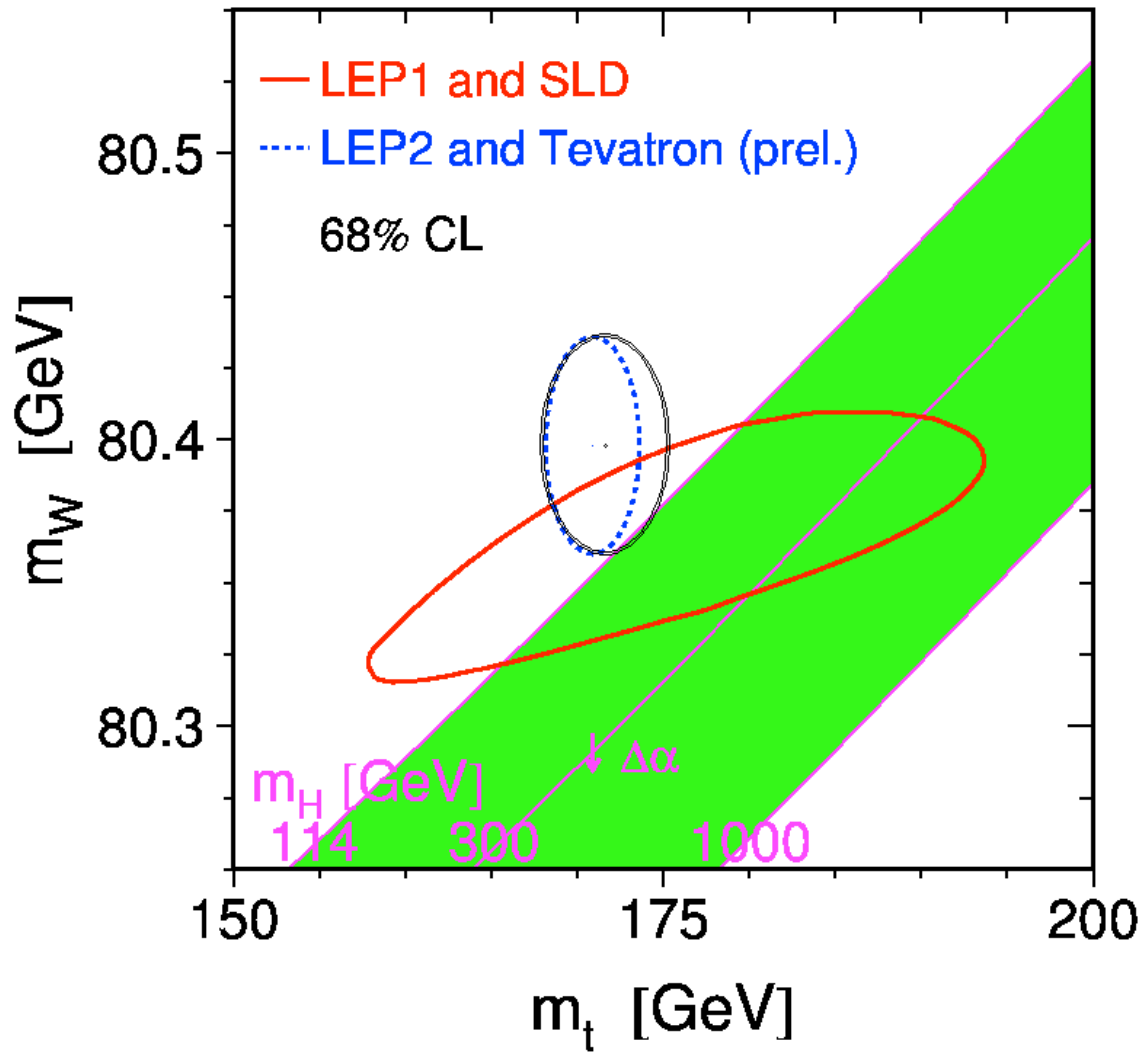


Figure 7.1: The prediction of mass area of Higgs boson with results of DLM using 1.73 fb^{-1} . The black curve represents the results in this analysis. Higgs boson mass is expected to approach to the SM region.

Bibliography

- [1] S. L. Glashow, Nucl. Phys., 22(579), 1961.
- [2] S. Weinberg, Phys. Rev. Lett., 19(1264), 1967.
- [3] A. Salam, Weak and Electromagnetic Interactions, Proceeding of the Nobel Symposium held at Lerum, Sweden, 1968.
- [4] F. Abe et al., Phys. Rev. Lett., 74(2626-2632), 1995.
- [5] S. Abachi et al., Phys. Rev. Lett., 74(2632-2637), 1995.
- [6] W.-M. Yao et al. <http://pdg.lbl.gov/>
- [7] P.W.Higgs. Phys. Lett., 12(132), 1964.
- [8] J.F.de Troconiz and F.J.Yndurain. Phys. Rev., D65(093002), 2002.
- [9] A.Aaltonen et al., CDF Collaboration. Phys. Rev. Lett.,93(142001), 2004.
- [10] D. Acosta et al., CDF Collaboration. Phys. Rev., D71(052003), 2005.
- [11] A.Abulencia et al., CDF Collaboration. Phys. Rev. Lett.,97(082004), 2006.
- [12] D. Acosta et al., CDF Collaboration. hep-ex/0607035, 2006
- [13] A.Abulencia et al., CDF Collaboration. Phys. Rev., D71(072005), 2005.
- [14] D.Acosta et al., CDF Collaboration. Phys. Rev., D72(052003), 2005.
- [15] D.Acosta et al., CDF Collaboration. Phys. Rev., D72(032002), 2005.
- [16] A.Abulencia et al., CDF Collaboration. Phys. Rev. Lett.,96(202002), 2006.
- [17] A.Abulencia et al., CDF Collaboration. hep-ex/0607095, 2006
- [18] A.Abulencia et al., CDF Collaboration. Phys. Rev. Lett., 96(152002), 2006.
- [19] A.Abulencia et al., CDF Collaboration. Phys., D73(112006), 2006.
- [20] A.Abulencia et al., CDF Collaboration. Phys. Rev., D74(032009), 2006.

- [21] A.Abulencia et al., CDF Collaboration. Phys. Rev. Lett., 96(022004), 2006.
- [22] A.Abulencia et al., CDF Collaboration. Phys. Rev., D73(032003), 2006.
- [23] A.Abulencia et al., CDF Collaboration. Phys. Rev., D73(092002), 2006.
- [24] A.Abulencia et al., CDF Collaboration. Phys. Rev. Lett., 96(152002), 2006.
- [25] A.Abulencia et al., CDF Collaboration. hep-ex/0510047, 2006.
- [26] D.Acosta et al., CDF Collaboration. Phys.Rev., D71(012005), 2005.
- [27] D.Acosta et al., CDF Collaboration. Phys.Rev. Lett., 95(022001), 2005.
- [28] D.Acosta et al., CDF Collaboration. Phys.Rev. Lett., 95(102003), 2005.
- [29] D.Acosta et al., CDF Collaboration. Phys.Lett., B639(172), 2005.
- [30] A.Abulencia et al., CDF Collaboration. Phys.Rev. Lett., 96(042003), 2006.
- [31] A.Abulencia et al., CDF Collaboration. Phys.Rev., D73(111103), 2006.
- [32] A.Abulencia et al., CDF Collaboration. hep-exp/0608062, 2006.
- [33] A.Abulencia et al., CDF Collaboration. Phys.Rev., D73(051101), 2006.
- [34] R. Bonciani et al. Nucl.Phys., B529(424), 1998.
- [35] J.Iliopoulos and L.Maiani S.L.Glashow. Phys.Rev., D2(1285), 1985.
- [36] S. Weinberg, Phys. Rev., D13(974), 1976.
- [37] S. Weinberg, Phys. Rev., D19(1277), 1979.
- [38] L. Susskind, Phys. Rev., D20(2619), 1979.
- [39] C. Hill, Phys. Lett., B266(419-424), 1991.
- [40] C. Hill, Phys. Lett., B345(483-489), 1995.
- [41] F.Abe et al.[CDF Collaboration]. Nucl. Instrum. Meth., A271(387), 1988.
- [42] A.Sill et al. Nucl. Instrum. Meth., A447(1), 2000.
- [43] T.Affolder et al. Nucl. Instrum. Meth., 526(249), 2004.
- [44] F.Bedeschi et al. Nucl. Instrum. Meth., A268(50), 1988.
- [45] L.Balka et al. Nucl. Instrum. Meth., A267(272), 1988.
- [46] S.Bertolucci et al. Nucl. Instrum. Meth., A267(301), 1998.

- [47] F.Abe et al. Phys. Rev. Lett., 73(2662), 1994.
- [48] K.Byrum et al. Nucl. Instrum. Meth., A268(46), 1988.
- [49] G.Ascoli et al. Nucl. Instrum. Meth., A268(33), 1988.
- [50] T.Dorigo et al. Nucl. Instrum. Meth., A461(560), 2001.
- [51] W.Wagner et al. Fermilab-conf-02-269-e, international europhysics conference on high energy physics (hep 2001), budapest, hungary. 12-18 Jul 2001.
- [52] B.Angelos et al. International conference on computing in high-energy physics and nuclear physics (chep 2000), padova, italy. 7-11 Feb 2000.
- [53] P.Canal et al. IEEE Trans. Nucl. Sci., 47(240), 2000.
- [54] PYTHIA, Torbjorn, Sjostrand, Stephen Mrenna and Peter Skands, <http://www.thep.lu.se/~torbjorn/Pythia.html>
- [55] HERWIG, Pino Marchesini et al, <http://hepwww.rl.ac.uk/theory/seymour/herwig/>
- [56] J.Pumplin et al., hep-ph/0201195, JHEP 0207 (2002) 012.
- [57] D. Stump et al., hep-ph/0303013, JHEP 0210 (2003) 046.
- [58] P.Avery, K.Read, and G.Trahern. CLEO Report CSN-212 (1985).
- [59] M. L. Mangano et al., High Energy Phys. JHEP 07 (2003) 001.
- [60] T.Affolder et al., Nucl. Instrum. and Methods 526 (2004) 249.
- [61] G. Grindhammer, M. Rudowicz, and S. Peters, Nucl. Instrum. and Methods, A290, 1990.
- [62] A. Bhatti et al., Nucl. instrum. Meth., A566(375-412), 2006.
- [63] K.Kondo: J.Phys. Soc. Jpn. 57 (1988) 4126.
- [64] K.Kondo: J.Phys. Soc. Jpn. 60 (1991) 836.
- [65] K.Kondo, T.Chikamatsu, S.H.Kim: J.Phys. Soc. Jpn. 62 (1993) 1177.
- [66] A.Abulencia et al., The CDF Collaborations, Phys. Rev. D73(092002), 2006.
- [67] A.Abulencia et al., The CDF Collaborations, CDF Note 9025, 2007.
- [68] A.Abulencia et al., The CDF Collaborations, CDF Note 8949, 2007.